UNIVERSITÀ DEGLI STUDI DI MILANO

Scuola di Dottorato in Fisica, Astrofisica e Fisica Applicata

Dipartimento di Fisica

Corso di Dottorato in Fisica, Astrofisica e Fisica Applicata

Ciclo XXVI

Search for direct top squark pair production in final states with two leptons with ATLAS in $\sqrt{s} = 7$ TeV and $\sqrt{s} = 8$ TeV pp collisions

Settore Scientifico Disciplinare FIS/04, FIS/01

Supervisore: Dottor Tommaso LARI

Coordinatore: Professor Marco BERSANELLI

Tesi di Dottorato di:

Federico MELONI

Anno Accademico 2012/13

Commission of the final examination:

External Referee:
Dr. Monica D'ONOFRIO (University of Liverpool)

External Members:
Prof. Peter LOCH (University of Arizona)
Dr. Marumi KADO (Université Paris-Sud et CNRS/IN2P3)

Internal Member:
Prof. Emanuela MERONI (Universitá degli Studi di Milano)

Final examination:

January 31, 2014

Universitá degli Studi di Milano, Dipartimento di Fisica, Milano, Italy

Cover illustration:

Event display of dileptonic event with one electron and one muon selected by the top squark analysis, recorded during the $\sqrt{s} = 7$ TeV run. The green and orange histograms show the energy deposit in the electromagnetic and hadronic calorimeters, respectively.

MIUR subjects:

FIS/01
FIS/04

PACS:

12.60.Jv

14.80.Ly

Contents

Introduction **ix**

1 The experimental setup **1**

1.1 The Large Hadron Collider (LHC) 1

1.1.1 The choice of a hadron collider 1

1.1.2 LHC experiments and accelerator chain 3

1.1.3 LHC parameters and operation 4

1.2 The ATLAS experiment 7

1.2.1 ATLAS coordinate system 8

1.3 The magnet system 10

1.4 Inner Detector 11

1.4.1 Pixel Detector 11

1.4.2 Semi-Conductor Tracker (SCT) 14

1.4.3 Transition Radiation Tracker (TRT) 15

1.5 Calorimeters 17

1.5.1 EM Calorimeter 18

1.5.2 Had Calorimeter 21

1.5.3 Forward Calorimeter 22

1.6 Muon Spectrometer 22

1.7 Forward detectors 25

1.8 ATLAS performance summary 26

1.9 Trigger, data acquisition and control systems 26

1.9.1 Trigger system 27
1.9.2 Readout architecture and data acquisition 28

2 A Natural extension of the Standard Model 31
2.1 The hierarchy problem and naturalness 32
2.2 Supersymmetry as solution to the hierarchy problem 33
2.3 The Minimal Supersymmetric Standard Model 34
2.3.1 R-parity 36
2.3.2 Supersymmetry breaking 36
2.3.3 The mass spectrum 38
2.3.4 A typical natural spectrum 40
2.4 A Dark Matter candidate 41
2.5 Unification of interactions 42
2.6 Third generation topologies 43
2.6.1 Top squark decay modes 44
2.7 Benchmark models 48
2.8 Top quark partners in other Beyond Standard Model theories 49

3 Data and Monte Carlo Simulation 51
3.1 Data samples 51
3.2 Monte Carlo simulation with $\sqrt{s} = 7$ TeV 52
3.2.1 Standard Model 52
3.2.2 Signal 53
3.3 Monte Carlo simulation with $\sqrt{s} = 8$ TeV 54
3.3.1 Standard Model 54
3.3.2 Signal 55

4 Event reconstruction 57
4.1 Tracks 57
4.2 Primary vertex 58
4.3 Jets 59
4.3.1 Jet energy calibration 62
4.3.2 b-tagging 63
4.4 Electrons 67
4.4.1 Electron performance 68
4.5 Muons 69
4.5.1 Muon performance 71

4.6 Missing Transverse Energy 72

5 Search for top squarks decaying to a neutralino and a top quark 75
5.1 Introduction 75
5.1.1 The stransverse mass 76
5.2 Trigger selection and object definition 78
5.3 Event selection 80
5.3.1 Event selection optimization 81
5.4 Kinematic distributions 90
5.5 Background estimate 100
5.5.1 $t\bar{t}$ background 100
5.5.2 Z+jets background 103
5.5.3 Minor backgrounds 107
5.5.4 Fake lepton background 107
5.6 Systematic uncertainties 112
5.6.1 Experimental systematics 112
5.6.2 Theoretical systematics 114
5.6.3 Other systematics 114
5.7 Results 116
5.8 Interpretation and limit setting 117

6 Search for top squarks decaying to a chargino and a bottom quark 121
6.1 Introduction 121
6.2 Trigger selection and object definition 124
6.3 Event selection 127
6.3.1 Event selection optimization 127
6.4 Kinematic distributions 134
6.5 Background estimate 148
6.5.1 Background Fit 149
6.5.2 Control Regions definition 149
6.5.3 Fake lepton background 163
6.5.4 Validation Regions definition 163
6.6 Systematic uncertainties 166
6.6.1 Experimental systematics 166
6.6.2 Theoretical systematics 167
6.6.3 Other systematics 168

6.6.4 Background fit results and nuisance parameters 170
6.7 Results 172
6.8 Interpretation and limit setting 172

Conclusions **183**

A Hypothesis testing **185**
A.1 Profile likelihood-ratio 186
A.2 Limit setting 186

Bibliography **189**

Introduction

The Large Hadron Collider is a particle physics accelerator built at CERN. It collides head-on bunches of protons or heavy ions. The analysis of these collisions resulted in the discovery of a particle compatible with a Standard Model (SM) Higgs boson and allows to explore new physics phenomena beyond the SM.

This thesis follows the evolution of my involvement in the analysis of 2011-2013 ATLAS data, focusing on the search for new physics beyond the SM. ATLAS is one of the four main experiments at the LHC. The analyses I have contributed to were driven by the amount of collected luminosity, starting from a search for strong production of supersymmetric particles in events with two final state leptons [1]. The lack of early discoveries pushed the scientific community to consider models where the production of third generation squarks are suggested as one of the most favored scenarios to be observed at the LHC.

This thesis presents two searches for direct top squark pair production in events with two leptons, in which I was heavily involved. The first search (chapter 5) targets the $\tilde{t}_1 \to t + \tilde{\chi}_1^0$ decay, using a cut and count method in 4.7 fb^{-1}of pp collision data collected during the 2011 run. The results have been published in a paper [2]. My personal contribution consisted in the background estimation (particularly focusing on the $t\bar{t}$ production, the dominant background for this analysis), the systematic uncertainties evaluation and the results interpretation.

The second search (chapter 6) targets the $\tilde{t}_1 \to b + \tilde{\chi}_1^{\pm}$ decay, or the three body decay $\tilde{t}_1 \to b + W + \tilde{\chi}_1^0$ via an off-shell top quark. This analysis uses the full 20.3 fb^{-1}of pp collision data collected during the 2012 run, and has been published showing preliminary results [3]. My contribution to this analysis has been even more substantial: I helped on the selection cuts optimization, I took care of the background estimation (but for the fake lepton background), the systematic uncertainties evaluation and the results interpretation. Because of my contributions,

I have been chosen as an editor of the paper (in preparation) that summarizes all the ATLAS searches for top squarks in the two leptons channel.

In parallel with my physics studies, I have contributed to the ATLAS vertex reconstruction performance group, focusing on the study of the number of reconstructed vertices as a function of the number of interactions. I have built an online database to monitor this quantity during the data-taking and studied the systematic effects involved in the vertex reconstruction. In particular, I contributed to the development of an analytical parameterization on the relationship between the number of reconstructed vertices and the number of interactions taking into account the main reconstruction effects: reconstruction efficiency and inability of resolving nearby interactions in distinct vertices (vertex masking). I used this parameterization to study both the current performances and the possible improvements in upgrade scenarios. I chose not to put these results in my thesis because of their weaker connection with the other topics which are dealt with in this document.

The thesis is organized as follows: chapter 1 introduces the LHC accelerator and the ATLAS experiment; chapter 2 briefly describes the theory and motivations behind the searches presented in this work. Chapter 3 describes the data samples used in this thesis, while chapter 4 describes the event reconstruction in the ATLAS experiment, focusing on the objects used the analyses which follow. Chapter 5 and 6 present the two analyses mentioned above.

CHAPTER 1

The experimental setup

The analyses presented in this thesis use data of proton-proton collisions collected by the ATLAS experiment at the Large Hadron Collider at CERN during 2011 and 2012. This chapter describes the experimental setup of the LHC to collide protons at a center-of-mass energy up to $\sqrt{s} = 8$ TeV in section 1.1 and the ATLAS detector in section 1.2.

1.1 The Large Hadron Collider (LHC)

In the early '90, the scientific community started to design a high energy physics collider able to deliver a center of mass energy one order of magnitude greater than the other already existing hadronic colliders (Tevatron) and two orders of magnitude greater than the existing leptonic colliders (LEP). The main objective of this new machine would have been the investigation of the nature of electroweak symmetry breaking and the search for physics beyond Standard Model at the TeV scale: this includes the search for the Higgs boson and for particles predicted by Supersymmetric models (SUSY).

The result of this design challenge is the Large Hadron Collider [4]: a hadronic (proton-proton and lead ions) collider built inside the tunnel that housed LEP (Large Electron-Positron collider) near the city of Genève in Switzerland.

1.1.1 The choice of a hadron collider

The main motivation to use a hadron collider instead of electron-positron one is much higher achievable center of mass energy, a fundamental feature for a discovery machine. Synchrotron radiation, leading to a large energy loss in e^+e^-

colliders, is the crucial limiting factor. Charged particles moving along a curved trajectory loose energy following the relation:

$$\frac{dE}{dt} \propto \frac{E^4}{m^4 R} \tag{1.1}$$

where E and m are particle's energy and mass, while R is the trajectory's radius of curvature. This implies that at fixed energy and collider dimensions (radius), electrons loose $(m_p/m_e)^4 \sim 10^{12}$ times more energy than a proton beam with the same characteristics. The use of electrons would have been possible only in a synchrotron with a much larger radius or in a linear accelerator implying a much greater cost than the solution adopted.

An hadron collider brings some problems that are absent in leptonic colliders due to the proton's composite structure. Proton-proton collisions can be of two different types: *soft collisions* or *hard collisions*.

Soft collisions are distant collisions, with protons interacting as a whole object. These interactions have a small transferred momentum and the interaction products have a small transverse momentum, e.g. $\langle p_{\mathrm{T}} \rangle \simeq 500$ MeV (a natural system of units is used henceforth, assuming c=1).

In *hard collisions* protons interact revealing their inner structure: the collision is studied in terms of QCD processes between different partons. In this type of interaction, the transferred momentum is large and there is a chance to generate new particles. A generic mixture of soft and hard collisions is called *minimum-bias* event.

In hadron colliders the partonic center of mass energy is unknown, making kinematic calculation more difficult. Another problem comes from the fact that the cross section for *hard collisions*, which are important for the discovery of new physics, is much smaller than the one for *soft collisions*. This creates the need for a high luminosity operating collider: the rate of the proton-proton interactions inside the LHC machine is given by the product of the proton-proton cross section σ and the luminosity $\mathcal{L}$.

The instantaneous luminosity $\mathcal{L}$, defined in equation 1.2, is the product of the numbers of particles n_1, n_2 in both crossing bunches and the frequency f of bunch crossings, divided by the cross sectional area $A = 4\pi\sigma_x\sigma_y$ of a bunch:

$$\mathcal{L} = f\frac{n_1 n_2}{4\pi\sigma_x\sigma_y} \tag{1.2}$$

The instantaneous luminosity has been progressively increased during operation, as shown in figure 1.1. In 2012, for each bunch crossing there were up to about

30 collisions that summed themselves to each interaction with large transverse momentum. This soft-collision background is usually called *pile-up*.

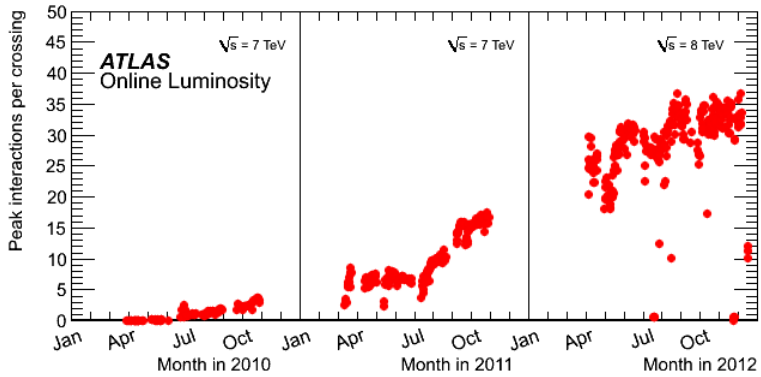

Figure 1.1: The maximum mean number of events per beam crossing versus day during the p-p runs of 2010, 2011 and 2012. The mean value of the number of events in each bunch crossing has been computed within periods of about two minutes of data-taking (*luminosity block*) [5]. Only data taken during stable beams has been considered.

1.1.2 LHC experiments and accelerator chain

The LHC is located in a 27 km long underground tunnel. The tunnel lies at a depth of about 100-120 m and crosses the border of France and Switzerland.

The LHC is designed to serve proton and ion beam collisions to four main experiments: the two multipurpose detectors ATLAS (A Toroidal Lhc ApparatuS) [6] and CMS (Compact Muon Solenoid) [7], LHCb (LHC beauty experiment) [8], focusing on b-physics and ALICE (A Lhc Ion Collider Experiment) [9] focusing on heavy-ion physics.

Before being injected into the LHC, the particles are accelerated step by step up to the injection energy of 450 GeV, by a series of accelerators shown in figure 1.2. For protons, the first system is a linear accelerator (LINAC2), which accelerates the beam at an energy of 50 MeV. The protons then go through the Proton Synchrotron Booster (PSB) and are brought to 1.4 GeV. After that they are injected into the Proton Synchrotron (PS), where they are accelerated to 26 GeV. Finally, the Super Proton Synchrotron (SPS) is used to further increase their energy to 450 GeV. From the SPS, two transfer lines inject the proton beams into the LHC.

For lead ions the beam production is different. They are first accelerated by a different linear accelerator (LINAC3). The ions are then further accelerated by the PS and SPS before being injected into the LHC ring.

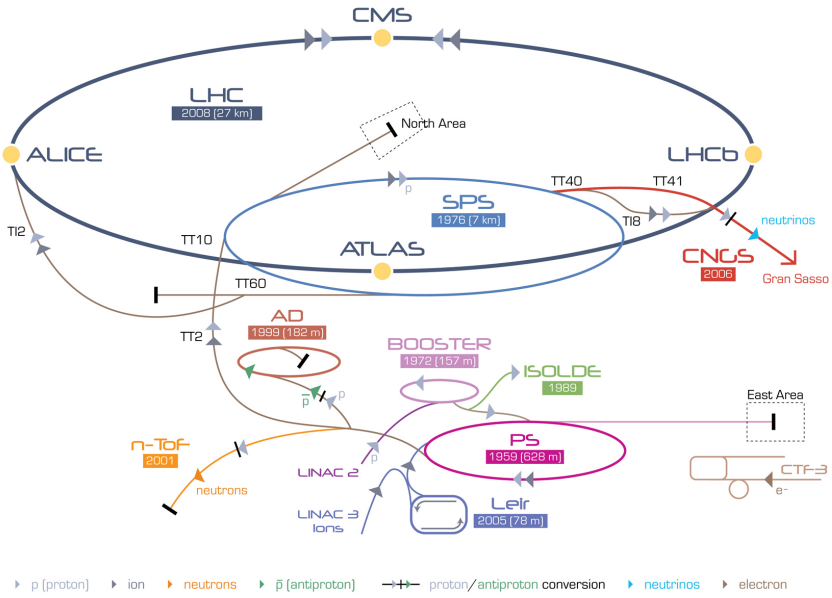

Figure 1.2: Scheme of the accelerator chain up to LHC. The LHC experiments are shown as yellow circles.

1.1.3 LHC parameters and operation

The LHC design value for instantaneous luminosity in proton-proton collisions at center of mass energy $\sqrt{s} = 14$ TeV is $\mathcal{L} = 10^{34}$ cm^{-2}s^{-1}. With this configuration there are an average of about 23 inelastic scatterings per bunch crossing, in which nearly 1000 new particles are produced. The 2808 LHC nominal contain $\sim 10^{11}$ protons each, and the nominal bunch separation is 25 ns.

The LHC started its operations on 10th September 2008, with the first beams circulating into the rings, in both directions, without collisions. Nine days later an accident was caused by a faulty electrical connection between two magnets during tests of the dipole circuit. In the accident 53 magnets were damaged. This caused a delay of about one year to repair the damaged magnets, check the electrical connections and improve the safety systems. During Fall 2009, the operations started again, with the first proton-proton collisions at a centre of mass energy

of 900 GeV recorded by the four experiments on 23rd November 2009. After a 900 GeV collisions data taking, the centre of mass energy was further increased to 2.36 TeV, producing collisions at the highest energy ever reached before. The first proton-proton collisions at $\sqrt{s} = 7$ TeV were registered on 30th March 2010, starting a new running period that went on until the beginning of November, when the LHC provided the first heavy ion collisions. Proton-proton collisions have started again on 13th March 2011, after the winter technical stop. During the commissioning phase, the number of colliding bunches has been progressively increased towards the design value, even if this has never been reached for physics. At the end of 2010 the maximum number of colliding bunches has been 348, a maximum number of 1092 has been then reached in June 2011. At the end of 2011 proton-proton run the number of colliding bunches is about 1400, as shown in figure 1.3: the bunch separation of 50 ns has been reached. Only in 2015 the nominal value of 25 ns will be reached.

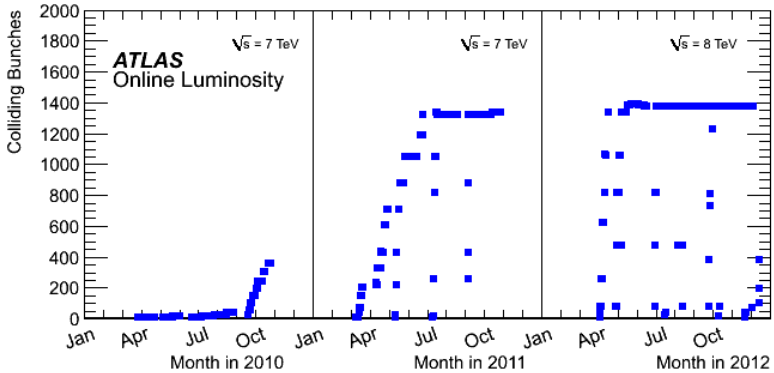

Figure 1.3: The number of colliding bunches in ATLAS versus time during the proton-proton runs of 2010, 2011 and 2012 [5]

The maximum instantaneous luminosity that has been reached in 2010 is slightly higher than 2×10^{32} cm^{-2}s^{-1}, while during 2011 run a peak of 3.65×10^{33} cm^{-2}s^{-1} has been achieved. In 2010 and 2011 HI running collisions at 2.76 TeV per nucleon took place, reaching a peak instantaneous luminosity of 30×10^{24} cm^{-2}s^{-1}.

Data-taking restarted from March 2011 to the end of the 2011. During 2012, the LHC provided proton-proton collisions at a center of mass energy of 8 TeV, with a bunch spacing of 50 ns. A peak instantaneous luminosity of 8×10^{33} cm^{-2}s^{-1} has been reached.

The nominal pp run configuration is compared with the setup used at the end of 2012 in table 1.1.

Table 1.1: Important parameters for the LHC. The design configuration is compared with the setup used in the 2012 pp run.

Parameter	**Design value**	**End of 2012**
$\sqrt{s}$	14 TeV	8 TeV
Bunch spacing	25 ns	50 ns
Peak luminosity	10^{34} cm^{-2}s^{-1}	8×10^{33} cm^{-2}s^{-1}
Number of bunches per beam	2808	1380

1.2 The ATLAS experiment

The ATLAS detector, A Toroidal LHC ApparatuS, is located at Point 1, one of the four interaction points of the LHC, in a large underground cavern. Figure 1.4 shows a sketch of the 44 m $\times$ 25 m detector, weighting about 7000 tons. It has a cylindrical layout and a forward-backward symmetry with respect to the interaction point.
The detector is designed for the study of high energy proton-proton and ion-ion collisions. Of particular interest for the physics at LHC are the collisions that produce energetic particles perpendicularly to the axis of colliding beams, the so called high transverse momentum phenomena.

The detector assembly lasted more than four years, from 2003 to July 2007, when the innermost detector was inserted and the last end-cap toroidal magnet was lowered in the pit. Since 2008 it has been recording cosmic-ray events and, starting from November 2009, proton-proton collision events at rates of up to 400 Hz.

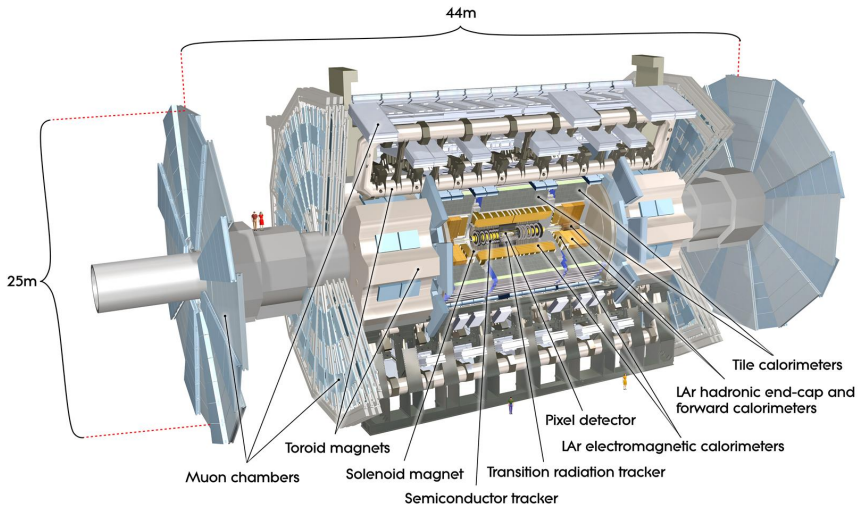

Figure 1.4: Detailed view of the ATLAS detector and its sub-detectors [6].

The very high luminosity operating conditions of the LHC, together with the need to be able to detect and record very rare processes, imposes stringent demands on the capabilities of the experiment. To provide sensitivity to any possi-

ble evidence of new physics beyond the Standard Model, ATLAS had to meet the following requirements:

- Full azimuthal coverage and large geometrical acceptance.
- Excellent tracking capability: precise momentum determination over a wide range of energies, from hundreds of MeV to a few TeV.
- Vertex detectors close to the beam line, to identify taus and jets originating from b-quarks.
- Hermetical calorimetry for missing transverse energy measurements
- Fine granularity to separate signal contributions from different particles.
- Good muon identification and momentum measurement up to a few TeV.
- Fast triggering systems, to spot interesting events and reduce background levels for efficient storage.
- Radiation hardness to tolerate the large particle fluxes provided by the LHC without loss of performance or important aging effects.

ATLAS is composed by a set of sub-detectors, each designed and optimized for a specific task. It can be divided into three major parts: the Inner Detector (Section 1.4) that surrounds the interaction region and operates in a solenoidal magnetic field, the Calorimeter system (Section 1.5) surrounding the ID and the Muon Spectrometer (Section 1.6) with a dedicated toroidal magnetic field. The choice of two separate magnetic systems (Section 1.3), one for the internal tracking, and one for the outer muon tracker, has driven the design of the rest of the detector. The spatial arrangement of these sub-detectors and an event cross section is shown in figure 1.5.

1.2.1 ATLAS coordinate system

ATLAS uses a right-handed coordinate system (ϕ, η, z) instead of the cartesian coordinate system (x, y, z). ϕ and η are expressed with respect to x, y and z. To define these, the origin of the (x, y, z) coordinate system is located in the center of the detector and the z-axis is defined counter-clockwise, while the positive y-axis goes upwards with the increasing height of the detector. The x-axis is pointing

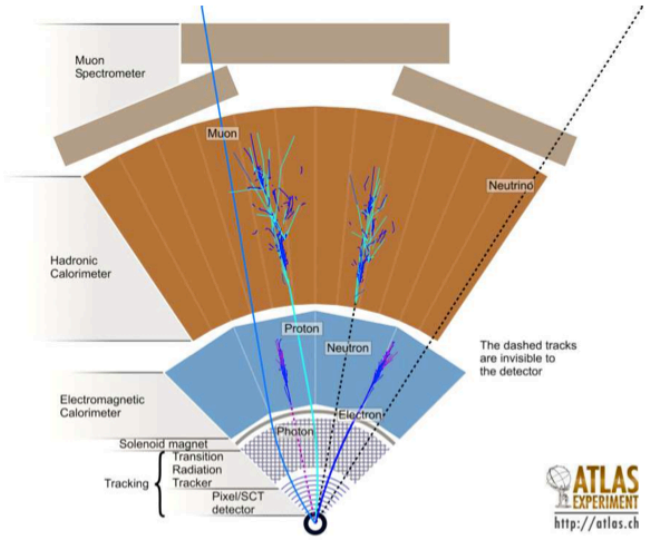

Figure 1.5: Schematical view of the specialized particle detectors of ATLAS. The toroidal magnets between the hadronic calorimeter and the muon spectrometer are not shown in this figure [6].

towards the center of the LHC. The azimuthal angle ϕ is measured around the beam axis. The pseudorapidity η can be introduced as

$$\eta = -\ln \tan \frac{\theta}{2} \tag{1.3}$$

with θ being the polar angle with respect to the positive y-axis. For massive objects such as jets, the rapidity is used, given by

$$y = \frac{1}{2} \ln \left(\frac{E + p_z}{E - p_z} \right) \tag{1.4}$$

Rapidity, or pseudorapidity, are preferred with respect to the polar angle θ because the collisions are boosted relative to each other along the z-axis. This quantity is additive. A Lorentz boost β' along the z-axis is equivalent to a boost with rapidity $y' = \text{arctanh}(\beta')$, and results in $y \rightarrow y + y'$. This implies that rapidity differences are invariant, and hence the shape of the high energy particle multiplicity spectrum dN/dy is also invariant under a boost along the z-axis.

The transverse momentum p_T of a particle in the detector is defined as the momentum perpendicular to the z-axis:

$$p_{\mathrm{T}} = \sqrt{p_x^2 + p_y^2} \tag{1.5}$$

1.3 The magnet system

The magnet configuration comprises a thin superconducting solenoid surrounding the Inner Detector cavity, and three large superconducting toroids (one barrel and two end-caps), arranged with an eight-fold azimuthal symmetry around the calorimeters, which provide bending power for the Muon Spectrometer. The magnet system is shown in figure 1.6

- *Solenoid*: the solenoid has its field axis matching the beam direction (z). It is made of a single-layer aluminum coil wound by a NbTi conductor, optimizing thus its thickness in order to have a small impact on the energy measurement in the calorimeters. The solenoid has an inner radius of 1.23 m and a total length of 5.8 m. A magnetic field of 2 T is produced in the central region of the the Inner Detector.

- *External Toroids*: the external toroidal magnets use coils consisting of a conductor made of a mixture of aluminum, niobium, titanium and copper, and they extend the magnet system to a total of 26 m length and 20 m diameter. This configuration provides a magnetic field for the Muon Spectrometer of 0.5 T and 1 T in the barrel and end-caps, respectively. The magnet system operates with nominal currents of 8 kA for the solenoid, and of 25 kA for the toroids, respectively. Every toroid has a separate cryogenic system, while in the end-caps the coils have common cryostat.

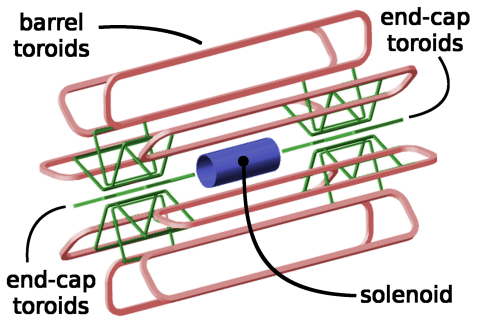

Figure 1.6: Schematical view of the ATLAS magnet system.

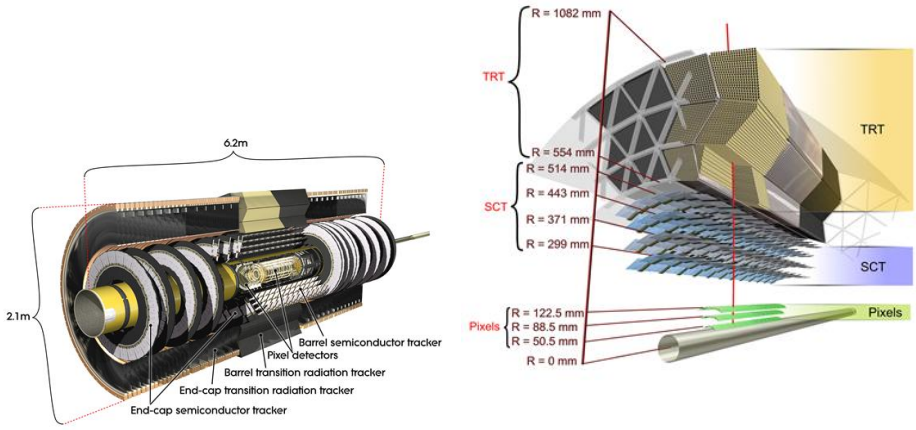

(a) (b)

Figure 1.7: Schematic views of the ATLAS Inner Detector [6]

1.4 Inner Detector

The Inner Detector is the innermost system of the ATLAS detector. The high position and momentum resolution required by the ATLAS physics program are achieved by the combination of high bending power and fine granularity position measurements for charged particles. The Inner Detector offers pattern recognition, momentum and vertex measurements, and electron identification capabilities. Its schematic view is shown in Figure 1.7. It is composed by three independent but complementary sub-detectors: two silicon detectors, the *Pixel Detector* and the *Semi-Conductor Tracker* (SCT), and the *Transition Radiation Tracker* (TRT) composed of straw-tubes. The Inner Detector is immersed in an axial magnetic field of 2 T and its overall dimensions are 2.1 m in diameter and 6.2 m in length and covers a pseudorapidity region of $|\eta| < 2.5$.

A summary of their main characteristics is also reported in table 1.2.

1.4.1 Pixel Detector

The ATLAS Pixel Detector (figure 1.8) is the nearest system to the collision point and it is built directly onto the beryllium beam pipe in order to provide the best possible primary and secondary vertex resolution. It was designed to operate in the high particle multiplicity of LHC, maintaining high efficiency and an excellent

Table 1.2: Summary of the main characteristics of the three ATLAS Inner Detector sub-detectors [6]

		Radial extension (mm)	Length (mm)
Overall ID envelope		$0 < R < 1150$	$0 < \|z\| < 3512$
Beam pipe		$29 < R < 36$	
Pixel	Overall envelope	$45.5 < R < 242$	$0 < \|z\| < 3092$
3 cylindrical layers	Sensitive barrel	$50.5 < R < 122.5$	$0 < \|z\| < 400.5$
2×3 disks	Sensitive end-cap	$88.8 < R < 149.6$	$495 < \|z\| < 650$
SCT	Barrel envelope	$255 < R < 549$	$0 < \|z\| < 805$
	End-cap envelope	$251 < R < 610$	$810 < \|z\| < 2797$
4 cylindrical layers	Sensitive barrel	$299 < R < 514$	$0 < \|z\| < 749$
2×9 disks	Sensitive end-cap	$275 < R < 560$	$839 < \|z\| < 2735$
TRT	Barrel envelope	$554 < R < 1082$	$0 < \|z\| < 780$
	End-cap envelope	$617 < R < 1106$	$827 < \|z\| < 2744$
73 straw planes	Sensitive barrel	$563 < R < 1066$	$0 < \|z\| < 712$
160 straw planes	Sensitive end-cap	$644 < R < 1004$	$848 < \|z\| < 2710$

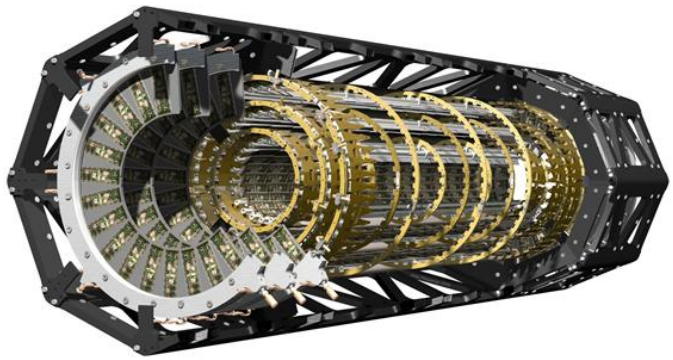

Figure 1.8: The ATLAS Pixel Detector [6]

position resolution in the $r - \phi$ plane of < 15 μm, as well as a time resolution of less than the 25 ns nominal proton bunch spacing of the LHC. At the time of writing, after 3 years of operation, the detector performance is excellent with a hit detection efficiency of $\sim 96\%$.

The Pixel detector consists of three cylindrical barrel layers[1] with 1456 mod-

[1]The layer closest to the beam pipe is referred to as L0 or b-layer. The outer layers are called L1 and

ules and two end-caps with three disks each having a total of 288 modules, covering the pseudorapidity range of $|\eta| < 2.5$. The total number of readout channels is approximately 80×10^6. The barrel layers have radii of 50.5 mm (b-layer), 88.5 mm (L1) and 122.5 mm (L2) and are 800 mm long.

The LHC environment imposes a high radiation tolerance (up to 500 kGy for a fluence of 10^{15} 1 MeV n_{eq}/cm^2) and the adoption of an evaporative C_3F_8-based cooling integrated in the module supports to keep a low leakage current and remove the heat generated by the electronics.

The detector is operated at -13°C since Summer 2009, with the cooling system able to operate down to slightly lower temperatures which will be exploited only later in the detector life when the radiation damage effects will be more important.

A pixel module consists of a 250 μm thick sensor with n^+ pixels implanted on the n-doped bulk with a p^+ backplane on the opposite side, 16 Front-End chips bump-bonded to this sensor and a module controller chip (MCC). Each module has an active area of 16.4×60.8 mm^2 consisting of 47232 (328×144) pixels. The typical pixel size is 50×400 μm^2. To enable full coverage in the regions between front-end chips, approximately 10% of the sensor pixels have a size of 600×50 μm^2 (long pixels). The 16 chips read out in total 46080 channels, but all 47232 pixels are readout, as pixels in the inter-chip regions are ganged to be read out. In order to fully deplete the semi-conductor a bias voltage 150 to 600 V can be applied to separate electron-hole pairs created by a traversing charged particle. The current is amplified and measured, counting a hit in a certain pixel sensor if it exceeds a threshold, which is constantly calibrated to provide the best signal-to-noise separation for each pixel sensor. At present time the threshold is set to the value of 3500 e^- with a dispersion of ~ 40 e^- and a fraction of masked pixels around 0.1%. There are nearly 500 reconstructed hits/event in the b-layer and despite the very high pile-up level, the Pixel Detector occupancy[2] is still small.

When a charge deposited in the sensor is above the discriminator threshold, the front-end electronics stores the Time-over-Threshold (ToT) quantity, i.e. the time during which the pre-amplifier output is above threshold. By design the ToT has a nearly linear dependence on the amplitude of the pre-amplifier output and therefore on the charge released in the sensor. The measurement of the deposited charge, obtained with the calibration of the ToT, allows several improvements for

L2.

[2]The Pixel Detector occupancy is defined as the fraction of detector channels with a hit in a local area

the detector performance, like the position resolution where the improvement is obtained by weighting properly the pixel hit in cluster position reconstruction with a charge sharing algorithm. Another important application of the ToT information is the determination of the specific energy loss dE/dx with a resolution of 12%.

The Pixel Detector operates in a solenoidal field of 2 T, therefore the Lorentz angle needs to be determined with good accuracy, by measuring the mean cluster size as a function of the track incident angle. The measured value of $\theta_L = (211.3 \pm 1.6)$ mrad is close to the expected value of 225 mrad.

1.4.2 Semi-Conductor Tracker (SCT)

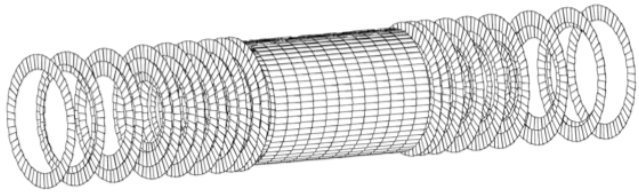

Figure 1.9: Geometrical layout of the SCT [6]

Going outwards from the beam pipe, the SCT is the second system (shown in figure 1.9) of the Inner Detector. It is composed by four cylinders in the barrel region, covering the pseudorapidity range $|\eta| < 1.1 - 1.4$, with radii between 299 mm and 514 mm and a full length of 1492 mm. Each of the two end-caps consists of 9 disks covering pseudorapidity range $1.1 - 1.4 < |\eta| < 2.5$ and radii extending to 56 cm. It provides typically eight measurements (four space-points) for particles originating in the beam-interaction region.

The SCT detector uses the same detection principle and material, semiconducting silicon, as the pixel detector, but instead of small rectangular pixels larger strip sensors are used. The SCT comprises 61 m^2 of silicon sensors with 6.3 million readout channels. It operates in a near zero humidity nitrogen environment and is cooled nominally to -7°C by a C_3F_8 evaporative cooling system, to suppress reverse annealing arising from radiation damage. The silicon sensors are all 285 μm thick single-sided p-on-n devices, with 768 AC-coupled micro-strips. There are 8448 identical rectangular shaped barrel sensors with size 64.0 $\times$ 63.6 mm and 80 μm strip pitch. The end cap disks use wedge shaped sensors of five slightly different sizes to accommodate the more complex geometry. There are 6944 wedge

sensors in total, with strip pitch ranging from 56.9 to 90.4 μm.

There are a total of 4088 modules, determining the basic granularity of the SCT detector: 2112 rectangular shaped modules used to construct the barrel cylinders and 1976 wedge shaped modules of three different sizes used to construct the end-cap disks. Modules consist of two pairs of back-to-back sensors, glued to a thermally conductive substrate for mechanical and thermal stability. Pairs on opposite sides are rotated by 40 mrad to form a stereo angle in order to enable a resolution measurement in the direction parallel to the strips.

More than 99% of the SCT strips have remained fully functional and available for tracking throughout all data taking periods. The number of disabled strips (typically due to high noise or un-bonded channels) and non-functioning chips is negligible and the largest contribution is due to disabled modules (total fraction: 0.73%).

The intrinsic accuracies of the SCT are 17 μm in the azimuthal direction and 580 μm along the beam direction, while the intrinsic hit efficiency is determined by counting the number of recorded hits on high p_T tracks (> 1 GeV/c) through the SCT by the number of possible hits, after ignoring known disabled strips. The nominal design requirement was for hit efficiency to be $> 99\%$. The barrels have a mean hit efficiency of 99.9% over all layers. Similarly, the hit efficiencies for the SCT end-caps are measured to be 99.8%.

1.4.3 Transition Radiation Tracker (TRT)

The TRT is the outermost system of the Inner Detector. Its sensitive volume covers radial distances from 563 mm to 1066 mm. It consists of drift tubes with a 4 mm diameter that are made from Wound Kapton (straw tubes) and reinforced with thin carbon fibers. In the centre of each tube there is a gold-plated tungsten wire of 31 μm diameter. With the wall kept at a voltage of -1.5 kV and the wire at ground potential, each tube acts as a small proportional counter. The tubes are filled with a gas mixture of 70% Xe, 27% CO_2, and 3% O_2.

The TRT barrel region contains 52544 straw tubes of 1.5 m length, parallel to the beam axis, arranged in three cylindrical layers and 32 ϕ sectors. They cover a radius from 0.5 m to 1.1 m and a pseudorapidity range of $|\eta| < 1$. The central wires are electrically split and read out at both ends of the straw. The end-caps contain radial 0.4 m long straws that are arranged perpendicular to the beam axis. Each side consists of 122880 straws, covering the geometrical range 0.8 m$< |z| <$

2.7 m and $1 < |\eta| < 2$. The end-cap straws are read out at their outer end.

When a charged particle traverses the TRT, it ionizes the gas inside the straws. The resulting free electrons drift towards the wire where they are amplified and read out. The spaces between the straws are filled with polymer fibers (barrel) and foils (end-caps) to create transition radiation, which may be emitted by highly relativistic charged particles as they traverse a material boundary. This effect depends on the relativistic factor $\gamma = E/m$ and is strongest for electrons. Typical photon energies are 5-30 keV. These soft X-rays can be absorbed by Xe atoms, depositing additional energy in the gas and leading to significantly higher readout signals. Such signals are detected by comparing them against an additional high threshold of 6 keV. The fact that the emission of transition radiation is much more likely for an electron than for a pion of the same momentum can be used to discriminate these particle types.

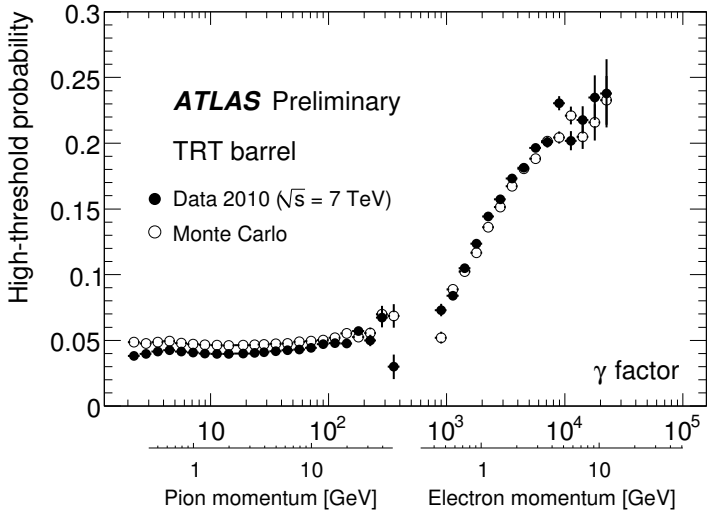

Figure 1.10: Probability of a transition radiation high-threshold hit in the TRT barrel as a function of the Lorentz Factor. Measurements from 2010 LHC collision events are compared to predictions from Monte Carlo simulations.

This design makes the TRT complementary to the silicon-based tracking devices: the single-point resolution of 120 μm is larger than that of the silicon trackers, but this is compensated by the large number of hits per track (typically more than 30) and the long lever arm.

The TRT readout data merely contains time information, which needs to be

calibrated to be useful for tracking. The $R(t)$ calibration relates the measured drift time with a particle's distance of closest approach to the readout wire. It depends on the properties of the active gas (mixture, pressure, temperature), the voltage that is applied to the tube, and the magnetic field.

Another source of information for the particle identification is the time over threshold (ToT), i. e. the number of time bins for which a readout signal exceeds the (low) threshold. This quantity depends on the particle's specific energy loss dE/dx, which in turn depends on the relativistic velocity β according to the Bethe-Bloch law.

1.5 Calorimeters

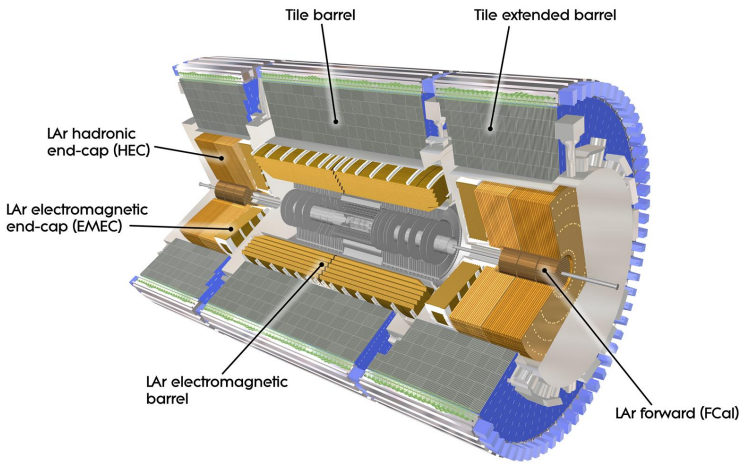

Figure 1.11: Schematic view of the ATLAS Calorimetric system [6]

The calorimeters are prime devices to measure the energy of particles through total absorption. In order to do this the entering point of a particle and the following shower of lower energy particles are measured. The high luminosity conditions and interesting physics events signatures require calorimeters with extremely good performances in terms of granularity, response time and energy resolution.

The ATLAS experiment has chosen a non-compensating[3] sampling calorime-

[3]The calorimeter signals for hadrons are in general smaller than for electrons or photons of the same

ter system that consists of two sections covering the range $|\eta| < 4.9$: an electromagnetic calorimeter (EM) and a hadronic calorimeter (Had). The electromagnetic calorimeter uses liquid argon (LAr) as sensitive material [10]: it is divided into two sections, barrel+end-cap calorimeter for region of $|\eta| < 3.2$ and a forward calorimeter covering $3.2 < |\eta| < 4.9$. The hadronic calorimeter is a Iron-Scintillator sampling calorimeter composed by a central cylinder and two side extensions: the hadronic calorimeter's end-caps use the same LAr technology on which is based the electromagnetic calorimeter [11]. Details about the coverage and segmentation of the calorimeter systems are shown in table 1.3. A schematic view of the calorimeter system is shown in figure 1.11.

One of the most important requirements for calorimeters is to provide good containment for electromagnetic and hadronic showers: the number of jets reaching the muon system (punch-through) has to be limited in order to have a good muon identification. This can be done exploiting the density of the material used in the calorimeter and in the supporting structure. For this reason, the total thickness of the EM calorimeter is more than 22 radiation lengths (X_0) in the barrel and more than 24 X_0 in the end-caps. It contains electrons and photons showers up to $\sim$ 1 TeV and it also absorbs almost 2/3 of a typical hadronic shower. The average 11 interaction lengths λ (including 1.3 λ from the support material) are adequate to provide good resolution for high-energy jets and sufficient to reduce punch-through well below the irreducible level of prompt or decay muons.

Some details on the different calorimeter regions are given below, and its nominal performance goals are summarized in table 1.4

1.5.1 EM Calorimeter

The EM calorimeter uses lead plates as passive and liquid argon (LAr) as active detector material. To ensure the maximum azimuthal coverage the EM Calorimeter was designed with an accordion geometry, as shown in figure 1.12: the readout electrodes and the lead absorbers are laid out radially and folded so that particles can not cross the calorimeter without being detected. It is divided into one barrel part ($|\eta| < 1.475$) and two end-caps ($1.375 < |\eta| < 3.2$), each one with its own cryostat. In order to reduce material in front of the EM calorimeter, the central solenoid and the LAr calorimeter itself share a common vacuum vessel. The bar-

energy ($e/h > 1$). The difference must be taken into account by an additional correction applied to hadronic objects.

Table 1.3: Pseudo-rapidity coverage, longitudinal segmentation and granularity of the ATLAS calorimeters.

	η **coverage**		**Granularity** $(\Delta\eta \times \Delta\phi)$
EM calorimeter	barrel	end-cap	
Presampler	$\lvert\eta\rvert < 1.54$	$1.5 < \lvert\eta\rvert < 1.8$	0.025×0.1
Sampling 1	$\lvert\eta\rvert < 1.475$	$1.375 < \lvert\eta\rvert < 3.2$	0.003×0.1^{a}
			0.025×0.025^{b}
			$0.003 - 0.025 \times 0.1^{c}$
			0.1×0.1^{d}
Sampling 2	$\lvert\eta\rvert < 1.475$	$1.375 < \lvert\eta\rvert < 3.2$	0.025×0.025
			0.075×0.025^{b}
			0.1×0.1^{d}
Sampling 3	$\lvert\eta\rvert < 1.35$	$1.5 < \lvert\eta\rvert < 2.5$	0.05×0.025
Tile calorimeter	barrel	extended barrel	
Sampling 1-2	$\lvert\eta\rvert < 1.0$	$0.8 < \lvert\eta\rvert < 1.7$	0.1×0.1
Sampling 3	$\lvert\eta\rvert < 1.0$	$0.8 < \lvert\eta\rvert < 1.7$	0.2×0.1
Hadronic end-cap			
Sampling 1-4	$1.5 < \lvert\eta\rvert < 3.2$		0.1×0.1^{e}
			0.2×0.2^{d}
Forward			
Sampling 1-3	$3.1 < \lvert\eta\rvert < 4.9$		0.2×0.2

$^{a}\lvert\eta\rvert < 1.4$, $^{b}1.4 < \lvert\eta\rvert < 1.475$, $^{c}1.375 < \lvert\eta\rvert < 2.5$, $^{d}2.5 < \lvert\eta\rvert < 3.2$, $^{e}1.5 < \lvert\eta\rvert < 2.5$

Table 1.4: Nominal calorimeters' performance goals and coverage for the ATLAS detector [6]

Detector component	**Required resolution** (σ_E / E)	η **coverage**
EM calorimeter	$10\%\sqrt{E} \oplus 0.7\%$	± 3.2 (± 2.5 for the trigger)
Had barrel / end-cap	$50\%\sqrt{E} \oplus 3\%$	± 3.2
Had forward	$100\%\sqrt{E} \oplus 3.1\%$	± 4.9

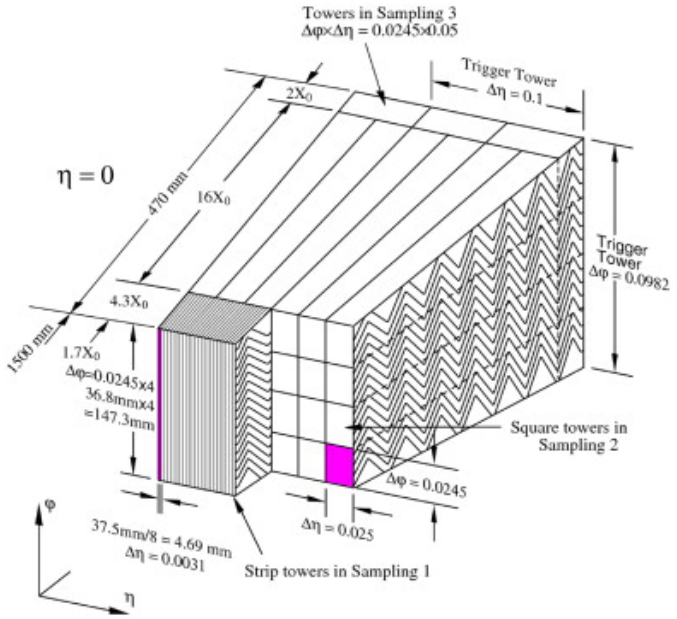

Figure 1.12: Schematic view of the accordion geometry [6]

rel calorimeter consists of two identical half-barrels, separated by a small gap (4 mm) at $z = 0$. Each end-cap calorimeter is mechanically divided into two coaxial wheels: an inner wheel covering the region $1.375 < |\eta| < 2.5$, and an outer wheel covering the region $2.5 < |\eta| < 3.2$.

Over the region devoted to precision physics ($|\eta| < 2.5$), the EM calorimeter is segmented into three longitudinal sections: strips, middle and back. While most of the energy of electrons and photons is collected in the middle, the fine granularity of the strips is necessary to improve the $\gamma - \pi^0$ discrimination. The back measures the tails of highly energetic electromagnetic showers, and helps to distinguish electromagnetic and hadronic deposits. For the end-cap inner wheel, the calorimeter is segmented in two longitudinal sections and has a coarser lateral granularity than for the rest of the acceptance.

Energy losses by particles crossing the material in front of the calorimeters (the cryostat, the solenoid and the 1-4 radiation-lengths thick Inner Detector) introduce an uncertainty in the energy measurements. To overcome this difficulty, the EM is complemented by an additional pre-sampler layer in front of the sampling portion (i.e. accordion) of the calorimetry. The pre-sampler is 11 mm (5 mm) thick in the barrel (end-cap) and includes fine segmentation in η. Unlike the rest of the

calorimetry, the pre-sampler has no absorber layer.

The transition region between the barrel and the end-cap EM calorimeters, $1.37 < |\eta| < 1.52$, is expected to have poorer performance because of the higher amount of passive material in front of the calorimeter, this region is often referred as crack region.

The LAr electronic calibration is done using pulse height samples, while the tiles signal is monitored by different systems. The response, i.e.the ratio of the reconstructed signal to the "true" signal, is checked using Cesium sources. Read-out electronics can be tested and calibrated by injecting charge into a single cell and finally the optical connections and photomultiplier tubes response can be checked with laser light.

1.5.2 Had Calorimeter

Two different techniques are used for the Had Calorimeter depending on the region: central and end-cap.

The Tile calorimeter (Tile) is placed directly outside the EM Calorimeter envelope in the central region. It uses a sampling technique with steel as absorber and scintillating tiles as active material. It is divided into a barrel ($|\eta| < 1.0$) and two extended barrels ($0.8 < |\eta| < 1.7$). Radially, the Tile goes from an inner radius of 2.28 m to an outer radius of 4.25 m. It is longitudinally segmented in three layers approximately 1.5, 4.1 and 1.8 interaction lengths thick for the barrel and 1.5, 2.6, and 3.3 interaction lengths for the extended barrel.

The Hadronic End-cap Calorimeter (HEC) consists of two independent wheels per end-cap, located directly behind the end-cap EM calorimeter and sharing the same LAr cryostats. It covers the region $1.5 < |\eta| < 3.1$, overlapping both with the Tile and Forward calorimeters. The HEC is a parallel plate copper - LAr sampling calorimeter. Each wheel is divided into two longitudinal segments, for a total of four layers per end-cap. The wheels closest to the interaction point are built from 25 mm parallel copper plates, while those further away use 50 mm copper plates. The outer radius of the copper plates is 2.03 m, while the inner radius is 0.475 m (except in the overlap region with the forward calorimeter where this radius becomes 0.372 m). Radiation hardness and cost effectiveness drove the choice for this technology and the calorimeter geometry.

1.5.3 Forward Calorimeter

The Forward Calorimeter (FCal) covers the $3.1 < |\eta| < 4.9$ region and is another detector based on LAr technology. It is integrated into the end-cap cryostats and is approximately 10 interaction lengths deep.

It consists of three 45 cm thick independent modules in each end-cap and provides both electromagnetic and hadronic energy measurements: the first module's absorber is copper, which is optimized for electromagnetic measurements, while for the two are made of tungsten, which is used to measure predominantly the energy of hadronic interactions. Although the system is not used for precision measurements, it provides valuable information for missing transverse energy determination and reconstruction of very forward jets.

Radiation tolerance is extremely important in this region, where the expected radiation dose is very high. Therefore the electrode structure is different from the accordion geometry, consisting in a structure of concentric rods and tubes parallel to the beam axis.

1.6 Muon Spectrometer

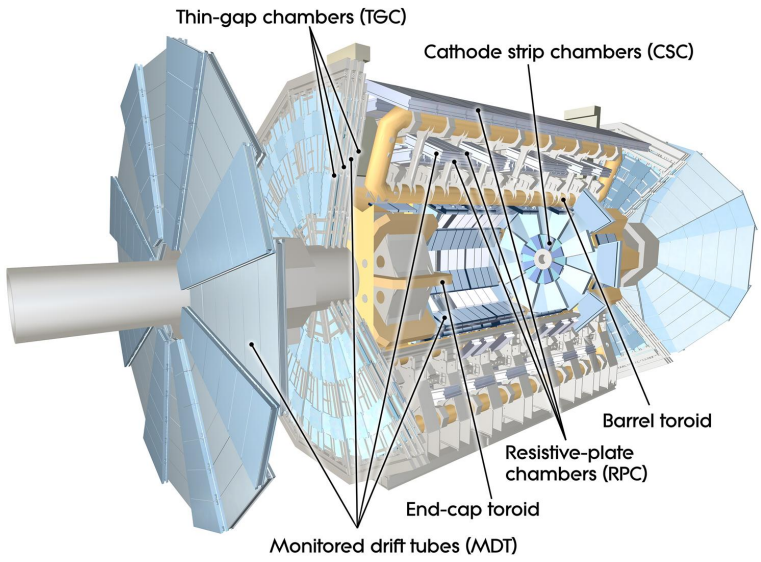

Figure 1.13: Schematic view of the ATLAS Muon Spectrometer [6]

The Muon Spectrometer (MS) is the largest and outermost part of the AT-

LAS detector: it has been designed to detect charged particles exiting the barrel and end-cap calorimeters and provide an independent measurement of their momenta. The degradation of resolution due to multiple scattering is minimized because the muons travel mainly through air. The MS is immersed in a toroidal magnetic field and is composed by separated layers of wired chambers: in the barrel region ($|\eta| < 1.0$), the muon chambers are arranged in three cylindrical layers (sectors), while in the end-cap ($1.4 < |\eta| < 2.7$) they form three vertical walls. The transition region ($1.0 < |\eta| < 1.4$) is instrumented with four layers. The layout of the Muon Spectrometer is also shown in figure 1.13.

The muon system has two different functions: high precision tracking of muons and trigger. These goals have been achieved by deploying a mixture of chambers based on four different technologies. The choice of different types of chambers has been driven by criteria of rate capability, granularity, aging and radiation hardness. The measurement of the track bending is provided in most of the η regions by the Monitored Drift Tubes (MDT), while at large η, the higher granularity Cathode Strip Chambers (CSC) are used. The chambers for the first level of the trigger system need a very fast response. They covers the region $|\eta| < 2.4$. The Resistive Plate Chambers (RPC) are used in the barrel region, while the Thin Gap Chambers (TGC) are used in the end-cap.

The reconstruction efficiency and resolution of the Muon Spectrometer were measured using cosmic ray events in 2008 and 2009 [12]. The reconstruction efficiency, integrated over the detector acceptance, is $\sim$ 94%. At $|\eta| = 0$ there is a gap in the detector for cable routing. If the region of the detector near this crack is excluded, the reconstruction efficiency is increased to 97%. The transverse momentum resolution was determined from this data to be

$$\frac{\sigma_{p_T}}{p_T} = \frac{0.29\ \text{GeV}}{p_T} \oplus 0.043 \oplus 4.1 \times 10^{-4}\ \text{GeV}^{-1} \times p_T \tag{1.6}$$

for transverse momentum (p_T) between 5 and 400 GeV.

A brief description of the technologies used in the muon chambers follows.

Monitored Drift Tubes

The basic element of the MDTs is a pressurized drift tube: the passage of a charged particle ionizes the gas (93% Ar / 7% CO_2) within the chamber and the liberated electrons are collected by a central anode wire (50 μm diameter made of tungsten-rhenium). In the vicinity of the wire, an avalanche process takes place, inducing

measurable signals which are read out by the on-chamber electronics. The charge information is used for noise discrimination. The arrival time of the signal can be interpreted as a drift-radius, using a calibration function to correct for the non-linear drift velocity in the gas mixture. Single hit resolutions of the order of 80 μm are achieved, with an efficiency around 96%. The chamber resolutions are of the order of 35 μm. Each chamber is equipped with an optical system to monitor its deformations.

MDT chambers have a projective design, covering a total area of 5500 m^2. They are formed of six or eight layers of drift tubes, with diameters of 29.970 mm.

Cathode Strip Chambers

The performance of MDTs is degraded at rates above 150 Hz/cm^2, which will be exceeded in the first layer of the forward region ($|\eta| > 2$). In this range up to $|\eta| < 2.7$, Cathode Strip Chambers provide high spatial and time resolutions with high-rate capability. CSCs consist of multi-wire proportional chambers made of radial anode wires and cathode planes segmented into orthogonal strips. Strips in the plane perpendicular to the wires provide the precision coordinate (η) and the ones parallel to the wire give the second coordinate (ϕ) information. Each chamber is composed by 4 layers with 5 mm gaps filled with with Ar / CO_2 (80% / 20%). The wire plane is located at the center of each gap, with a wire pitch of 2.5 mm, equal to the anode-cathode spacing. The wires are 30 μm in diameter and operate at 1900 V. This result in drift times of less than 40 ns, with an associated precision around 7 ns. The expected spatial resolutions are of the order of 40 μm in R and 5 mm in ϕ.

Resistive Plate Chambers

Resistive Plate Chambers are gaseous parallel-plate detectors, with a 2 mm gap created by insulating spacers between the electrodes. The gap is filled with a mixture of $C_2H_2F_4$ / Iso-C_4H_{10}/SF_6 (94.7/5/0.3), which allows relatively low operating voltage, non-flammability and low cost. The electric field between the plates ($\sim$ 4.9 kV/mm) creates avalanches in front of the anodes when an ionizing track crosses the chamber. Induced signals are read out via capacitive coupling to metallic strips, mounted on the outer faces of the resistive plates. Spatial resolution around 10 mm is expected for both coordinates, with timing resolutions below 2 ns. Three layers of RPC provide the trigger and second coordinate mea-

surement in the barrel region. Each station consists of two independent layers, each measuring η and ϕ, such that a track going through all three stations delivers six measurements per coordinate. The redundancy decreases fake rates from noise hits and increases the triggering efficiency.

Thin Gap Chambers

TGCs have the same function as RPCs, providing trigger and second coordinate measurement in the end-cap. Each chamber is a multi-wire proportional chamber filled with a highly quenching gas mixture of CO_2 and n-pentane. It operates in a quasi-saturated mode, preventing the occurrence of streamers in all operating conditions. Wire-to-cathode distance of 1.4 mm and wire-to-wire distance of 1.8 mm lead to very good time resolution. Including the variation of the propagation time, signals arrive with 99% probability inside a time window of 25 ns. The radial bending coordinate is measured by the TGC wire groups, while the azimuthal coordinate is determined by the radial strips.

1.7 Forward detectors

The luminosity measurement from the ID is complemented by four additional devices.

The Luminosity Cherenkov Integrating Detectors (LUCID) are placed at a distance of 17 m on each side of the interaction region, covering the range $5.6 < |\eta| < 6.0$. They detect inelastic proton-proton scattering in the forward direction and provide the main online relative-luminosity monitor for ATLAS. They are also used to check for possible beam losses, before collisions are delivered by the LHC.

The Beam Condition Monitor (BCM), placed at $|\eta| = 4.2$, consists of four small diamond sensors arranged around the beam-axis in a cross pattern designed mainly to monitor background levels and to request an aborting procedure in case of beam losses.

The Absolute Luminosity For ATLAS (ALFA) is another detector used for luminosity measurement. It is located at ± 240 m from the interaction point and consists of scintillating fibre trackers located inside Roman pots which are designed to approach as close as 1 mm from the beam.

The last detector is Zero-Degree Calorimeter (ZDC). It is located at ± 140 m from the interaction point, just beyond the point where the common straight-

section vacuum-pipe divides back into two independent beam-pipes. The ZDC modules consist of layers of alternating quartz rods and tungsten plates which measure neutral particles at $|\eta| \geq 8.2$.

1.8 ATLAS performance summary

The general performance goals for ATLAS are summarized in table 1.5.

Table 1.5: General performance goals of the ATLAS detector. Note that, for high-p_T muons, the muon spectrometer performance is independent of the inner-detector system.

Detector component	Resolution	Acceptance
Inner Detector	$\sigma_{p_T}/p_T = 0.05\% p_T \oplus 1\%$	$\lvert\eta\rvert < 2.5$
EM Calorimeter	$\sigma_E/E = 10\%/\sqrt{E} \oplus 0.7\%$	$\lvert\eta\rvert < 3.2$
Hadronic Calorimeter	$\sigma_E/E = 50\%/\sqrt{E} \oplus 3\%$	$\lvert\eta\rvert < 3.2$
Forward Calorimeter	$\sigma_E/E = 100\%/\sqrt{E} \oplus 10\%$	$3.1 < \lvert\eta\rvert < 4.9$
Muon Spectrometer	$\sigma_{p_T}/p_T = 10\%$ ($p_T = 1$ TeV)	$\lvert\eta\rvert < 2.7$

1.9 Trigger, data acquisition and control systems

The Trigger and Data Acquisition (collectively TDAQ) systems, the timing and trigger-control logic, and the Detector Control System (DCS) are partitioned into sub-systems, typically associated with sub-detectors, which have the same logical components and building blocks.

The design luminosity of the LHC of 10^{34} cm^{-2}s^{-1} with a bunch-spacing of 25 ns corresponds to a collision rate at the interaction point inside the ATLAS detector of roughly 40 MHz. This large amount of data, corresponding to an extremely high theoretical raw data rate of about 1.5 PBs^{-1}, can neither be fully reconstructed nor stored for further analysis. Therefore, the amount of data collected by the detector has to be reduced down to approximately 400 Hz within a very short time frame. Since only a small fraction of the collisions produced are actually interesting for analysis, the ATLAS trigger [13] has been designed to reduce the initial data rate by several orders of magnitude by selecting these possibly interesting events. In order to do so, the trigger system consists of three levels

of increasingly refined and stepwise event selection shown in fig. 1.14: Level-1 (L1), Level-2 (L2), and Event Filter (EF). The last two form together the so-called High-Level Trigger (HLT).

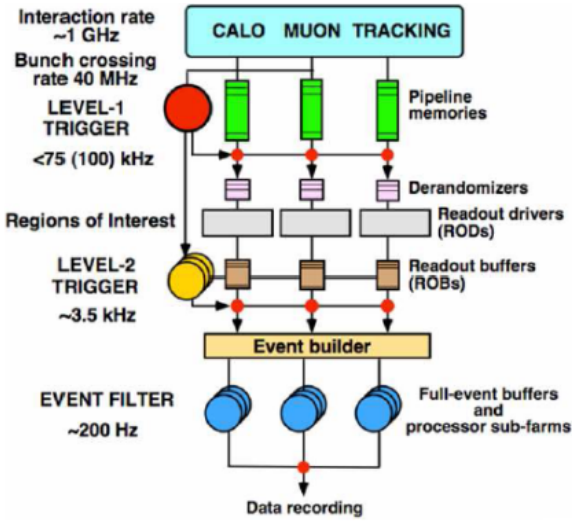

Figure 1.14: The trigger and read-out chain of the ATLAS detector. The data recording rate at the EF trigger has been updated to approximately 400Hz.

1.9.1 Trigger system

The L1 trigger is designed to unambiguously identify the bunch-crossing of interest and perform the initial event selection based on reduced granularity information from a subset of the detectors (calorimeter and muon spectrometer). It searches for high transverse-momentum muons, electrons, photons, jets, and τ-leptons decaying into hadrons, as well as large missing and total transverse energy. High transverse-momentum muons are identified using trigger chambers in the barrel and end-cap regions of the spectrometer. Calorimeter selections are based on reduced-granularity information from all the calorimeters. Results from the L1 muon and calorimeter triggers are processed by the central trigger processor, where a set of criteria, referred to as trigger menu, can be programmed with up to 256 distinct L1 items, each or these being a combination of requirements on the input data. Pre-scaling of trigger menu items is also available, allowing optimal use of the bandwidth as luminosity and background conditions change. Upon the event being accepted by the L1 trigger, the information about the geometric lo-

cation (η and ϕ) of L1 trigger objects (retained in the muon and calorimeter trigger processors) is sent to the next level as Regions-of-Interest (RoI). The RoI data include information on the type of feature identified and the criteria passed, e.g. a threshold. This information is subsequently used by the HLT.

The L2 selection uses RoI information on coordinates, energy, and type of signatures to limit the amount of data which must be transferred from the detector readout. The L2 trigger algorithms are software-based and the system is designed to provide an event rejection factor of about 30, with an average throughput per farm node of about 200 Hz. The L2 menus are designed to reduce the trigger rate to approximately 3.5 kHz, with an event processing time of about 40 ms, averaged over all events. The L2 trigger decisions are applied in a series of steps, each refining existing information by acquiring additional data from different sub-detectors.

The EF is the last step of the chain. It uses off-line algorithms, adapted for the on-line time requirements, to reconstruct the objects, and to take its decision. The EF has about four seconds to take the decision, and the output rate is of about 400 Hz. The events selected are written to mass storage for the subsequent off-line analysis.

1.9.2 Readout architecture and data acquisition

In parallel to the trigger, two independent, complementary and interacting systems are responsible for the data taking and control the experiment infrastructure: the data acquisition system (DAQ), and the Detector Control System (DCS).

After an event is accepted by the L1 trigger, the data from the pipe-lines are transferred off the detector to the Readout Drivers (RODs). Digitized signals are formatted as raw data prior to being transferred to the DAQ system. The RODs are detector-specific functional elements of the front-end systems, which gather information from several front-end data streams. Although each sub-detector uses specific front-end electronics and ROD's, these components are built from standardized blocks and are subject to common requirements. The front-end electronics sub-system includes different functional components:

- the front-end analogue or analogue-to-digital processing
- the L1 buffer in which the (analogue or digital) information is retained for a time long enough to accommodate the L1 trigger latency
- the derandomising buffer in which the data corresponding to a L1 trigger

accept are stored before being sent to the following level. This element is necessary to accommodate the maximum instantaneous L1 rate without introducing significant dead time (maximum 1%)

- the dedicated links or buses which are used to transmit the front-end data stream to the next stage

The RODs follow some general ATLAS rules, including the definition of the data format of the event, the error detection/recovery mechanisms to be implemented, and the physical interface for the data transmission to the DAQ system. The first stage of the DAQ, the readout system, receives and temporarily stores the data in local buffers. It is subsequently solicited by the L2 trigger for the event data associated to RoIs. Those events selected by the L2 trigger are then transferred to the event-building system and subsequently to the Event Filter for final selection. Events selected by the Event Filter are moved to permanent storage at the CERN computer centre. In addition to the movement of data, the data acquisition also provides for the configuration, control and monitoring of the hardware and software components which together provide the data-taking functionality enabling diagnostics and error recovery, with the capability of removing or re-enabling individual parts without stopping the full acquisition.

The Detector Control System permits the coherent and safe operation of the ATLAS detector hardware, and serves as a homogeneous interface to all subdetectors and to the technical infrastructure of the experiment. It controls, continuously monitors and archives the operational parameters, signals any abnormal behavior to the operator, and allows automatic or manual corrective actions to be taken. Typical examples are high and low-voltage systems for detector and electronics, gas and cooling systems, magnetic field, temperatures, and humidity. The DCS also enables bi-directional communication with the data acquisition system in order to synchronize the state of the detector with data-taking. It also handles the communication between the sub-detectors and other systems which are controlled independently, such as the LHC accelerator, the CERN technical services, the ATLAS magnets, and the detector safety system.

CHAPTER 2

A Natural extension of the Standard Model

The Standard Model (SM) [14, 15] of particle physics describes the known phenomena below an energy scale of the order of 100 GeV. For decades, the SM has been subject to thorough experimental scrutiny and has been found to be in agreement with experimental measurements, tested in some cases to a precision greater than 0.1%. However, if we consider higher energies up the to Grand Unified Theory (GUT) ($\Lambda_{\text{GUT}} \approx 10^{16}$ GeV) or Planck scale ($\Lambda_{\text{Planck}} = G_{\text{N}}^{-1/2} \approx 10^{19}$ GeV where G_{N} is the gravitational constant), we encounter a number of conceptual problems.

The first problem comes from the very large difference between the electroweak energy scale and the GUT or the Planck scales. This is called hierarchy problem. This affects the Higgs boson mass: without any additional symmetry stabilizing the electroweak scale by providing a cancellation mechanism, the Higgs mass receives large corrections by the one-loop diagram contributions.

Furthermore, cosmological observations point out the need to include Dark Matter (DM) in our description of the universe. A successful DM candidate must be stable, electrically neutral, weakly interacting and massive (non-relativistic): this excludes any known Standard Model particle.

Moreover, unification of gravity in the framework of quantum field theory is not achieved in the SM.

There are several other problems not mentioned here (neutrino masses, matter-antimatter asymmetry, fermion masses hierarchy, etc.), but all of them lead to the idea that the SM is an "effective theory" that works fine at the electroweak scale, but is incomplete when it is extended to higher energies.

2.1 The hierarchy problem and naturalness

Typical energies in SM processes at the electroweak symmetry breaking scale go up to the order of 100 GeV. If we take into account the energy scale where quantum gravity is not negligible anymore, we get to the Planck scale. The huge difference between these two energy scales is known as hierarchy problem and is deeply related to the structure of the Higgs scalar field.

The mass of the Higgs boson receives quantum loop corrections from all the particles which couple to the Higgs field. Any SM fermion f couples to the Higgs H with a Lagrangian term $-\lambda_f H\bar{f}f$, shown in fig. 2.1 (a). The SM Higgs boson mass is hence given by

$$m_H^2 \approx m_{H0}^2 - \frac{|\lambda_f|^2}{8\pi^2}\Lambda^2 + ... \tag{2.1}$$

where m_H is the physical Higgs boson mass, m_{H0} is the bare Higgs mass and λ_f is the Yukawa coupling of f. Λ^2 is the ultraviolet momentum cut-off used to regulate the loop integral. Hence, the Higgs boson mass diverges quadratically in Λ. The ellipses represent terms proportional to m_f^2, which grow at most logarithmically with Λ. There is nothing that protects the Higgs mass from these quadratic divergences. Furthermore the SM quarks, leptons and the electroweak gauge bosons obtain masses from the Higgs vacuum expectation value $\langle H \rangle$, so the entire mass spectrum of the MS is sensitive to the cutoff Λ.

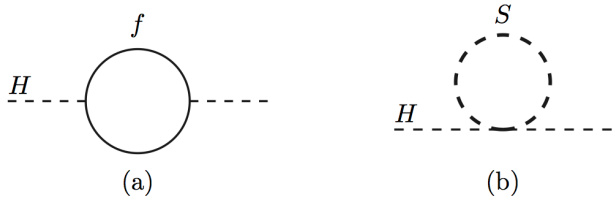

Figure 2.1: One-loop quantum corrections to the Higgs squared mass parameter m_H^2 , due to (a) a Dirac fermion f, and (b) a scalar S. [16]

Theories are expected to provide *natural* explanations of experimental observations. A quantitative definition of the naturalness of a particle physics theory can be given with respect to the amount of fine-tuning needed to achieve the electroweak symmetry breaking at the observed energy scale, represented by the Z boson mass m_Z [17, 18]. Once a set of independent and continuously variable parameters $\{a_i\}$ representing the theory is chosen, it is possible to compute another

set of parameters $\mathcal{N}_i$. These parameters, defined as

$$\mathcal{N}_i \equiv \left| \frac{\partial \ln m_Z^2}{\partial \ln a_i^2} \right| = \left| \frac{a_i^2}{m_Z^2} \frac{\partial m_Z^2}{\partial a_i^2} \right| \tag{2.2}$$

measure the sensitivity of the electroweak scale to variations in the fundamental parameters. An overall measure of the naturalness of a theory is given by $\mathcal{N} = max\{\mathcal{N}_i\}$.

The requirements of a Higgs mass of order the electroweak scale and the SM extension up to some unification scale (i.e. $\Lambda = 10^{15}$ GeV) imply a very large fine-tuning of the quantum loop corrections and correspondingly a very low degree of naturalness.

2.2 Supersymmetry as solution to the hierarchy problem

The Supersymmetry (SUSY) [19, 20, 21, 22] is a theory that associates a fermionic (bosonic) partner to each SM boson (fermion). The generators of this new symmetry are the Majorana spinors $Q_\alpha (\alpha = 1, ..., 4)$ that act on the physical states changing their spin of a quantity $\pm 1/2$.

This fermionic generators satisfy the following relations:

$$[Q_\alpha, M^{\mu\nu}] = i(\sigma^{\mu\nu})_\alpha^\beta Q_\beta \tag{2.3}$$

$$\{Q_\alpha, \bar{Q}_\beta\} = -2(\gamma_\mu)_{\alpha\beta} P^\mu \tag{2.4}$$

$$[Q_\alpha, P^\mu] = \{Q_\alpha, Q_\beta\} = \{\bar{Q}_\alpha, \bar{Q}_\beta\} = 0 \tag{2.5}$$

with

$$\sigma_{\mu\nu} = \frac{1}{4}[\gamma_\mu, \gamma_\nu] \tag{2.6}$$

$$\bar{Q}_\alpha = Q_\alpha^T \gamma^0 \tag{2.7}$$

where γ_μ are the usual 4×4 Dirac matrices, P^μ is the momentum operator and $M^{\mu\nu}$ is the Lorentz group generator.

The Standard Model hierarchy problem presented in Section 2.1 is solved when considering the supersymmetric theory. If one assumes there exists a heavy scalar particle S with mass m_S that couples to the Higgs with a Lagrangian term $-\lambda_S |H|^2 |S|^2$,

shown in fig. 2.1 (b), the scalar loop corrections would give a contribution to the Higgs mass of

$$\Delta m_H^2 = \frac{\lambda_s}{16\pi^2}\Lambda^2 + ... \tag{2.8}$$

where the first term diverges quadratically in Λ and the ellipses correspond to terms proportional to m_S^2, which grow at most logarithmically with Λ.

Comparing Eq. 2.1 and Eq. 2.8, we can see that if each of the quarks and leptons of the SM is accompanied by two complex scalars with $\lambda_S = |\lambda_f|^2$, the quadratic divergences coming from these two terms would cancel each other independently of the masses and of the magnitude of the couplings.

The reason is that every Standard Model fermion f has two scalar SUSY partners S, that also couple to the Higgs, contributing with a mass correction given by Eq. 2.8. Higher order interactions also contribute to the Higgs mass renormalization (although not quadratically divergent), which depends on the mass splitting between the fermion and the scalar. The terms that do not cancel are of the form:

$$\Delta m_H^2 = \frac{\lambda}{16\pi^2}\left[m_f^2 \log\left(\frac{\Lambda}{m_f}\right) - m_S^2 \log\left(\frac{\Lambda}{m_S}\right)\right] \tag{2.9}$$

where λ stands for the various dimensionless couplings, and other smaller contributions have been omitted. In order to avoid considerable fine tuning and keep naturalness, these corrections must not be much greater than the mass of the SM Higgs. Using $\Lambda \approx M_P$ and $\lambda \approx 1$ one finds that the masses of at least the lightest few superpartners should be of about 1 TeV, in order to provide a Higgs VEV resulting in $m_W \approx 80$ GeV and $m_Z \approx 91$ GeV without any miraculous cancelation within the SUSY framework. Thus, one associates

$$\mathcal{O}\left(|m_S^2 - m_f^2|\right) \leq \mathcal{O}\left((1\text{TeV})^2\right) \tag{2.10}$$

as the scale where the SM is no longer valid and must be substituted by its supersymmetric extension. Therefore, as long as the mass splitting between scalars and fermions is "small", no unnatural cancellations will be required and the theory can be considered "natural". In this manner, a theory with nearly degenerate fermions and scalars with equal couplings solves the hierarchy problem.

2.3 The Minimal Supersymmetric Standard Model

The minimal supersymmetric extension of the Standard Model is referred to as the Minimal Supersymmetric Standard Model (MSSM). Since there are no candidates for supersymmetric partners within the already observed particles, the

entire particle spectrum must be doubled, placing the observed particles and the new hypothetical superpartners within supermultiplets.

Each of the known fundamental particles is included in either a chiral or gauge supermultiplet, and must have a superpartner with the spin differing by 1/2 unit:

- Chiral (or scalar) supermultiplets: a massless spin-1/2 Weyl fermion with two spin helicity states and two real scalar fields, assembled into a complex scalar field.

- Gauge (or vector) supermultiplets: a massless real spin-1 vector boson and a massless spin-1/2 Weyl fermion.

The chiral and gauge supermultiplets are summarized in tables 2.1 and 2.2. None of the superpartners of the Standard Model particles have been discovered so far, therefore supersymmetry has to be broken in the vacuum state chosen by Nature.

The interactions of SUSY particles are basically obtained from the Standard Model ones, by replacing any two lines in a vertex by their SUSY partners; for example, the gluon-quark-quark and gluino-quark-squark couplings are the same. See [23, 24, 25, 16] for the construction of the complete Lagrangian.

Table 2.1: Chiral supermultiplets in the Minimal Supersymmetric Standard Model. The spin-0 fields are complex scalars, and the spin-1/2 fields are left-handed two-component Weyl fermions.

		spin 0	**spin 1/2**	**SU(3)$_C$, SU(2)$_L$, U(1)$_Y$**
squarks, quarks	Q	$(\tilde{u}_L \ \tilde{d}_L)$	$(u_L \ d_L)$	$(3, 2, \frac{1}{6})$
($\times$3 generations)	$\overline{u}$	$\tilde{u}_R^*$	$\tilde{u}_R^\dagger$	$(\overline{3}, 1, -\frac{2}{3})$
	$\overline{d}$	$\tilde{d}_R^*$	$\tilde{d}_R^\dagger$	$(\overline{3}, 1, \frac{1}{3})$
sleptons, leptons	L	$(\tilde{\nu} \ e_L)$	$(\nu \ e_L)$	$(1, 2, -\frac{1}{2})$
($\times$3 generations)	$\overline{e}$	$\tilde{e}_R^*$	$\tilde{e}_R^\dagger$	$(1, 1, 1)$
Higgs, higgsinos	H_u	$(H_u^+ \ H_u^0)$	$(\tilde{H}_u^+ \ \tilde{H}_u^0)$	$(1, 2, +\frac{1}{2})$
	H_d	$(H_d^0 \ H_d^-)$	$(\tilde{H}_d^0 \ \tilde{H}_d^-)$	$(1, 2, -\frac{1}{2})$

Table 2.2: Gauge supermultiplets in the Minimal Supersymmetric Standard Model.

	spin 1/2	**spin 1**	**SU(3)$_C$, SU(2)$_L$, U(1)$_Y$**
gluino, gluon	$\tilde{g}$	g	$(8,1,0)$
winos, W bosons	$\tilde{W}^{\pm}$ $\tilde{W}^0$	$W^{\pm}$ W^0	$(1,3,0)$
bino, B boson	$\tilde{B}^0$	B^0	$(1,1,0)$

2.3.1 R-parity

In the Standard Model Lagrangian, baryon and lepton number are conserved by the requirements of gauge invariance and renormalizability. In supersymmetric theories it is possible to violate both, potentially leading to weak-scale proton decay.

The unwanted terms can be eliminated by imposing invariance under a new symmetry, known as R-parity. This new discrete symmetry is defined for each particle as:

$$R = (-1)^{3(B-L)+2S} \tag{2.11}$$

where B, L, and S are respectively the baryon number, the lepton number, and the spin. Hence R = +1 for all Standard Model particles and R = -1 for all SUSY particles.

This has three important phenomenological consequences:

- The lightest sparticle with R = -1, referred to as the lightest supersymmetric particle (LSP) must be stable.
- Each sparticle other than the LSP must eventually decay into a state that contains an odd number of LSPs.
- Sparticles can only be produced in even numbers.

R-parity conservation holds automatically in many GUT models under rather general assumptions. Alternatively, weak-scale proton decay can also be avoided by imposing either baryon or lepton number conservation.

2.3.2 Supersymmetry breaking

In a theory with exact supersymmetry fermions and their bosonic superpartners must be degenerate in mass, however the experimental observations show that

the observed particle spectrum does not satisfy this requirement. Thus, if SUSY is realized in Nature, it must be broken.

Supersymmetry is broken "by hand" by adding to the Lagrangian all possible soft terms consistent with SU(3) $\otimes$ SU(2) $\otimes$ U(1) gauge invariance. Unlike the supersymmetry-preserving part of the Lagrangian, many new parameters are introduced in the MSSM by the soft supersymmetry-breaking terms (compatible with gauge invariance and R-parity conservation) such as mass terms for all the superpartners and trilinear A terms:

$$\begin{aligned} L_{\text{SOFT}} = \quad & -m_{H_d}^2|H_d|^2 - m_{H_u}^2|H_u|^2 + \mu B\epsilon_{ij}(H_d^i H_u^j + h.c.) \\ & -\tfrac{1}{2}M_1\tilde{\bar{B}}\tilde{B} - \tfrac{1}{2}M_2\tilde{\bar{W}}\tilde{W} - \tfrac{1}{2}M_3\tilde{\bar{g}}\tilde{g} \\ & -M_{\tilde{Q}}^2(\tilde{u}_L^*\tilde{u}_L + \tilde{d}_L^*\tilde{d}_L) - M_{\tilde{U}}^2 u_R^* u_R - M_{\tilde{D}}^2 d_R^* d_R \\ & -M_{\tilde{L}}^2(\tilde{l}_L^*\tilde{l}_L + \tilde{\nu}_L^*\tilde{\nu}_L) - M_{\tilde{E}}^2 l_R^* l_R \\ & -\epsilon_{ij}(-\lambda_u A_u H_u^i \tilde{Q}^j \tilde{u}_R^* + \lambda_d A_d H_d^i \tilde{Q}^j \tilde{d}_R^* + \lambda_l A_E H_d^i \tilde{L}^j \tilde{l}_R^*) \end{aligned} \tag{2.12}$$

where Q, L, H_u and H_d denote $SU(2)$ weak doublets as in table 2.1 and a summation over generations is implied. There are 105 masses, phases and mixing angles in the MSSM [26] that cannot be removed by redefining the phases and flavour basis from the quark and lepton supermultiplets.

Many of these parameters are however severely restricted by experimental observations. As consequence, a phenomenologically viable MSSM can be defined by making the following three assumptions:

- All the soft SUSY-breaking parameters are real and therefore there is no new source of CP-violation generated, in addition to the one from the CKM matrix.
- The matrices for the sfermion masses and for the trilinear couplings are all diagonal, implying the absence of flavour-changing neutral current processes at the tree-level.
- First and second sfermion generation universality at low energy from constraints on experimental particle masses.

These assumptions reduce the total of 105 parameters to 22: the ratio of the VEVs of the two-Higgs doublet fields, two Higgs mass parameters squared, three gaugino mass parameters, five first/second generation sfermion mass parameters, five third generation sfermion mass parameters, three first/second generation trilinear couplings, and three third generation trilinear couplings.

2.3.3 The mass spectrum

The superpartners listed in tables 2.1 and 2.2 are not necessarily the mass eigenstates of the MSSM. After electroweak symmetry breaking and supersymmetry breaking effects are included, particles with the same quantum numbers will in general mix. The resulting masses and mixings of the superpartners are presented next.

Higgs sector

The Higgs scalar fields in the MSSM consist of two complex $SU(2)_L$-doublets, H_u and H_d, or eight real, scalar degrees of freedom. After the electroweak symmetry is broken, three of them are the Nambu-Goldstone bosons, which become the longitudinal modes of the Z and $W^\pm$ massive vector bosons. The remaining five degrees of freedom yield the physical Higgs bosons of the model:

- $H^\pm$: a charged Higgs boson pair
- A^0: a CP-odd neutral Higgs boson
- H^0, h^0: CP-even neutral Higgs bosons (with h^0 being lighter by convention)

If $m_{A^0} \gg m_Z$ (decoupling limit), the particles A^0, H^0 and $H^\pm$ are much heavier than h^0, nearly degenerated and decoupled from low-energy experiments.

In contrast, the mass of h^0 is upper bounded. The bound is found to be $m_{h^0} \lesssim$ 135 GeV, consistent with the experimental observation. This bound can be weakened if all the couplings in the theory are required to remain perturbative up to the unification scale, or if the top squarks are heavier than ~ 1 TeV, but the upper bound rises only logarithmically with the soft masses in the loop corrections. Thus supersymmetry at the electroweak scale predicts that at least one of the Higgs scalar bosons must be light.

Charginos and neutralinos

The gauginos and Higgsinos mix to form two spin 1/2 charged particles called "charginos" $\tilde{\chi}_i^\pm$ with the matrix in the (W^+, H^+) basis:

$$\begin{pmatrix} M_2 & \sqrt{2}M_W \sin\beta \\ \sqrt{2}M_W \cos\beta & \mu \end{pmatrix} \tag{2.13}$$

and four spin-1/2 neutral particles called "neutralinos" $\tilde{\chi}_i^0$ with the mass matrix in the (B, W^0, H_d, H_u) basis:

$$\begin{pmatrix} M_1 & 0 & -M_Z \cos\beta \sin\theta_W & M_Z \sin\beta \sin\theta_W \\ 0 & M_2 & M_Z \cos\beta \cos\theta_W & M_Z \sin\beta \cos\theta_W \\ -M_Z \cos\beta \sin\theta_W & M_Z \cos\beta \cos\theta_W & 0 & -\mu \\ M_Z \sin\beta \sin\theta_W & -M_Z \sin\beta \cos\theta_W & -\mu & 0 \end{pmatrix} \tag{2.14}$$

where, in both formulae, θ_W is the Weinberg angle and $\tan\beta$ is the ratio of the two v.e.v's of the two Higgs doublets. The lightest neutralino, χ_1^0, is usually assumed to be the LSP (since it is the only MSSM particle that can make a good dark matter candidate).

Generally, the mass eigen-states and their corresponding eigenvalues are complicated mixtures of the gauge interaction-eigenstates and the phenomenology of the different SUSY models strongly depends on this mixing. However, in most models of supersymmetry breaking it is possible to write the following relation:

$$\frac{M_1}{\alpha_1} = \frac{M_2}{\alpha_2} = \frac{M_3}{\alpha_3} \tag{2.15}$$

with the mass term μ that is of order of $M_{\tilde{g}}$. The consequence is that the two lighter neutralinos and the lighter chargino are dominantly gaugino, while the heavier states are dominantly Higgsino and weakly coupled to the first two generations.

Gluino

The gluino is a color octet fermion, so it cannot mix with any other particle in the MSSM (even if R-parity is violated). The gluino mass parameter (M3) is related to the bino and wino mass parameters (M1 and M2, respectively), by Eq. 2.15 with an approximate 6:2:1 (M3:M2:M1) ratio [?]. Therefore, in models where relation 2.15 holds, the gluino is expected to be heavier that the lighter neutralinos and charginos.

Squarks and sleptons

Concerning the sfermion sector, while chiral fermions f_L, f_R must have the same mass by Lorentz invariance, their scalar partners $\tilde{f}_L$, $\tilde{f}_R$ instead may have separate masses. Their squared mass matrix gets off-diagonal contributions proportional to the fermion mass with the result that this left-right mixing is only important

for the third generation. These eigenstates are called $\tilde{t}_{1,2}$, $\tilde{b}_{1,2}$ and $\tilde{\tau}_{1,2}$ (top and bottom squarks, stau).

2.3.4 A typical natural spectrum

The direct inputs from the LHC experiments have already presented strong limits on the squarks of the first two generations, constraining them to be heavier than 1 TeV. Naturalness points towards the possibility that the squark soft masses are not flavor degenerate, therefore shifting the focus on the particles that give the largest contributions to the Higgs mass corrections: the higgsino, the top squark (and left-handed bottom squark due to the SM weak isospin symmetry) and gluino [27]. A possible natural SUSY spectrum is shown in Fig. 2.2.

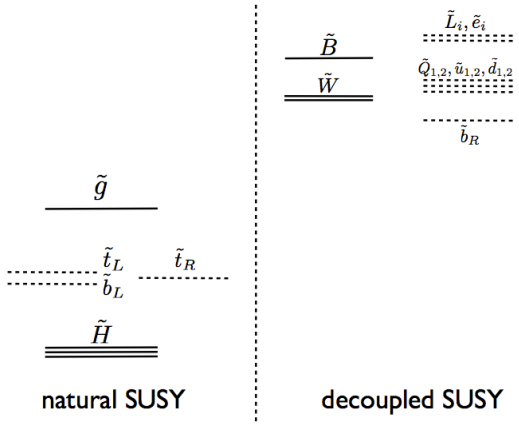

Figure 2.2: Natural electroweak symmetry breaking constrains the superpartners on the left to be light. Meanwhile, the superpartners on the right can be heavy, $m \gg$ 1 TeV, without spoiling naturalness. [27]

The naturalness in the MSSM can be summarized by:

$$-\frac{m_Z^2}{2} = |\mu|^2 + m_{H_u}^2 \tag{2.16}$$

The direct consequence of this equation is that higgsinos must be light because their mass is directly controlled by μ. If we define

$$\Delta \equiv \frac{2\delta m_H^2}{m_h^2} \tag{2.17}$$

with $m_h^2 = -2m_H^2$ as a measure of fine-tuning, we get that

$$|\mu| \leq 200\,\text{GeV}\left(\frac{m_h}{125\,\text{GeV}}\right)\left(\frac{\Delta^{-1}}{20\%}\right)^{-1/2} \tag{2.18}$$

At loop level we find additional constraints. The Higgs potential is corrected by both gauge ($A_t y_t \tilde{q}_3 \tilde{u}_3 H_u$) and Yukawa ($-y_t \tilde{q}_3 u_3 H u$) interactions, with the largest contribution being the top quark-squark loop. This is given by

$$\delta m_{H_u}^2|_{\tilde{t}} = -\frac{3}{8\pi^2} y_t^2 \left(m_{Q_3}^2 + m_{u_3}^2 + |A_t|^2\right) \log\left(\frac{\Lambda}{\text{TeV}}\right) \tag{2.19}$$

where Λ is the scale at which sfermion masses are generated. This translates in a boundary on the heaviest of the top squarks via

$$\sqrt{m_{\tilde{t}_1}^2 + m_{\tilde{t}_2}^2} \leq 600\,\text{GeV}\frac{\sin\beta}{(1+x_t^2)^{1/2}}\left(\frac{\log(\Lambda/\text{TeV})}{3}\right)^{-1/2}\left(\frac{m_h}{125\,\text{GeV}}\right)\left(\frac{\Delta^{-1}}{20\%}\right)^{-1/2} \tag{2.20}$$

where $x_t = A_t/\sqrt{m_{\tilde{t}_1}^2 + m_{\tilde{t}_2}^2}$.

All the other SM particles give much smaller radiative contributions to the Higgs potential and hence less stringent limits on the SUSY spectrum. The only exception is the gluino, which induces a large correction to the top squark masses at 1-loop and therefore feeds into the Higgs potential at two loops. This correction, neglecting the mixed $A_t M_3$ contributions, is given by

$$\delta m_{H_u}^2|_{\tilde{g}} = -\frac{2}{\pi^2} y_t^2 \left(\frac{\alpha_s}{\pi}\right) |M_3|^2 \log^2\left(\frac{\Lambda}{\text{TeV}}\right) \tag{2.21}$$

where M_3 is the gluino mass. This corrections can also be translated in a naturalness bound on the gluino mass

$$M_3 \leq 900\,\text{GeV}\sin\beta\left(\frac{\log(\Lambda/\text{TeV})}{3}\right)^{-1}\left(\frac{m_h}{125\,\text{GeV}}\right)\left(\frac{\Delta^{-1}}{20\%}\right)^{-1/2} \tag{2.22}$$

corresponding to an upper limit of about 1.5 TeV.

2.4 A Dark Matter candidate

One of the most compelling hints for physics beyond the Standard Model is the cosmological observation that about 25% of our universe consists of Dark (i.e., non-relativistic, non-luminous and non-absorbing) Matter. Weakly interacting massive particles (WIMPs), with masses roughly between 10 - 100 GeV and cross

sections of approximately weak strength are attractive DM candidates. The currently best motivated WIMP DM candidate is the lightest supersymmetric particle (LSP) in SUSY models with exact R-parity.

2.5 Unification of interactions

Grand unified theories (GUT) provide a framework for understanding the origin of the diverse strengths of the various forces observed in nature. The GUT assume to have a single force associated with a grand unified local symmetry at a high scale, which below the scale of the symmetry breaking evolves into three different strengths corresponding to the observed weak, electro-magnetic and strong interactions. The challenge is to have a theory where the three couplings evolved down to the m_Z scale match their experimentally observed values. Supersymmetric models provide a concrete realization of the unification of gauge couplings: the unification scale is $\Lambda_U \approx 2 \times 10^{16}$ GeV, when assuming the existence of SUSY particles with masses $\Lambda_{SUSY} \approx 1$ TeV. Such unification is a strong hint for grand unification at scales near Λ_P. The failure of coupling constant unification in the SM may indicate that there is no desert between m_Z and Λ_U, therefore new physics at some intermediate scale must exist.

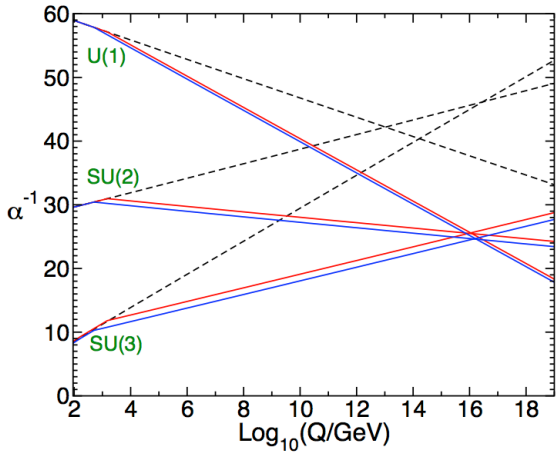

Figure 2.3: Two-loop renormalization group evolution of the inverse gauge couplings $\alpha_a^{-1}(Q)$ in the Standard Model (dashed lines) and its minimal supersymmetric extension (solid lines). [16]

2.6 Third generation topologies

Third generation squarks are expected to be lighter than the other squarks as discussed in Section 2.3.4, and therefore their production may be dominant at the LHC. If the top or the bottom squarks are relatively light, there are mainly two types of production processes. One is through the decay of gluinos and the other is via direct pair production. If the gluino is not much heavier than the top squark, the direct production of gluinos dominates over direct top (or bottom) squark production. However, it is possible that gluinos might be heavier than a few TeV. In this case, only direct top squark pair production would be observed.

Signal cross sections are calculated to next-to-leading order in the strong coupling constant, adding the resummation of soft gluon emission at next-to-leading-logarithmic accuracy (NLO+NLL) [28, 29, 30]. The nominal cross section and the uncertainty are taken from an envelope of cross section predictions using different PDF sets and factorisation and renormalisation scales, as described in Ref. [31].

Figure 2.4 shows the production cross section of top squark pairs at a center-of-mass energy of 8 TeV, computed with the above described technique. Top squarks with a mass of 150 GeV and 400 GeV (the benchmarks that will be used in Chapter 6) are expected to respectively have a cross-sections of 80 ± 13 pb and 0.35 ± 0.05 pb.

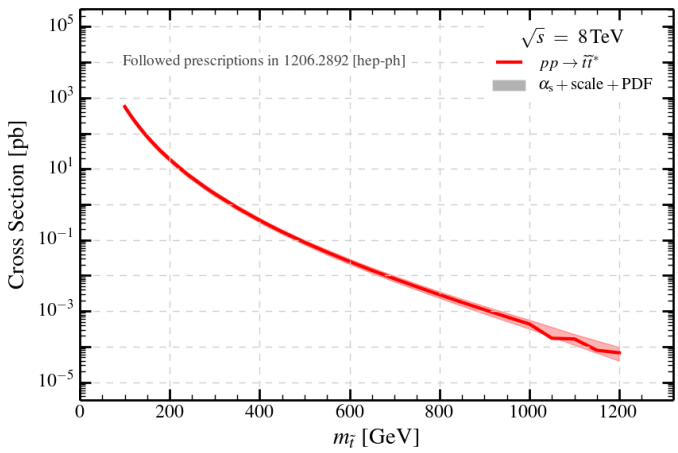

Figure 2.4: Cross-sections for the pair production of top squarks as a function of their masses calculated to NLO+NLL using PROSPINO for proton-proton collisions at $\sqrt{s} = 8$ TeV

2.6.1 Top squark decay modes

The decay modes of the top and bottom squarks depend on the SUSY particle mass spectrum. In the rest of this work, for simplicity, only the lightest top squark, the lightest chargino and the lightest neutralino are considered as the active SUSY particles; the other SUSY particles are assumed to be heavy enough (masses of the order of TeV) such that they decouple. The decay modes of the bottom squarks can be inferred by the analogy to the top squark.

The top squark decay modes are shown in figure 2.5 will be described in the following.

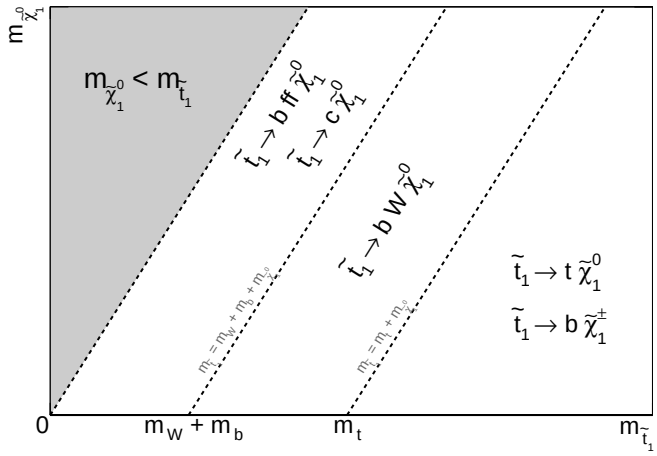

Figure 2.5: Main top squark decay modes as a function of the top squark and lightest neutralino masses.

Two-body decay

A.1 If $m_{\tilde{t}_1} > m_t + m_{\tilde{\chi}_1^0}$, the top squark can decay via

$$\tilde{t}_1 \to t + \tilde{\chi}_1^0 \tag{2.23}$$

If the lightest neutralino is the LSP, $\tilde{\chi}_1^0$ cannot decay anymore but the top quark will decay further. The final state therefore consists of multi-jets including b-jets, leptons and $E_{\mathrm{T}}^{\mathrm{miss}}$. Figure 2.6 (left) shows the Feynman diagram in the case of both final state top quarks decaying leptonically.

A.2 If $m_{\tilde{t}_1} > m_b + m_{\tilde{\chi}_1^+}$,the top squark can decay via

$$\tilde{t}_1 \to b + \tilde{\chi}_1^+ \tag{2.24}$$

Since the lightest chargino is in general heavier than the lightest neutralino, the lightest chargino can decay further trough either a scalar fermion or a W boson (where the intermediate particle can be either be real or virtual) via $\tilde{\chi}_1^+ \to \tilde{\chi}_1^0 + f + f'$, where f and f' are any SM fermions. The branching ratios to fermion flavors depend on the corresponding scalar fermion masses. Figure 2.6 (right) shows the Feynman diagram in the case of both final state W bosons decaying leptonically.

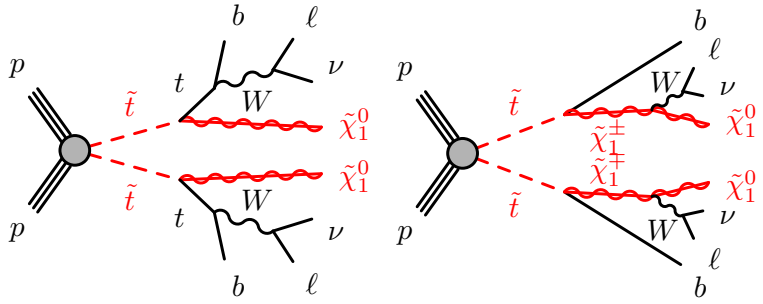

Figure 2.6: The figure on the left illustrates the Feynman diagram for the $\tilde{t}_1 \to t\tilde{\chi}_1^0$ decay. The figure on the right illustrates the Feynman diagram for the $\tilde{t}_1 \to b\tilde{\chi}_1^\pm$ decay. In both cases, a leptonic decay for each of the the final state W bosons has been assumed.

A.3 If the above two decay modes and the three-body decay modes shown below are all suppressed, the top squark can decay via

$$\tilde{t}_1 \to c + \tilde{\chi}_1^0 \tag{2.25}$$

if $m_{\tilde{t}_1} > m_c + m_{\tilde{\chi}_1^0}$ through the one-loop diagram such as shown in figure 2.7. However, this topology is only possible in a limited parameter space.

Three-body decay

The branching ratios for three-body decays are much smaller than those of two-body decays. If the two-body decay modes (A1 and A2) are forbidden, however, three-body decays can be dominant.

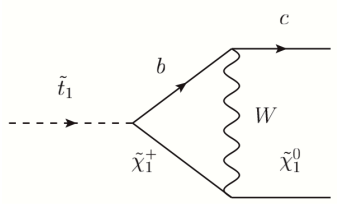

Figure 2.7: One of the $\tilde{t}_1 \to c + \tilde{\chi}_1^0$ decay diagram in one-loop

B.1 If the sleptons are lighter than the top squark, the latter can decay via

$$\tilde{t}_1 \to b + \nu + \tilde{l} \tag{2.26}$$

However, a charged LSP is forbidden from the cosmological constraints. Hence, none of the sleptons can be the LSP and therefore they will decay further. This results in the final states with b-jets, leptons and $E_{\mathrm{T}}^{\mathrm{miss}}$.

B.2 If the sneutrinos are lighter than the top squark, the latter can decay via

$$\tilde{t}_1 \to b + l + \tilde{\nu} \tag{2.27}$$

Regardless of whether one of the sneutrinos is the LSP or not, the sneutrino or other LSP are not detected. This decay mode therefore also results in the final stats with b-jets, leptons and $E_{\mathrm{T}}^{\mathrm{miss}}$.

B.3 If $m_b + m_W < m_{\tilde{t}_1} - m_{\tilde{\chi}_1^0}$, the top squark can decay via

$$\tilde{t}_1 \to b + W + \tilde{\chi}_1^0 \tag{2.28}$$

This decay became preferable with respect to the two-body decay A1 only if $m_{\tilde{t}_1} - m_{\tilde{\chi}_1^0} < m_t$. If the lightest neutralino is the LSP, $\tilde{\chi}_1^0$ cannot decay anymore but the W boson will decay further. The final state therefore consists of multi-jets including b-jets, leptons and $E_{\mathrm{T}}^{\mathrm{miss}}$. Figure 2.8 shows the Feynman diagram for this process, in the case of both final state W bosons decaying leptonically.

These decay processes are different from two-body decays but the final states are the same as one of the decay modes described in the previous paragraph. Therefore by searching for two-body decay modes, these three-body decay modes are also naturally covered.

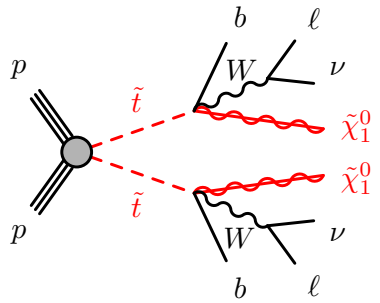

Figure 2.8: The figure illustrates the Feynman diagram for the case of the $\tilde{t}_1 \to bW\tilde{\chi}_1^0$ 3-body decay, considering both W bosons decaying leptonically.

Four-body decay

If all two-body decay modes (A1 and A2) and three-body decay modes (B1 and B2) are forbidden, the branching ratio of the top squark decay via four-body decay modes can be dominant.

C.1 In this case, the top squark can decay via

$$\tilde{t}_1 \to b + f + f' + \tilde{\chi}_1^0 \tag{2.29}$$

where f and f' are any SM fermions. Figures 2.9 show some examples of tree-level Feynman diagrams of this decay mode. Since this mode has the same order in perturbation theory as the loop-induced A3 decay ($\mathcal{O}(\alpha^3)$), its branching ratio is competitive to that of the A3 mode. For example, it can be enhanced if the charginos have masses not much larger than their present experimental bounds, or if the sfermions are light [32].

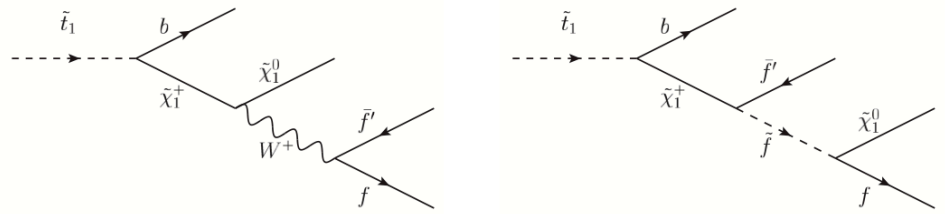

Figure 2.9: The tree-level Feynman diagrams for $\tilde{t}_1 \to b + f + f' + \tilde{\chi}_1^0$

Although this is a different decay process from the two-body decay, the final states have the same composition and also these modes are naturally covered by the two-body decay searches.

2.7 Benchmark models

In the context of the MSSM, each final state signature can be produced in multiple ways. When a signal is seen, it won't be immediately possible to determine what particles are producing it or what their decay modes are. For this reason, a new approach, referred to as "Simplified Models", has been developed by characterizing the basic properties of a decay chain in a manner that allows comparison to any model.

These are effective field theories for collider physics aimed at developing searches and exploring common features of new physics. Simplified models are effective models built including the minimal particle content necessary to produce SUSY-like final states contributing to the channels of interest and parametrized directly in terms of cross sections for production, branching ratios for decays, and masses of on-shell particles.

The kinematics, masses and phase space, of production and decay vertices are treated exactly, whereas the highly model-dependent dynamics appearing in quantum amplitudes are approximated using effective parameterizations of $|\mathcal{M}|^2$. Thus, these models rely on the fact that only a few dynamical variables control the phenomenology of new physics at hadron colliders.

Simplified Models with a simple spectra are a starting point for building more accurate models, since deviations from the phenomenology of the Simplified Models can indicate the need for a larger set of particles interacting in the theory. The production and decay modes are generally linked together in all possible ways to generate a list of consistent topologies, allowing the results of the search be reported in terms of limits on cross-section times branching ratios as a function of new particle masses, separately for each event topology.

The simplified model framework is meant to be used as a complementary approach to the usual interpretation in more complete models including the full MSSM particle spectrum. However the results presented in this thesis will be interpreted in the context of Simplified Models targeting specifically the top squark decay.

2.8 Top quark partners in other Beyond Standard Model theories

Supersymmetry is not the only theory trying to address the limitations of the SM.

A top-quark fermionic partner T which decays into a stable, neutral, weakly interacting particle A_0 also appears in other SM extensions, such as little Higgs models with T-parity conservation [33, 34, 35] or models of Universal Extra Dimensions (UED) with Kaluza-Klein parity [36]. In many of such cases, the T decays into a top quark and an A_0 , mimicking the decay of a top squark to a top quark and a neutralino. The main observable difference with respect to the supersymmetric case, is that the production cross section is larger by about a factor of six.

Little Higgs theories are an attempt to address the hierarchy problem up to the scale of $5 - 10$ TeV by adding weak-isospin singlets, doublets or triplets of vector-like quarks [37, 38]. In little Higgs theories, the Higgs mass is protected to the one-loop order from the quadratic divergence. This allows the renormalization cutoff to be raised up to about 10 TeV, beyond the scales probed by the precision data. A new symmetry, denoted as T-parity, under which all heavy gauge bosons and scalar triplets are odd, is needed to remove all the tree-level contributions to the electroweak observables and make the little Higgs theories natural. The T-odd particles need to be pair-produced and will cascade down to the lightest T-odd particle (LTP) which is stable. A neutral LTP gives rise to missing energy signals at the colliders which can mimic supersymmetry. It can also serve as a good dark matter candidate.

The Universal Extra Dimensions model is a scenario where all SM fields are allowed to propagate in the bulk of the extra dimensions. Therefore, every SM particle has heavy Kaluza-Klein partners. Since there are no tree level brane-localized fields or interactions in the UED scenario, the momentum along the extra dimensions is conserved. Furthermore, the higher dimensional couplings are dimensional and thus UED is an effective theory, valid up to a cutoff scale. To setup a particular UED model, one has to specify the number of extra dimensions as well as the compactification scale. The typical scale for the compatictification of extra dimensions in which SM fields live is around the TeV. The UED models were not motivated by a solution to the hierarchy problem, but were originally proposed as a a model for electroweak symmetry breaking.

One family of theories adds a fourth generation of heavy chiral fermions [39, 40] to the SM, in order to provide new sources of CP violation that could explain

the matter-antimatter asymmetry in the universe. The new weak-isospin doublet contains heavy up-type (T) and down-type (B) quarks that mix with the lighter quarks via an extended CKM matrix. In order to be consistent with precision electroweak data, a relatively small mass splitting between the new quarks is required [41].

CHAPTER 3

Data and Monte Carlo Simulation

This chapter summarizes the data samples which will be analyzed in Chapters 5 and 6 and the Monte Carlo (MC) simulation samples which have been used to model the contribution from SM and expected signal processes.

3.1 Data samples

The ATLAS detector recorded 5.25 fb^{-1} of proton-proton collisions at $\sqrt{s} = 7$ TeV in 2011. An additional 21.3 fb^{-1} of proton-proton collisions at $\sqrt{s} = 8$ TeV has been recorded in 2012. Figure 3.1 shows the cumulative luminosity versus day/month for the two data-takings.

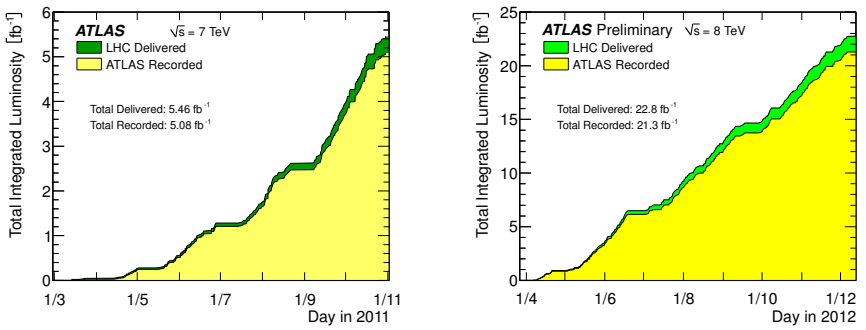

Figure 3.1: Cumulative luminosity versus time delivered to (green), and recorded by ATLAS (yellow) during stable beams and for pp collisions at 7 TeV (left) and 8 TeV (right) centre-of-mass energy data takings. [5]

The analysis presented in Chapter 5 uses all the proton-proton collisions data collected in 2011, to which beam, detector and data quality requirements are ap-

plied, yielding a total integrated luminosity of 4.7 ± 0.2 fb^{-1}. The analysis presented in Chapter 6 uses all the proton-proton collisions data collected in 2012, to which the same data quality requirements are applied, yielding a total integrated luminosity of 20.3 ± 0.6 fb^{-1}. The 2011 dataset is not used in this analysis since it would give a negligible sensitivity contribution because of the reduced signal cross sections.

3.2 Monte Carlo simulation with $\sqrt{s} = 7$ TeV

Monte Carlo simulated event samples are used to aid in the description of the background and to model the SUSY and spin-1/2 heavy top-quark partner signals. Only processes with two real isolated leptons in the final state have been considered, since processes with at least one fake or not isolated lepton, collectively referred to as "fake" leptons in the following, are estimated entirely from data as will be described in section 5.5.4.

Pile-up effects are included. Events in MC are reweighted, so that the simulated distribution of the average number μ of proton-proton collisions per bunch crossing matches that in the data.

The MC generator parameters have been tuned to ATLAS data [42, 43] and generated events have been processed through a detector simulation [44] based on GEANT4 [45].

3.2.1 Standard Model

Top-quark pair and Wt production are simulated with MC@NLO [46, 47], interfaced with HERWIG [48] for the fragmentation and the hadronization processes, including JIMMY [49] for the underlying event. The top-quark mass is fixed at 172.5 GeV, and the NLO PDF set CTEQ10 [50] is used. Additional MC samples are used to estimate the event generator systematic uncertainties: two POWHEG [51] samples, one interfaced with HERWIG and the other with PYTHIA [52]; an ALPGEN [53] sample interfaced with HERWIG and JIMMY; two ACERMC [54] samples produced with variations to the PYTHIA parton shower parameters chosen such that the two samples produce additional radiation consistent with the experimental uncertainty in the data [55, 56].

Samples of $Z/\gamma^\star$ produced in association with light- and heavy-flavour jets are generated with ALPGEN using the PDF set CTEQ6.1 [57]. Samples of $t\bar{t} + Z$

Table 3.1: The most important SM background processes and their production cross sections, multiplied by the relevant branching ratios. The ℓ indicates all three types of leptons (e, μ, τ) summed together. The $Z/\gamma^\star$ production cross section is given for events with a di-lepton invariant mass of at least 12 GeV.

Physics process	σ·BR [pb]	Perturbative order
$Z/\gamma^\star \to \ell^+\ell^-$	1069 ± 53	NNLO
$t\bar{t}$	167^{+17}_{-18}	NLO+NNLL
Wt	15.7 ± 1.2	NLO+NNLL
$t\bar{t} + W$	$0.168^{+0.023}_{-0.037}$	NLO
$t\bar{t} + Z$	0.130 ± 0.019	NLO
WW	44.4 ± 2.8	NLO
WZ	19.1 ± 1.3	NLO
ZZ	6.2 ± 0.3	NLO

and $t\bar{t} + W$ production are generated with MADGRAPH [58] interfaced to PYTHIA.

Diboson samples (WW, WZ, ZZ) are generated with SHERPA [59]. Additional samples generated with ALPGEN and HERWIG are used for the evaluation of the event generator systematic uncertainties.

The background predictions are normalized to theoretical cross sections, including higher-order QCD corrections when available, and are compared to data in control regions populated by events produced by SM processes. NNLO cross sections are used for inclusive Z boson production [60]. Approximate NLO+NNLL cross sections are used in the normalization of the $t\bar{t}$ [61] and Wt [62] samples. NLO cross sections are used for the diboson samples [46, 63] and for the $t\bar{t} + W$ and $t\bar{t} + Z$ [64] samples. Production of $t\bar{t}$ in association with $b\bar{b}$ is normalized to leading order (LO) cross section [53]. Table 3.1 summarizes the production cross sections used in this analysis and their uncertainties.

3.2.2 Signal

Top squark signal samples are generated with HERWIG++[65]. The mixings in the top squark and gaugino sector are chosen to be such that the lightest top squark is mostly the partner $\tilde{t}_R$ of the right-handed top quark, and the lightest neutralino is almost a pure bino. Under such conditions, the top squark is expected to decay to the lightest neutralino and a top quark with a branching ratio close to 100%,

even if the decay mode to a chargino and a b quark is kinematically allowed. The effects of helicity in the decay are correctly treated by HERWIG++.

In this framework only two parameters are relevant: the mass of the stop and the mass of the lightest neutralino, and signal grids are generated in this plane with stop masses up to 800 GeV and neutralino masses up to 550 GeV in steps of 25 GeV or 50 GeV.

Spin-1/2 heavy top-quark partner signal samples are generated with MADGRAPH [58]. A grid with the pair production of spin 1/2 top partner T was generated in the range from 300 GeV to 600 GeV, with A masses assuming values up to 400 GeV in steps of 50 GeV.

3.3 Monte Carlo simulation with $\sqrt{s} = 8$ TeV

3.3.1 Standard Model

Similarly to what has been done for the 7 TeV MC simulation, top-quark pair and Wt production have been simulated with MC@NLO interfaced with HERWIG for the fragmentation and the hadronization processes and including JIMMY for the underlying event. The $t\bar{t}$ cross section is computed for a top quark mass of 172.5 Gev. It has been calculated at NNLO+NNLL with top++2.0 [66, 67, 68, 69, 70, 71]. The PDF and α_S uncertainties were calculated using the PDF4LHC prescription [72] with the MSTW2008 68% CL NNLO [73, 74], CT10 NNLO [50, 75] and NNPDF2.3 5f FFN [76] PDF sets, added in quadrature to the scale uncertainty. The NNLO+NNLL value, as implemented in Hathor 1.5[61], is about 3% larger than the exact NNLO prediction. Additional MC samples are used to estimate the event generator systematic uncertainties: two POWHEG samples, one interfaced with HERWIG and the other with PYTHIA; two ACERMC tuned with the same technique used for the 7 TeV simulation.

Samples of $Z/\gamma^\star$ produced in association with light- and heavy-flavour jets are generated with SHERPA, while ALPGEN (using the PDF set CTEQ6.1) has been used to simulate samples for the evaluation of the event generator systematic uncertainties and the description of low mass Drell-Yan .

Samples of $t\bar{t} + Z$ and $t\bar{t} + W$ production are generated with MADGRAPH interfaced to PYTHIA.

Diboson samples (WW, WZ, ZZ) are generated with POWHEG. Additional samples generated with SHERPA are used for the evaluation of the event generator

Table 3.2: The most important SM background processes and their production cross sections, multiplied by the relevant branching ratios. The ℓ indicates all three types of leptons (e, μ, τ) summed together. The $Z/\gamma^\star$ production cross section is given for events with a di-lepton invariant mass of at least 12 GeV.

Physics process	σ·BR [pb]	Perturbative order
$Z/\gamma^\star \to \ell^+\ell^-$	1122 ± 53	NNLO
$t\bar{t}$	253^{+13}_{-15}	NNLO+NNLL
Wt	22.4 ± 1.5	NLO+NNLL
$t\bar{t} + W$	0.23 ± 0.07	NLO
$t\bar{t} + Z$	0.21 ± 0.06	NLO
WW	54.71 ± 2.8	NLO
WZ	33.31 ± 1.3	NLO
ZZ	8.73 ± 0.4	NLO

systematic uncertainties.

Table 3.2 summarizes the production cross sections used for the analysis described in Chapter 6 and their uncertainties.

3.3.2 Signal

For the $\tilde{t}_1 \to b + \tilde{\chi}_1^\pm$ decay the signal models were generated in a simplified model containing only the $\tilde{t}_1$, the $\tilde{\chi}_1^\pm$ and the $\tilde{\chi}_1^0$.

The signal grids are generated with MADGRAPH interfaced with PYTHIA for the showering simulation. The $\tilde{t}_1$ is required to decay to the targeted final state with 100% BR. The $\tilde{t}_1$ mass ranges from 150 GeV to 600 GeV with a granularity which is 25 GeV for the lowest masses and increases to 100 GeV for highest masses. Due to practical reasons it has not been possible to generate a complete 3-dimensional grid in the masses of the top squark, chargino and neutralino. Therefore projections of the 3D plane have been chosen, with granularities going from 25 GeV to 50 GeV in the variable mass parameters. In all cases the $\tilde{\chi}_1^\pm$ mass starts from 100 GeV, and degeneracies between sparticles are removed by lowering the mass of the decay particle by 10 GeV.

The following 2D signal scenarios have been generated and will be used for the interpretation of results:

- For a fixed mass difference $m(\tilde{t}_1) - m(\tilde{\chi}_1^{\pm}) = 10$ GeV, $\tilde{\chi}_1^0$ and $\tilde{t}_1$ masses are scanned.
- For a $m(\tilde{\chi}_1^0) = 1$ GeV, the $\tilde{\chi}_1^{\pm}$ and $\tilde{t}_1$ masses are scanned.
- For $m(\tilde{t}_1) = 300$ GeV, the $m(\tilde{\chi}_1^0) - m(\tilde{\chi}_1^{\pm})$ plane are scanned.
- For $m(\tilde{\chi}_1^0) = 0.5 \times m(\tilde{\chi}_1^{\pm})$ the $m(\tilde{\chi}_1^0) - m(\tilde{t}_1)$ plane are scanned.
- For $m(\tilde{\chi}_1^{\pm}) = 150$ GeV the $m(\tilde{\chi}_1^0) - m(\tilde{t}_1)$ plane are scanned.

Furthermore, a set of samples covering the $\tilde{t}_1$ 3-body decay has been generated with HERWIG++, with a grid of points with $m(W) < m(\tilde{t}_1) - m(\tilde{\chi}_1^0) < m(t)$ and $m(\tilde{\chi}_1^0)$ up to 200 GeV.

CHAPTER 4

Event reconstruction

Proton-proton interaction events are reconstructed using the information collected by the sub-detectors described in Chapter 1. The focus of this thesis will be on the search for direct production of top squarks in the two lepton channel and this chapter will describe how the involved physics objects are defined and reconstructed.

4.1 Tracks

Track reconstruction for charged particles with $p_T > 0.4$ GeV and $|\eta| < 2.5$ is performed in the ATLAS Inner Detector with the following steps [77].

- *Pre-processing*: the raw data from the pixel and SCT detectors are converted into clusters and the TRT raw timing information is translated into calibrated drift circles. The SCT clusters are transformed into space-points, using a combination of the cluster information from back-to-back of a SCT module.

- *Track-finding*: prompt tracks originating from the interaction region are found exploiting the high granularity of the silicon detectors, following an inside-out pattern recognition algorithm. First, track seeds are formed from a combination of space-points in the three pixel layers and the first SCT layer. These seeds are then extended through the SCT to form track candidates. These candidates are fitted, the clusters with bad quality of the fit are removed, ambiguities in the cluster-to-track association are resolved, and fake tracks are rejected. The selected tracks are then extended into the TRT and associated with drift-circle information to resolve the left-right ambiguities.

The extended tracks are refitted with the full information of all three detectors. The quality of the refitted tracks is compared to the silicon-only track candidates and hits on track extensions resulting in bad fits are labeled as outliers.

- *Post-processing*: A dedicated vertex finder is used to reconstruct primary vertex candidates, as documented in the next section. The parameters of the fitted tracks are re-evaluated once a vertex intersection constraint is added.

4.2 Primary vertex

The reconstruction of primary vertices can be logically divided into two parts. The primary vertex *finding* algorithm deals with solving the pattern recognition problem, i.e. association of tracks to vertex candidates by forming clusters of tracks. The vertex *fitting* algorithm determines the vertex position and the corresponding error matrix. The input to the fitting algorithm is a set of reconstructed tracks found within a cluster by the finding algorithm.

At the present stage, the input of the vertex reconstruction algorithms consists of tracks selected according to the following criteria:

- $p_{\mathrm{T}} > 400$ MeV,
- $|d_0| < 4$ mm,
- $\sigma(d_0) < 5$ mm,
- $\sigma(z_0) < 10$ mm,
- at least 4 hits in the SCT detector,
- at least 6 hits in the pixel and SCT detectors.

Here d_0 and z_0 denote the transverse and longitudinal impact parameters of tracks with respect to the centre of the luminous region, and $\sigma(d_0)$ and $\sigma(z_0)$ denote the corresponding uncertainties as estimated in the track fit. The selection criteria based on the impact parameters are designed to remove a good fraction of the tracks originating from secondary interactions.

The luminous region in ATLAS is determined during a physics run by applying an unbinned maximum likelihood fit to the distribution of primary vertices

recorded in this period of time, where the same primary vertex reconstruction algorithm is used as described in the following, but without applying the beam-spot constraint. A detailed description of how the beam-spot is determined and on the uncertainties connected with its determination can be found in Ref. [78].

The *Iterative Vertex Finding* and *Fitting* approaches are defined by the following steps:

- Reconstructed tracks compatible with originating from the interaction region are pre-selected according to the criteria listed above.
- A vertex seed is found by looking for the global maximum in the distribution of z coordinates of the tracks, computed at the point of closest approach to the beam-spot center.
- The vertex position is determined using the *adaptive vertex fitting* algorithm [79], which takes as input the seed position and the tracks around it. The adaptive vertex fitter is a robust χ^2 based fitting algorithm which deals with outlying track measurements by down-weighting their contribution to the overall vertex χ^2.
- Tracks incompatible with the vertex by more than approximately 7 σ are used to seed a new vertex. The compatibility of the track to the vertex is expressed in terms of a χ^2 with 2 degrees of freedom. This procedure is repeated until no unassociated tracks are left in the event or no additional vertex can be found.

The parameters of the beam-spot are used both during the finding to pre-select compatible tracks and during the fitting step to constrain the vertex fit.

4.3 Jets

Hadronic particles in ATLAS deposit their energies mainly in the calorimeter system. In an attempt to resolve particles coming from the hard scatter, these energy deposits may be grouped into objects called jets.

As described in section 1.5, the ATLAS calorimeters have a high granularity. A procedure which groups cells into clusters has been developed, in order to reduce the impact of the noise induced by the high input multiplicity. This procedure also helps in determining the source of the signal thanks to the signals from neighboring cells. A sketch of a cluster is shown in Figure 4.1. The cells are associated

following a geometrical closeness criteria in the 3D space, and the clusters extend to the different radial layers of the calorimeter system: these topological cell clusters (*topoclusters*) are an attempt to reconstruct three-dimensional energy deposits from the showers developing for each particle entering the calorimeter.

The clustering starts with seed cells with a signal-to-noise ratio $\Gamma = E_{\text{cell}}/\sigma_{cell}^{noise}$ above a certain threshold $|\Gamma| > 4$. Then topological clusters are built by iteratively adding neighboring cells with $|\Gamma| > 2$. Finally, a ring of guard cells, with signal significances above a basic threshold $|\Gamma| > 0$, is added to the cluster. After the initial clusters are formed, they are analyzed for local signal maxima by a splitting algorithm. If more than one maximum is found, the cluster is split. The cluster variables which are relevant for the jet definition are the direction with respect to the interaction point, and the sum of the energy in its cells. From these variable, a 0 mass four-vector is associated to each single cluster, and the list of these four-vectors is used as input to the jet definition which merges the clusters in jets.

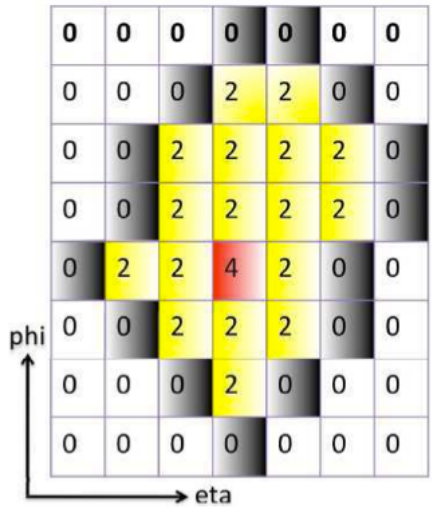

Figure 4.1: Topocluster schematic representation

The jet reconstruction algorithm adopted by the ATLAS collaboration as default is the anti-k_t [80]. The anti-k_t algorithm belongs to the sequential recombination class, where jets are built by pair-wise clustering of the initial constituents. These algorithms define also some condition upon which clustering should be terminated. For each measured object i with an associated four-momentum, the

quantities d_{ij} and d_{iB} are defined and evaluated as follows:

$$d_{ij} = min\left(p_{Ti}^{2p}, p_{Tj}^{2p}\right)\frac{\Delta R_{ij}^2}{R^2} \tag{4.1}$$

$$d_{iB} = p_{Ti}^{2p} \tag{4.2}$$

where $\Delta R_{ij}^2 = \left(y_i - y_j\right)^2 + \left(\phi_i - \phi_j\right)^2$, y_i is the rapidity of object i and p_{Ti} is the i object transverse momentum.

In the sense defined by the algorithm, the d_{ij} is the distance between two objects, and d_{iB} is the distance between the object and the beam. These distance definitions are common between different algorithms which differ from the value of the p parameter: for the anti-k_t algorithm, $p = -1$.

The variable R is a parameter that sets the resolution at which jets are resolved from each other with respect to the beam: this means that in the vicinity $\Delta R < R$ of a hard object, all softer objects will be merged with the harder object in order of their closeness in ΔR. If two comparably hard objects are within $R < \Delta R < 2R$ of each other, energy will be shared between them depending upon their relative p_T and distance. For hard objects within $\Delta R < R$ of each other, a single jet will be formed containing both hard objects and the soft objects within their vicinity. In the analyses presented in this thesis $R = 0.4$ was used.

The algorithm works in the following way: a list of all the distances d is compiled. If the smallest entry is a d_{ij}, objects i and j are combined and the list is remade. If the smallest entry is a d_{iB}, this object is considered a complete jet and is removed from the list. The distances are recalculated and the procedure repeated until no entities are left. The jet shape is unaffected from soft radiation, and the results are independent from the merging order.

Once the jet algorithm has performed the association of the inputs to the final jets, the recombination scheme defines how to determine the energy and momentum of the jets. Energy and momenta of the clusters are added into the four-momentum of the final jet. The result of the jet clustering is a list of jets at the so called electro-magnetic (EM) scale. This energy scale accounts correctly for the energy of electrons and photons, but it underestimates hadron energy, because the ATLAS calorimeters are not compensating. As a consequence, for equal incoming particle energy, electromagnetic showers generate larger signals than a corresponding hadronic energy deposit. A specific correction for the hadronic signals is hence needed.

4.3.1 Jet energy calibration

The ATLAS calorimeters are not compensating, so the energy of hadronic particles is underestimated. In order to compensate for the difference between the energy measurement of purely EM objects and the energy of a hadronic jet, an additional jet calibration must be applied to convert the EM scale of the ATLAS calorimeters to the hadronic scale. For this purpose, truth jets (or particle jets) are defined in MC simulations. They are built from stable particles produced by the fragmentation model in the physics generator. In ATLAS, stable particles are defined as those with the lifetime of 10 ps or more in the laboratory frame. Typically they include electrons, muons, photons, charged pions, charged and neutral kaons, protons, neutrons, neutrinos and their corresponding antiparticles. Neutrinos and muons are excluded from the truth-jet reconstruction, since they are almost invisible in the calorimeter. The same jet finding algorithm is applied for interacting stable particles to reconstruct truth jets.

ATLAS has developed several calibration schemes with different levels of complexity.

- *Simple p_{T} and η-dependent calibration scheme (EM+JES calibration)*: the goal of the Jet Energy Scale calibration, here called EM+JES because it is applied on top of the EM scale, is to correct the energy and momentum of jets measured in the calorimeter, using as reference the kinematics of the corresponding MC truth jets. The jet energy scale calibration is an average correction derived as a global function depending on p_{T} and η. Systematics are due to dead material and to uncertainties on calorimeters energy scale calculated from test beams, on simulation of the hadron showers in calorimeters and on Monte Carlo event generator description of fragmentation and underlying event.

- *Global cell energy density weighting calibration scheme (GCW calibration)*: the Global Cell Weighting Calibration depends only on the energy density in the calorimeter cells that belong to the reconstructed jet. Electromagnetic-like cascades generate more concentrated showers than hadronic-like cascades with the same energy. The energy density is therefore sensitive to the type of energy deposit. The GCW calibration method exploit this sensitivity to assign to each cell a correction weight based on its energy density. The

reconstructed jet energy is then defined as:

$$E_{\text{recoJets}} = \sum_{i=\text{cells}} w_i(\rho) \cdot E_i \tag{4.3}$$

The weights w_i are obtained minimizing the difference between E_{recoJets} and the reference jet energy.

- *Local Hadron Calibration (LCW calibration)*: the input for this calibration procedure are topological clusters. The clustering of the energy deposit in calorimeters allows to make a relatively good matching between clusters and stable particles in jets. Each cluster can be classified as mainly electromagnetic, hadronic or unknown, according to its shape (classification based on the predicted shape obtained in simulation). The effects of non-compensation, missing energy due to noise thresholds in the clustering, and energy deposits lost outside the calorimeters are dealt with in independent steps. Clusters classified as hadronic receive the appropriate calibration weight, to bring back the measured energy to the "true" energy deposit in calorimeter. Jets are then built from the calibrated clusters (while in the global calibration, jets were built from the uncalibrated clusters). There is still a difference between the calibrated energy and the reference jet energy due in particular to the fact that some particles composing the reference jet might be bent out of the acceptance of the reconstructed jet, or leave an energy which is too low to be included in a cluster. For this reason, a final jet-level correction on top of the local hadron calibration is used to correct for global effects.

4.3.2 *b*-tagging

The process of identifying jets originating from *b*-quark fragmentation (*b*-jets) is called *b*-tagging. Within the ATLAS collaboration several algorithms for the identification of b-jets, abbreviated as b-tagging algorithms, are available with different levels of complexity and performance. The first physics measurements published by the ATLAS Collaboration [81, 82, 83] used a set of basic algorithm termed as "early data taggers", which were commissioned shortly after the beginning of data taking [84]. More advanced taggers, with improved light-jet rejection capability have been implemented in physics analysis with the full 2011 data. This section describes those relevant for the work presented in this thesis.

All algorithms make use of the fact that b-quarks have a lifetime of about 10^{-12} s, significantly longer than the lighter quarks. Therefore, jets containing B-hadrons

can be identified by the direct presence of a secondary vertex in the event or tracks associated to jets that originate away from the primary vertex. The algorithms use different quantities, like the secondary vertex position or the impact parameter of tracks, and the performance of the algorithms can be further improved by using multivariate analysis techniques and combining several methods. The identification of b-jets profit from these specific properties to discriminate them from gluon- or light-quark initiated jets, and it is implemented through three spatial b-tagging algorithms: IP3D, SV1 and JetFitter.

The IP3D is a b-tagging algorithm based on two- and one-dimensional information of respectively the signed transverse impact parameter significance $d_0/\sigma(d_0)$ and of the longitudinal impact parameter significance $z_0/\sigma(z_0)$. The distributions of these variables are combined using a likelihood ratio technique comparing the input variables to pre-defined distributions for both the b- and light jet hypotheses.

The SV1 algorithm that takes into account the inclusive vertex information formed by the decay products of the b-hadron, including the products of the eventual subsequent charm hadron decay to further increase the discrimination between b-jets and light jets. Secondary vertices are fit and the discrimination between b-jets and light jets is done considering the decay length significance $L_{3D}/\sigma(L_{3D})$ measured in 3D (i.e., $L3D = ||\overrightarrow{X}_{PV} - \overrightarrow{X}_{track}||$) and signed with respect to the jet direction. To increase the discriminating power, additional variables are combined using a likelihood ratio technique.

The JetFitter algorithm exploits the topological structure of weak b- and c-hadron decays inside the jet. A Kalman filter is used to find a common line on which the primary vertex and the b- and c-vertices lie, as well as their position on this line, giving an approximated flight path for the b-hadron. With this approach, the b- and c-hadron vertices are not necessarily merged, even when only a single track is attached to each of them. The discrimination between b-, c- and light jets is based on a neutral network using similar variables as in the SV1 tagging algorithm above, and additional variables such as the flight length significances of the vertices.

The JetFitterCombNN algorithm, used in the analysis described in chapter 5, combines the outputs of these three algorithms using an artificial neural networks trained with Monte Carlo simulated samples.

In order for b-tagging to be used in physics analyses, the efficiency with which

a jet originating from a *b*-quark is tagged by a *b*-tagging algorithm needs to be measured, as well as the probability to tag a jet originating from a light-flavor quark, referred to as the mistag rate.

One way to measure the *b*-tagging efficiency is by using muon-jets. Though muons originate also from other processes, a major source is the semi-leptonic decay of the *b*- or *c*-quarks resulting from the *b*-quark decays. In the p_T^{rel} [84] measurement the momentum of a muon orthogonal to the flight axis of the jet it is associated to is used to measure the *b*-jet content of a given sample. Templates of p_T^{rel} for *b*- , *c*- and light-flavor jets are fit to the data before and after *b*-tagging and the efficiency is calculated as $\epsilon = N_{b,tag} / N_b$.

A similar measurement uses uncorrelated taggers to numerically calculate the *b*-tagging efficiency from a set of 8 equations (System8 [85]). System8 is designed to minimize the dependence on simulation and it is a very promising method that will be used in future *b*-tagging calibration results.

The *b*-tagging efficiency of JetFitterCombNN has been measured in data: the results are in good agreement with simulated events as shown in figure 4.2. This figure shows, as a function of the jet p_T, the scale factors needed to match the MC b-tagging efficiency to what is observed in data, together with the associated uncertainties. All the scale factors are compatible with unity, with uncertainties up to 20%.

The measurement of the mistag rate, i.e. the probability of mistakenly tagging a jet originating from a light-flavour (u-, d-, s-quark or gluon) jet as a b-jet, is performed on an inclusive jet sample with two methods. The first method uses the invariant mass spectrum of tracks associated with reconstructed secondary vertices to separate light- and heavy-flavour jets, while the second is based on the rate at which secondary vertices with negative decay length significances, or tracks with negative impact parameter significances, are present in the data.

Advanced taggers like JetFitterCombNN greatly improve light-jet rejection at a fixed *b*-tagging efficiency with respect to more basic tagging algorithms, as is clearly visible in figure 4.3. At fixed *b*-jet efficiency, the light jet rejection can be increased by a factor of 2 to 5 with new taggers allowing better background rejection. On the other hand for same light-jet rejection, the working point can be chosen at higher efficiency. This is very promising for searches with low production cross section.

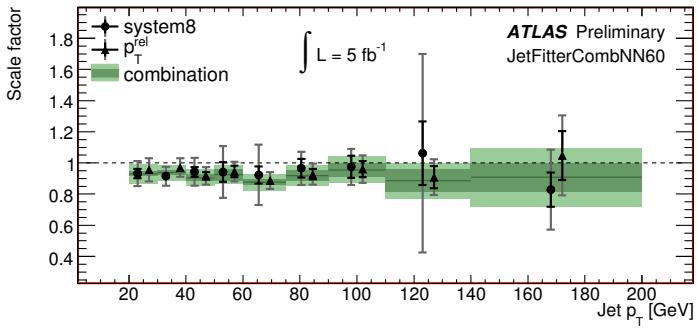

Figure 4.2: The individual and combined data-to-simulation scale factors for the JetFitterCombNN tagging algorithm at 60% efficiency. The dark green band represents the statistical uncertainty of the combined scale factor while the light green band shows the total uncertainty. The data points showing the p_T^{rel} and system8 measurements have been separated a little along the x-axis to make the plot more readable. [86]

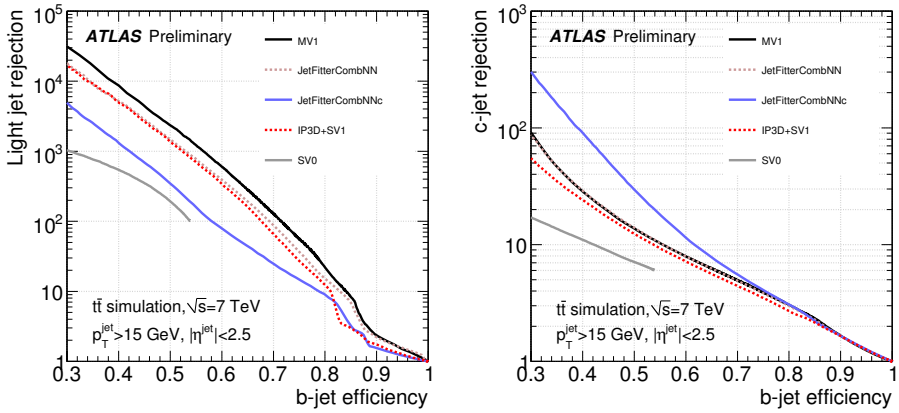

(a) (b)

Figure 4.3: (a) Light-jet rejection as a function of the b-tag efficiency for the b-tagging algorithms calibrated in this note, based on simulated $t\bar{t}$ events.
(b) c-jet rejection as a function of the b-tag efficiency for the b-tagging algorithms calibrated in this note, based on simulated $t\bar{t}$ events. [86]

4.4 Electrons

The standard electron reconstruction and identification procedure has been designed to achieve both large background rejection and high and uniform efficiency for isolated electrons over the full acceptance of the detector. It combines signals from the silicon detectors, the transition radiation tracker and the longitudinally layered EM calorimeter system. The strategy implemented is based on a sliding window algorithm [87] in which a fixed cone in $\eta \times \phi$ (3×5) is moved over the calorimeter cells to form seed clusters with a minimum energy of 2.5 GeV. The position which yields the maximum energy deposition within the cone is chosen as the cluster position.

Reconstructed tracks are matched to seed clusters by extrapolating them from their last measured point to the calorimeter's second layer. The track impact point is then compared to the coordinates of the corresponding seed cluster: if their difference is below a certain distance threshold then the track is considered matched to the cluster. In the case of tracks that do not contain silicon hits, the matching is restricted to the ϕ coordinate, due to the fact that the TRT accuracy on the η coordinate is limited. If more than one track points to the same cluster, priority is given to tracks with silicon hits and the smallest ΔR(track, cluster).

The cluster energy is determined by computing and summing four different contributions: the energy deposited in the calorimeter inside the cluster, the one deposited in the material in front of the EM calorimeter, the one deposited outside the cluster (lateral leakage) and finally the energy deposited beyond the EM calorimeter (longitudinal leakage). The corrections applied to the measured cluster energy are based on precise Monte Carlo simulations validated by comprehensive measurements with 900 GeV data [88].

The four terms are parametrized as a function of the cluster measured signals in the pre-sampler (where present) and in the three accordion longitudinal layers. The parameters are computed at each pseudorapidity value corresponding to the centre of a middle cell and stored in a database [89]. The energy is computed as a weighted average between the cluster energy and the track momentum. The η and ϕ directions are taken from the corresponding track parameters at the vertex, unless the track contains no silicon hits, in which case they are provided by the cluster.

The baseline ATLAS electron identification algorithm relies on variables which deliver good separation between isolated electrons and fake signatures from hadronic

jets. These variables include information from the calorimeter, the tracker and the matching between tracker and calorimeter. Three reference set of cuts have been defined for electrons:

- *Loose*: this set of cuts performs a simple electron identification based only on limited information from the calorimeters. Cuts are applied on the hadronic leakage and on shower-shape variables, derived from the middle layer of the EM calorimeter only. This set of cuts provides excellent identification efficiency, but poor background rejection.

- *Medium*: this set of cuts improves the background rejection quality, by adding cuts on the energy deposits in strips in the first layer of the EM calorimeter and on the tracking variables. Strip-based cuts are adequate for e - π^0 separation. The tracking variables include the number of hits in the pixels, the number of silicon hits (pixels plus SCT) and the transverse impact parameter. The medium cuts increase the fake rejection by a factor of 6 with respect to the loose cuts, while reducing the identification efficiency by $\sim 4\%$.

- *Tight*: in addition to the criteria used in the medium identification, cuts are applied on the number of hits in the first pixel layer (to reject electrons from conversions), on the number of hits in the TRT, on the ratio of high-threshold hits to the number of hits in the TRT (to reject the dominant background from charged hadrons), on the difference between the cluster and the extrapolated track positions in η and ϕ, and finally on the ratio of the cluster energy to the track momentum ratio. The fake rejection is $\sim 10^5$, while the identification efficiency is $\sim 70\%$.

4.4.1 Electron performance

The electron performance has been extensively studied by combining measurements of $Z \to e^+e^-$, $W \to e\nu$ and $J/\psi \to e^+e^-$ (for low p_T electrons) processes. The well known masses of the Z, W and J/ψ particles can be used to improve considerably the knowledge of the electron energy scale and its uncertainty. Figures 4.4 shows the J/Ψ and the Z invariant masses compared with the Monte Carlo simulation prediction: the agreement is found to be good.

These measurements have been used to correct for the differences of energy scale and resolution between data and MC simulation, energy resolution of electrons in MC samples are smeared and the energy scale of electrons in data is

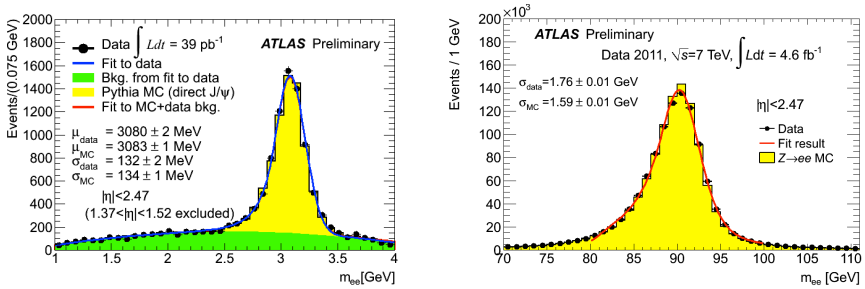

(a) (b)

Figure 4.4: Invariant mass of J/Ψ meson (left) [90], measured with an integrated luminosity of 39 pb^{-1}; Invariant Z mass for electron pairs (right) with an integrated luminosity of 4.6 fb^{-1}[90]

rescaled according to the measurements described in [91]. The energy-scale correction factor is defined by

$$\alpha \equiv \frac{E_{measured} - E_{true}}{E_{true}} \tag{4.4}$$

where $E_{measured}$ is the energy measured by the calorimeter after the MC-based energy-scale correction and E_{true} is the true electron energy. Moreover, scale factors that take into account the discrepancies between data and MC simulation in the electron reconstruction and identification efficiencies are applied to MC events.

4.5 Muons

The key part in the identification and reconstruction of muons is the muon system of the ATLAS detector, but a muon also leaves traces in the inner detector and the calorimeter. Hence, information from all detector parts can be used to reconstruct the track of a muon in the detector and to precisely determine its transverse momentum. ATLAS has developed four different muon reconstruction algorithms, depending on how the detector information is used.

- *Stand-alone*: the hits from MS are combined into segments to form a track. The direction of flight and the impact parameter of the muon at the interaction point are determined by extrapolating the spectrometer track back to

the beam line taking the energy loss of the muon in the calorimeters into account.

- *Combined*: track reconstruction is performed independently in the ID and MS, and a track is formed from the successful combination of a pair of these. A χ^2 matching procedure is implemented through the difference between a MS and ID track vector of five parameters expressed at the point of closest approach to the beam-line, weighted by their covariance matrix. The measure of the quality of this match is used to decide which pairs are retained. The muon parameters are derived from a combined track fit to the hits in the two sub-detectors.

- *Segment tagged*: an ID track with sufficient momentum is used as a seed and propagated to the first station of the MS. The reconstruction algorithms then searchs for track segments in the precision muon chambers that can be associated to the extrapolated Inner Detector track.

- *Calorimeter tagged*: an ID track is used as seed. The track is identified as a muon if energy depositions compatible with the minimum ionizing particle hypothesis can be associated to it.

ATLAS uses two different chains to evaluate the muon performance: *STACO* [92] and *MuId* [93]. These chains correspond to different sets of algorithms that build the classes of candidates listed above. Both muon combination algorithms create combined tracks out of pairs of Muon-only and Inner-Detector-only tracks, however the two algorithms handle the combined track in a slightly different way. STACO does a statistical combination of the track vectors to obtain the combined track vector, while MuId refits the combined track, starting from the Inner Detector track and then adding Muon Spectrometer measures. For the analyses presented in this thesis, the STACO algorithm has been used for reconstructing muons.

Following a similar approach to that of electrons, the muon identification implements three reference sets of cuts (*loose*, *medium* and *tight*) which are tuned to efficiently suppress fake tracks, muons created from high hit multiplicities in the muon spectrometer in punch-through events and discriminate against background muons from leptonic decay of heavy-flavor hadrons. Essentially, these refine the p_{T} thresholds, enhance the number of hits requirements and impose

conditions on their layer location, tune the transverse and longitudinal impact parameter with respect to the primary vertex to reject possible overlapping cosmic rays, among others.

4.5.1 Muon performance

The muon reconstruction performance was studied first of all in minimum bias events, by comparing basic reconstruction quantities with the Monte Carlo simulation [94]. Later, reconstruction and identification efficiencies have been measured from the experimental data using a tag-and-probe method with the di-muon decay of the Z boson ($Z \rightarrow \mu^+\mu^-$). These measurements allow to derive scale factor corrections as a function of the muon momentum and pseudorapidity, in order to correct for discrepancies when comparing data and Monte Carlo simulation.

Detector efficiencies, hit multiplicities, muon isolation, and residual distributions of reconstructed muon tracks were measured and found to be well reproduced by the Monte Carlo simulation. The capability of the ATLAS detector to reconstruct muons on a wide p_T range is illustrated in figure 4.5, where the di-muon spectrum is shown. Resonances down to J/Ψ and up to Z are evident.

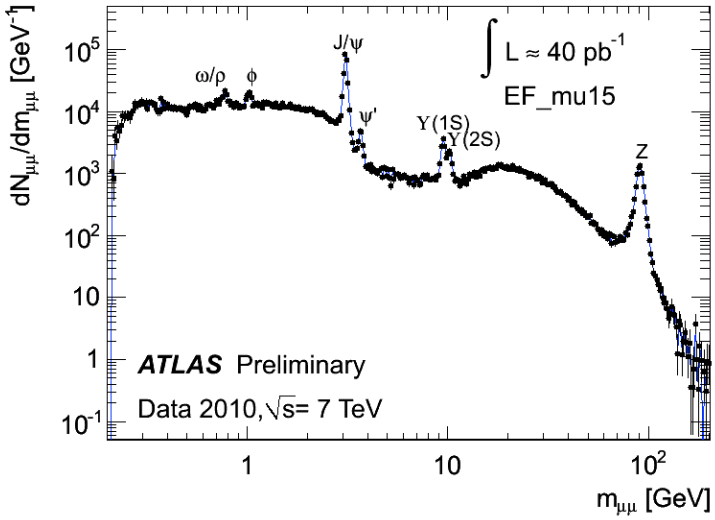

Figure 4.5: Di-muon invariant mass spectrum for data, from combined opposite sign muons. Peaks corresponding to various resonances are evident [95]

4.6 Missing Transverse Energy

In proton-proton collision the interacting parton momentum is unknown, and so is impossible to use the momentum conservation along the z axis. Instead the momentum conservation law can be used in the transverse plane where the total momentum is zero summing over all particles involved in the event, including non interacting particles like neutrinos.

The missing transverse energy ($E_{\mathrm{T}}^{\mathrm{miss}}$) is defined as:

$$E_{\mathrm{T}}^{\mathrm{miss}} = \sqrt{\left(E_x^{\mathrm{miss}}\right)^2 + \left(E_y^{\mathrm{miss}}\right)^2} \tag{4.5}$$

where $E_x^{\mathrm{miss}} = -\sum E_x$ and $E_y^{\mathrm{miss}} = -\sum E_y$ and $E_{x,y}$ are the energies measured in the detector. A correction to take into account dead or inactive detector components is also necessary.

The $E_{\mathrm{T}}^{\mathrm{miss}}$ reconstruction includes contributions from energy deposits in the calorimeters and muons reconstructed in the muon spectrometer. ID-reconstructed muons are used to recover losses due to the MS acceptance. The $E_{\mathrm{T}}^{\mathrm{miss}}$ reconstruction uses calorimeter cells calibrated according to the reconstructed physics object to which they are associated. Calorimeter cells are associated with a reconstructed and identified high-p_T parent object in a chosen order: electrons, photons, hadronically decaying τ-leptons, jets and muons. Cells not associated with any such objects are also taken into account in the $E_{\mathrm{T}}^{\mathrm{miss}}$ calculation.

Once the cells in calorimeters are associated with objects as described above, the $E_{\mathrm{T}}^{\mathrm{miss}}$ is calculated as follows:

$$\begin{aligned} E_{x(y)}^{\mathrm{miss}} &= E_{x(y)}^{\mathrm{miss},e} + E_{x(y)}^{\mathrm{miss},\gamma} + E_{x(y)}^{\mathrm{miss},\tau} + E_{x(y)}^{\mathrm{miss,jets}} \\ &+ E_{x(y)}^{\mathrm{miss,softjets}} + (E_{x(y)}^{\mathrm{miss,calo},\mu}) + E_{x(y)}^{\mathrm{miss,CellOut}} + E_{x(y)}^{\mathrm{miss},\mu} \end{aligned} \tag{4.6}$$

where each term is calculated from the negative sum of calibrated cell energies inside the corresponding objects (within $|\eta| < 4.9$), and the $E_{x(y)}^{\mathrm{miss},\mu}$ is calculated from the negative sum of the momenta of muon tracks reconstructed with $|\eta| < 2.7$. The $E_{\mathrm{T}}^{\mathrm{miss}}$ computation used in the analyses presented in this thesis does not compute the separate term for τ leptons, which are instead calibrated as jets. This is a conservative approach, motivated by the lack of explicit τ selections in the final state. Noise contributions due to the high granularity of the calorimeters are suppressed by the use of three-dimensional topological clusters, previously described in section 4.3. These clusters also ensure that the cells used in the $E_{\mathrm{T}}^{\mathrm{miss}}$

sum are the ones containing a significant signal. Electrons and photons are the only exception, using a different clustering algorithm.

The calibration scheme used is the one yielding the best performance in 2010 data. Electrons are calibrated with the default electron calibration (see section 4.4), photons are used at the EM scale, that provides the correct scale for energy deposited by electromagnetic showers, and the τ-jets are calibrated with the local hadronic calibration (LCW) [96]. The jets are reconstructed with the anti-k_t algorithm, with distance parameter $R = 0.4$. They are calibrated with the LCW scheme if their p_T is smaller than 20 GeV (soft jets) and with the LCW+EMJES scheme if their p_T is greater than 20 GeV. The contribution from topoclusters not associated to high-p_T objects is calculated with LCW calibration combined with tracking information.

The values of $E_{\mathrm{T}}^{\mathrm{miss}}$ and its azimuthal coordinate (ϕ^{miss}) are then calculated as:

$$\begin{aligned} E_{\mathrm{T}}^{\mathrm{miss}} &= \sqrt{\left(E_x^{\mathrm{miss}}\right)^2 + \left(E_y^{\mathrm{miss}}\right)^2} \\ \phi^{\mathrm{miss}} &= \arctan(E_y^{\mathrm{miss}}, E_x^{\mathrm{miss}}) \end{aligned} \tag{4.7}$$

The total transverse energy in the calorimeters, $\sum E_{\mathrm{T}}$, which is an important quantity to parameterize and understand the $E_{\mathrm{T}}^{\mathrm{miss}}$ performance, is defined as:

$$\sum E_{\mathrm{T}} = \sum_{i=1}^{N_{\mathrm{cell}}} E_i \sin\theta_i \tag{4.8}$$

where E_i and θ_i are the energy and the polar angle, respectively, of calorimeter cells associated to topoclusters within $|\eta| < 4.9$. Cell energies are calibrated according to the scheme described above for $E_{\mathrm{T}}^{\mathrm{miss}}$.

CHAPTER 5

Search for top squarks decaying to a neutralino and a top quark

ln the following chapter a search top squarks decaying in the $t + \tilde{\chi}_1^0$ final state will be presented. This analysis uses all the pp data collected by ATLAS during the 2011 run at $\sqrt{s} = 7$ TeV, as described in Section 3.1, and has been published in [2].

5.1 Introduction

Generic searches for supersymmetric (SUSY) particles address generic production of squarks and gluinos looking for events with large missing transverse momentum E_{T}^{miss} and jets plus possibly one or more leptons. Typical selection criteria require hard cut on E_{T}^{miss} and on the transverse momenta of the jets to reduce Standard Model (SM) backgrounds. However, such criteria have typically rather low efficiencies for sparticles lighter than 400 GeV [97].

This analysis seeks evidence for pair production of a heavy partner of the top quark, where each of the top partners decays into a b-jet, a lepton, and weakly interacting particles which escape detection. Two main criteria are used to separate the signal from the background: the request of b-tagged jets, which strongly suppresses the background from W/Z, and a selection which exploits the differences between the kinematics of top decays and of the new particles.

The analysis has been developed to target a top squark pair production where both top squarks decay as shown in Eq. 2.23 or the decay of a spin 1/2 top partner T. The final state contains two b-jets, two W bosons, real or virtual, and two invisible particles, which is the same final state as for the production and decays of pairs of top quarks, which thus constitute an irreducible background. In the

present study the signature with two leptons (e or μ) in the final state, produced in the decay of the two W bosons, is considered. This requests implies a high reduction in statistics, as the total BR is 4.9%, but it provides a strong suppression of reducible backgrounds, and, by using the kinematic of the two leptons, a good rejection against top background can be achieved. This selection is done using the *stransverse mass* variable, which is introduced in the next section.

5.1.1 The stransverse mass

The main discriminant variable used in the analysis is the so called *stransverse mass* (m_{T2}) calculated from the two leptons momenta and E_T^{miss}. This variable [98, 99] was introduced in the framework of SUSY measurement studies. It addresses the case where two identical particles ("legs") are produced, and both decay into an invisible particle. The vector sum of the transverse momenta of the two invisible particles is measured, and constitutes the E_T^{miss} of the event. The topology is illustrated in figure 5.1, from [98]. The idea is to consider all possible decompositions of the E_T^{miss} into two transverse vectors which are interpreted as the transverse momenta of the invisible particles in the two legs of the event. For each test value of the invisible momenta two transverse masses are built with the visible particles in the events and the maximum of the two values is taken. It is intuitive that the minimum value over all possible decompositions of E_T^{miss} of the variable thus calculated will be lower than the endpoint for the decay on a single leg. As an example, for WW production, m_{T2} will be below the endpoint for the W decay, which corresponds to the W mass.

The m_{T2} variable is defined as a function of the test mass for the invisible particles in the event. If this test mass is put to zero, the definition for m_{T2} reduces to:

$$m_{T2}^2(\vec{p}_T^{\,\alpha}, \vec{p}_T^{\,\beta}, \vec{p}_T^{\,\text{miss}}) = \min_{\vec{q}_T^{\,1}+\vec{q}_T^{\,2}=\vec{p}_T^{\,\text{miss}}} \left\{ \max \left[m_T^2(\vec{p}_T^{\,\alpha}, \vec{q}_T^{\,1}), m_T^2(\vec{p}_T^{\,\beta}, \vec{q}_T^{\,2}) \right] \right\} \tag{5.1}$$

where m_T indicates the transverse mass, $\vec{p}_T^{\,\alpha}$ and $\vec{p}_T^{\,\beta}$ are the momenta of the two leptons, and $\vec{q}_T^{\,1}$ and $\vec{q}_T^{\,2}$ are vectors which satisfy $\vec{q}_T^{\,1} + \vec{q}_T^{\,2} = \vec{p}_T^{\,\text{miss}}$. The minimum is taken over all the possible choices of $\vec{q}_T^{\,1}$ and $\vec{q}_T^{\,2}$.

For fully leptonic $t\bar{t}$, Wt, and WW events the value of m_{T2} has an upper bound equal to the W-boson mass. The bound $m_{T2} < m_W$ for SM events is quite sharp, and by selecting events with $m_{T2} > m_W$ it is thus possible to dramatically enhance the signal over background ratio. The distribution for both the expected

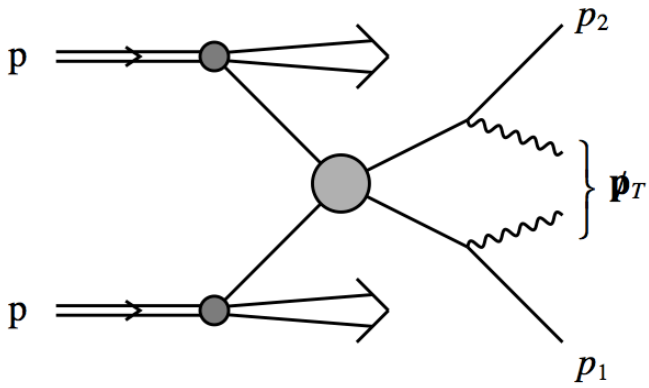

Figure 5.1: Diagram of the generic process under consideration. A hadronic collision that leads to a pair of particles being produced, which each decay into one particle that is observed with momenta p_1 and p_2 respectively; and one particle (shown as a wavy lines) that is not directly detected, and whose presence can only be inferred from the missing transverse momentum, p_T^{miss}

backgrounds and two benchmark signal processes can be found in figure 5.2 for events with two leptons, and in figure 5.18 after all selections except that on m_{T2} itself.

5.2 Trigger selection and object definition

Events are selected using single lepton triggers: they are required to pass either a single-electron trigger reaching a plateau efficiency of about 97% for electrons with $p_{\mathrm{T}} > 25$ GeV, or a single-muon or combined muon+jet trigger which reaches a plateau efficiency of about 75% (90%) in the barrel (end-caps) for events including muons with $p_{\mathrm{T}} > 20$ GeV and jets with $p_{\mathrm{T}} > 50$ GeV. The combined muon+jet trigger is used for the data-taking periods with high instantaneous luminosity, because it is based on looser muon identification requirements than the single-muon trigger available for those periods, resulting in a higher plateau efficiency.

Electron events in simulated samples are weighted to match the trigger efficiency in data by means of scale factors, defined as the ratio of the measured efficiency from data and from MC. A different approach is used for muons [100]: instead of relying on the trigger simulation and correcting it via scale factors, events are reweighted by using the efficiencies extracted from data, binned in relevant variables (e.g. p_{T}, η and ϕ), and requiring that at least one of the muons has issued the trigger in data. In this approach it is also straightforward to calculate event weights for an arbitrary collection and combination of triggers. In fact, assuming that n leptons are required in the final state, the probability that a single lepton trigger was issued by this event is given by the logical OR that one or more leptons in the event have passed the hypothesis of the trigger in question.

- *Jets* are reconstructed as described in 4.3 and calibrated at the EM+JES scale. Jets are kept only if they have $p_{\mathrm{T}} > 20$ GeV and lie within $|\eta| < 2.5$. An additional cut on the Jet Vertex Fraction[1] (JVF) is required to suppress pile-up jets, asking for $JVF > 0.75$.

- *Electron* candidates are required to have $p_{\mathrm{T}} > 20$ GeV, $|\eta| < 2.47$ and to satisfy "medium" electromagnetic shower shape and track selection quality criteria described in section 4.4. These preselected electrons are then required to pass "tight" quality criteria which places additional requirements on the ratio of calorimetric energy to track momentum, and on the fraction of hits in the straw tube tracker that pass a higher threshold for tran-

[1] By combining tracks and their primary vertices with calorimeter jets the Jet Vertex Fraction (or JVF) discriminant is defined, which is a measure of the probability that a jet originated from a particular vertex. Jet selection based on this discriminant is shown to be insensitive to the contributions from uncorrelated soft collisions due to pile-up.

sition radiation. The electron candidates are then required to be isolated: the scalar sum of the p_T, $\sum p_T$, of inner detector tracks, not including the electron track, with $p_{\mathrm{T}} > 1$ GeV within a cone in the $\eta - \phi$ plane of radius $\Delta R = \sqrt{\Delta\eta^2 + \Delta\phi^2} = 0.2$ around the electron candidate must be less than 10% of the electron p_{T}. In MC a multiplicative event weight is applied for each selected electron to the overall event weight in order to correct for differences in efficiency between data and MC.

- *Muon* candidates are reconstructed using either a full muon spectrometer track matched to an inner detector track, or a muon spectrometer segment matched to an extrapolated inner detector track. They must be reconstructed with more than one hit in the pixels, more than five hits in both the strips and straw tube detectors. They are required to have $p_{\mathrm{T}} > 10$ GeV, $|\eta| < 2.4$ and must have longitudinal and transverse impact parameters within 1 mm and 0.2 mm of the primary vertex, respectively.

  Muon candidates have been also required to be isolated. The $\sum p_{\mathrm{T}}$ of the tracks in a cone of $\Delta R < 0.2$ must be less than 1.8 GeV (excluding the muon track).

- The *missing transverse energy* calculation adds together jets calibrated at the EM+JES scale with $p_{\mathrm{T}} > 20$ GeV, "medium" electrons with $p_{\mathrm{T}} > 10$ GeV, all the muons from the STACO container (see section 4.5), and topological clusters in the calorimeters not belonging to pre-cited objects (*CellOut* term) calibrated at the EM scale.

- A *b*-tagging algorithm (JetFitterCombNN) exploiting both impact parameter and secondary vertex information, described in Section 4.3.2, is used to identify jets containing a *b*-hadron decay. The chosen operating point has a 60% efficiency for tagging *b*-jets in a MC sample of $t\bar{t}$ events, with a mis-tag probability of less than 1% for jets from light quarks and gluons.

Following the object reconstruction described above, overlaps between jet, electron and muon candidates are resolved. Any jet within $\Delta R = 0.2$ of preselected electrons is discarded. Electrons or muons within $\Delta R = 0.4$ of any remaining jet are then discarded to reject leptons from the decay of a *b*- or *c*-hadron.

5.3 Event selection

The primary vertex of each event, identified by the highest squared sum of the p_{T} of the associated tracks, is required to contain at least 5 tracks and be consistent with the transverse beam spot position: this cut reduces the chance of selecting a cosmic-ray event since the d_0 and z_0 of the muons considered in the analysis are calculated with respect to this primary vertex. In case of a cosmic muon, the event is rejected.

Events which contain exactly two opposite-sign (OS) leptons (electrons or muons) are selected if at least one lepton satisfies the leading p_{T} requirement of $p_{\mathrm{T}} > 25$ GeV for electrons and $p_{\mathrm{T}} > 20$ GeV for muons in order to be in the trigger efficiency plateau. If the event contains a third preselected electron or muon, the event is rejected. At least two jets with $p_{\mathrm{T}} > 25$ GeV, and at least one of them with $p_{\mathrm{T}} > 50$ GeV, are required. This requirement suppresses WW and $Z/\gamma^{\star}$+jets backgrounds.

The dilepton invariant mass m_{ll} is required to be larger than 20 GeV because of the lack of MC simulated samples for very low-mass ($m < 12$ GeV at truth level) Drell-Yan.

Two signal regions are defined, one for different-flavour, and one for same-flavour leptons. For the same-flavour SR, additional selections are imposed to suppress the $Z/\gamma^{\star}$+jets, WZ and ZZ backgrounds, which represent a significant fraction of events with large $\mathrm{m_{T2}}$. These events have large E_{T}^{miss}, which for the WZ process is generated by the leptonic decay of the W boson, for the ZZ process by the decay of one of the Z bosons to neutrinos, and for $Z/\gamma^{\star}$+jets by the tails in the jet energy resolution. The additional selections required in the same-flavour channel to suppress these backgrounds are that the invariant mass of the leptons must be outside the $71 - 111$ GeV range, and at least one of the jets must be tagged as a b-jet. After these selections the background is dominated by $t\bar{t}$.

Finally, for both SRs, signal candidate events are required to have a value of $\mathrm{m_{T2}}$ larger than 120 GeV. This requirement suppresses the remaining $t\bar{t}$ and WW backgrounds by several orders of magnitude and was chosen to optimize the coverage of the analysis in the $\tilde{t}_1 - \tilde{\chi}_1^0$ and $T - A_0$ planes.

The efficiency of the m_{T2} selection for $t\bar{t}$ events, calculated after all the other SR cuts, is 0.007%. The efficiency of the $\mathrm{m_{T2}}$ selection for stop and spin-1/2 heavy top-quark partner signal samples is given in table 5.1 for several values of the top-quark partner mass and for a massless $\tilde{\chi}_1^0$ or A_0. The kinematics of the signal

Table 5.1: Efficiency of the m_{T2} selection, calculated after all other selection requirements applied in the SR, for signal samples with different values of the mass of the stop or of the spin-1/2 heavy top-quark partner. The mass of the $\tilde{\chi}_1^0$ or A_0 is zero in each case. No signal sample with mass $m(T) = 200$ GeV has been simulated.

Top quark partner mass [GeV]	200	300	400	500	600
$\tilde{t}_1\tilde{t}_1$ production	0.02%	7.7%	22.0%	35.6%	43.0%
TT production	-	5.3%	15.8%	27.3%	34.3%

at the lowest mass splitting Δm are similar to those of $t\bar{t}$ background, with the differences increasing with Δm. Hence, the efficiency drops when $\Delta m(\tilde{t}_1, \tilde{\chi}_1^0)$, or $\Delta m(T, A_0)$, becomes closer to the top quark mass. For equal masses, the spin-1/2 top-quark partner signals have a slightly lower efficiency than the stop signals, due to helicity effects in the decay. More details will be given in the next section.

5.3.1 Event selection optimization

As previously explained, the analysis strategy is based on the selection of events with two leptons and a value of m_{T2} larger than the W mass. The analysis has been optimized maximizing the discovery significance, computed as $S/\sqrt{B + \delta B^2}$ where S is the signal rate, B the background from the full simulation, and δB the systematic uncertainty on the background, assumed to be 100%.

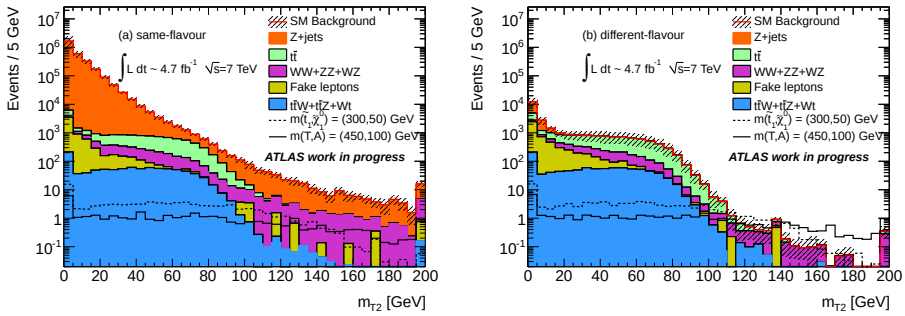

Figure 5.2: Expected distribution of the m_{T2} of the two leptons for the SF channel (a) and the DF channel (b).

In Fig. 5.2 the distribution of m_{T2} is shown requiring only two isolated leptons

in events that passed the trigger requirement. The distributions for a signal with a top squark mass of 300 GeV and a neutralino of 50 GeV, and a signal with a T mass of 450 GeV and an A mass of 100 GeV, are also reported for comparison.

In the DF channel the dominant backgrounds at high m_{T2} are $t\bar{t}$ and WW. These backgrounds present a sharp decrease around the W mass. The WW presents a longer tail populated by events where one the W is produced off-shell with a mass much higher than the W nominal mass.

In the SF channel, even after vetoing invariant masses in the Z region a long tail is observed, requiring additional cuts to separate the signal from the background. The Z+jets and diboson ($ZZ + WZ$) are the dominant backgrounds at large values of m_{T2}.

In Table 5.2 the expected rates of events with two leptons and with $m_{T2} > 120$ GeV are reported. No other selection is applied at this stage. It is evident that while part of the background is very effectively supressed by an m_{T2} cut, additional selections are required to supress the Z+jets, ZZ and ZW backgrounds.

For the $e\mu$ channel, this is obtained through the requirement on the two leading jets , which reduces the non-top backgrounds to the same level of the top, and it has a good signal acceptance. For the same flavour channels, additional cuts on the two lepton invatiant mass (Z peak veto) and on the presence of b-tagged jets have been considered. The b-tagging working point and the invariant mass window around the Z have been determined maximizing the expected signal significance. The signal selection described in the previous section has been chosen. The possibility of an E_{T}^{miss} cut has also been considered. However, ZZ and ZW events with high m_{T2} have also large E_{T}^{miss}, comparable to low-mass scalar top signals, so that an E_{T}^{miss} cut does not help against these. Furthermore, these backgrounds are effectively suppressed by the b-tag and invariant mass cuts which have been described, which also reduce the Z+jets to low levels. It was hence decided not to do an explicit E_{T}^{miss} cut.

The expected background and signal rates after all selections are reported in Table 5.3.

The final background rates in SF and DF channels are comparable. However, since this is achieved with more stringent cuts in the same flavour channels, the signal acceptance of these is smaller than the $e\mu$ channel. The $e\mu$ channel thus gives the stronger contribution to the expected sensitivity.

In Fig. 5.3 the number of expected signal events in the same flavour (left plots)

Table 5.2: Expected number of events with two leptons with $m_{T2} > 120$ GeV, for 4.71 fb^{-1}. The quoted errors are MC statistics only. The Drell-Yan background in the DF channel is expected to be negligible.

Process	same flavour	opposite flavour
$t\bar{t}$	0.40 ± 0.16	0.53 ± 0.15
$t\bar{t} + W$, $t\bar{t} + Z$	0.64 ± 0.06	0.20 ± 0.04
Wt	$0.00^{+0.17}_{-0.00}$	$0.10^{+0.17}_{-0.10}$
Drell-Yan	119 ± 5	-
$WW + WZ + ZZ$	32.7 ± 0.9	3.5 ± 0.3
total SM	153 ± 5	4.3 ± 0.4
m($\tilde{t}_1, \tilde{\chi}^0_1$) = (300,50) GeV	5.06	5.12
m(T,A) = (450,100) GeV	7.10	7.68

Table 5.3: Expected number of events passing all signal region cuts, for 4.71 fb^{-1}. The quoted errors are MC statistics only.The Drell-Yan background in the DF channel is expected to be negligible.

Process	SF	DF
$t\bar{t}$	0.19 ± 0.12	0.42 ± 0.14
$t\bar{t} + W$, $t\bar{t} + Z$	0.11 ± 0.03	0.18 ± 0.04
Wt	$0.00^{+0.17}_{-0.00}$	$0.10^{+0.17}_{-0.10}$
Drell-Yan	0.92 ± 0.29	-
$WW + WZ + ZZ$	0.04 ± 0.04	0.22 ± 0.09
total SM	1.26 ± 0.32	0.92 ± 0.20
m($\tilde{t}_1, \tilde{\chi}^0_1$) = (300,50) GeV	2.15	3.73
m(T,A) = (450,100) GeV	3.10	5.78

and opposite flavour (right plots) signal region is shown as a function of the top squark and neutralino masses, for the $\tilde{t}_1 \to t\tilde{\chi}^0_1$ scenario. In Fig. 5.4 the same information is reported for the $T \to tA_0$ scenario.

In Fig. 5.5 the acceptance of the signal region cuts is shown in the same mass plane. The acceptance is relative to the total cross section, hence it includes the 4.9% branching ratio in two leptons. It can be seen that the acceptance is very low

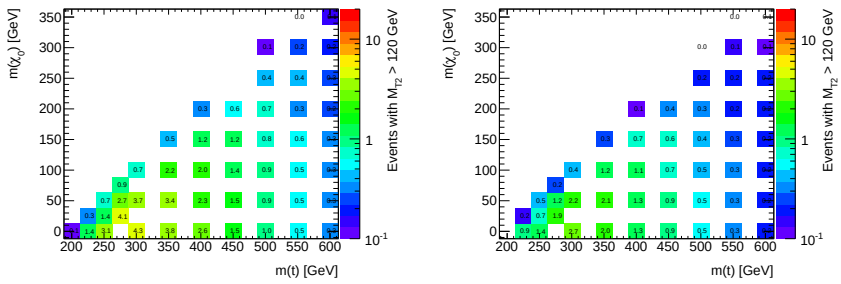

Figure 5.3: Expected number of signal events in the DF (left) and SF (right) signal regions, as a function of the scalar top and neutralino masses, for the scenario in which $\tilde{t}_1 \to t\tilde{\chi}_1^0$.

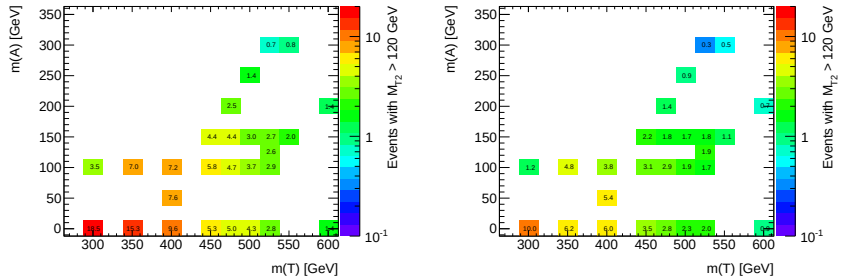

Figure 5.4: Expected number of signal events in the DF (left) and SF (right) signal regions, as a function of the spin 1/2 top partner T and neutral scalar A masses, for the scenario in which $T \to tA_0$.

for points near the $m(\tilde{t}_1) = m(t) + m(\tilde{\chi}_1^0)$ line. That is because the kinematic of signal events becomes very similar to those of $t\bar{t}$ events in that case, and the signal is thus drastically suppressed by the m_{T2} selection. The acceptance increases as the top squark mass increases.

The corresponding information for the spin 1/2 top partner scenario is reported in Fig. 5.6. The dependence of the acceptance on the masses of the particles is similar to that for the top squark case.

However, by comparing points of equal mass in Fig. 5.5 and Fig. 5.6, it can be observed that the acceptance for the spin 1/2 top partner case is lower than for the top squark partner case. Fig. 5.7 shows the angle between the W boson and the top quark in the center of mass frame of the latter (left) and between the charged

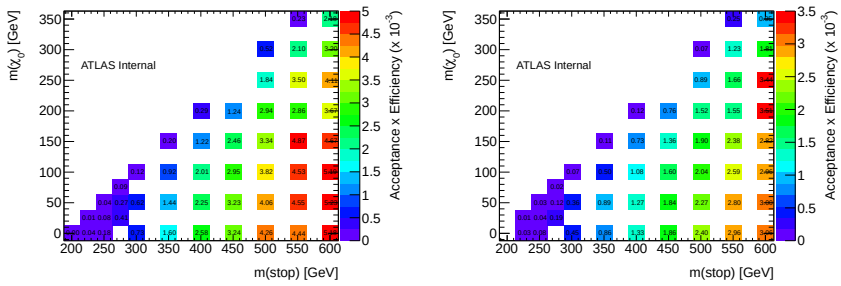

Figure 5.5: Acceptance of the DF (left) and SF (right) signal region selections, as a function of the top squarktop squark and neutralino masses, for the scenario in which $\tilde{t}_1 \to t\tilde{\chi}_1^0$.

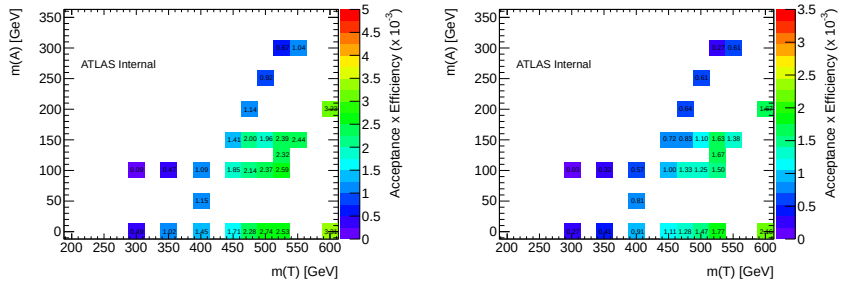

Figure 5.6: Acceptance of the DF (left) and SF (right) signal region selections,as a function of the spin 1/2 top partner T and neutral scalar A masses, for the scenario in which $T \to tA_0$.

lepton and the W boson in the center of mass frame of the latter (right). In the case of a spin 1/2 top partner, both the W and the charged lepton are emitted at larger angles with respect to the parent particle, with respect to the top squark samples. Thus, their p_T distributions is softer, resulting in a lower acceptance of the lepton p_T cuts, as well as in a softer m_{T2} distribution.

A summary of the SR selection criteria is reported in table 5.4.

Table 5.5 shows the amount of events passing these cuts in data, using the full analyzed data sample. The number of expected SM events, computed from MC before the application of the data driven scale factors described in section **??**, is shown in Table 5.6. The expected rates for one signal benchmark ($m_{\tilde{t}_1} = 400$ GeV and $m_{\tilde{\chi}_1^0} = 0$ GeV) are also reported.

Table 5.4: Selection of signal candidates.

Cut	Value
p_T cut on trigger lepton	$p_T > 25(20)$ GeV for electrons (muons)
p_T cut on second lepton	$p_T > 20(10)$ GeV for electrons (muons)
p_T cut for third lepton veto	$p_T > 20(10)$ GeV for electrons (muons)
Opposite sign	reject same charge leptons
Dilepton invariant mass	$m_{ll} > 20$ GeV
Jet cuts	$p_T > 50(25)$ GeV for leading (sub-leading) jets
b-jets	SF: at least one b-tagged jet
Z veto	SF: $m_{ll} < 71$ GeV or $m_{ll} > 111$ GeV
m_{T2}	> 120 GeV

Table 5.5: Number of events passing cuts at various cutflow stages for data. The b-Jets and Z veto selections are applied only for the same flavor channels.

Cut	$e^{\pm}e^{\mp}$	$\mu^{\pm}\mu^{\mp}$	$e^{\pm}\mu^{\mp}$
Two Leptons	1144726	915701	28002
Jet cuts	32520	54657	7878
b-Jets	4573	7676	-
Z Veto	1758	3137	-
$m_{T2} > 120$ GeV	1	0	2

Table 5.6: Expected number of MC events for some of the main background sources to opposite-sign ee (top), $\mu\mu$ (middle), $e\mu$ (bottom) channels for an integrated luminosity of 4.7fb^{-1}. The sum of these contributions is reported as "SM total" and, for comparison, the number of expected events for one signal benchmark ($m_{\tilde{t}_1} = 400$ GeV and $m_{\tilde{\chi}_1^0} = 0$ GeV) is also shown.

Cut ↓	$t\bar{t}$	Wt	Dibosons	Z+jets	SM total	Signal
MC → $(e^{\pm}e^{\mp})$						
Two Leptons	3320	353	671	1043602	1049367	6
Jet cuts	2285	108	52.10	29780	32572	5
b-Jets	1769	70	6	1222	3107	4
Z Veto	1241	50	3	87	1382	3
$m_{T2} > 120$ GeV	0.086	0	0.022	0	0.12	0.72
MC → $(\mu^{\pm}\mu^{\mp})$						
Two Leptons	5693	578	1265	1800795	1810639	8
Jet cuts	4607	354	185	125097	131162	7
b-Jets	3022	118	8	1987	5200	5
Z Veto	2165	83	4	182	2439	4
$m_{T2} > 120$ GeV	0.11	0	0.032	0.60	0.71	0.70
MC → $(e^{\pm}\mu^{\mp})$						
Two Leptons	8940	924	1283	9781	21688	14
Jet cuts	7255	582	197	1059	9130	13
$m_{T2} > 120$ GeV	0.42	0.1	0.14	0	0.75	2.4

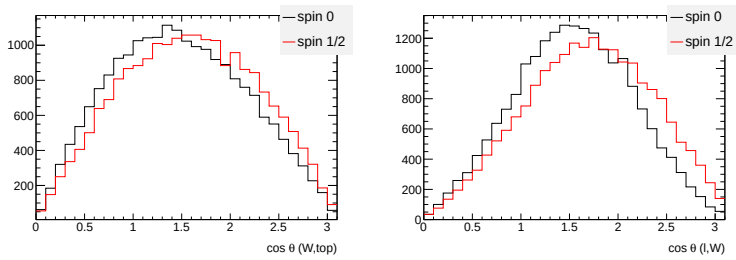

Figure 5.7: Truth-level distribution of the angle between the W boson and its parent top quark direction in the rest frame of the top quark (left) and between the charged leptons and their parent W boson direction in the rest frame of the W boson (right), for a top squark sample with $m(\tilde{t}_1) = 400$ GeV and $m(\tilde{\chi}_1^0) = 100$ GeV (black curves) and a spin 1/2 top partner sample with $m(T) = 400$ GeV and $m(A) = 100$ GeV (red curves).

The expected discovery significance is shown in Fig. 5.8 for the $\tilde{t}_1 \to t\tilde{\chi}_1^0$ scenario, and in Fig. 5.9 for the spin 1/2 scenario, for an integrated luminosity of 4.7 fb^{-1}.

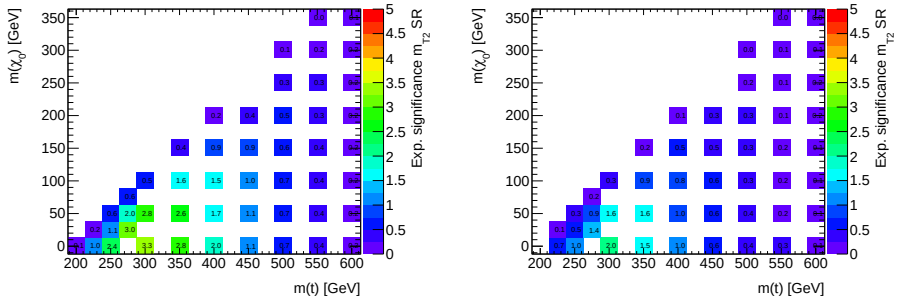

Figure 5.8: Expected signal significance as a function of the $\tilde{t}_1$ and $\tilde{\chi}_1^0$ masses, for the scenario with a $\tilde{t}_1 \to t\tilde{\chi}_1^0$ decay. The left figure shows the DF channel and the right figure shows the SF channel.

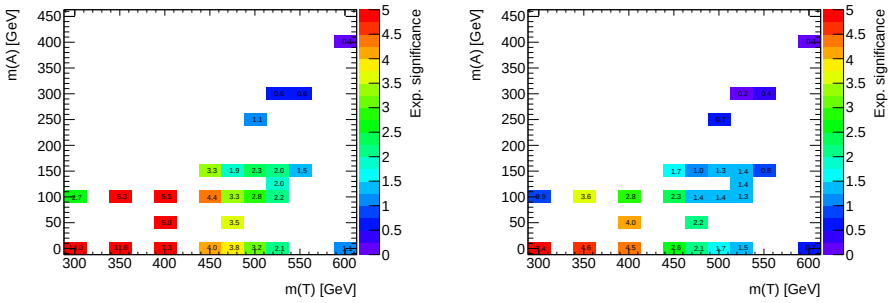

Figure 5.9: Expected signal significance as a function of spin 1/2 top partner and dark matter candidate masses. The left figure shows the DF channel and the right figure shows the SF channel.

5.4 Kinematic distributions

In this section, a comparison is made between data and MC simulation for the main observables used in the analysis. In all plots, the MC uses the nominal cross sections (i.e., the scale factors from CR measurements are not included). The uncertainty band includes the MC statistics, the main detector response uncertainties (JES, JER, and E_T^{miss} cellout term), the cross section uncertainty, the generator and ISR/FSR uncertainties for $t\bar{t}$. A comprehensive description of the systematic uncertainties will be given in section 5.6. The distributions are also shown separately for the same and different flavor channels. The overall agreement between data and Monte Carlo is good.

Figures 5.10, 5.11, 5.12, 5.13 and 5.16 show the distributions of the p_T of the leading lepton, the p_T of the sub-leading lepton, the p_T of the leading jet, the p_T of the sub-leading jet and of the transverse missing energy respectively, after all selection cuts but for m_{T2}.

The jet and b-jet multiplicity distributions are shown in Figures 5.14 and 5.15, for the same selection level. The b-jet multiplicity distribution for SF events shows the Z/γ^*+jets and diboson rejection power of the chosen cut. The discrepancy between the nominal background prediction and the data at large jet multiplicities is mainly due to the poor performance of MC@NLO in describing these kinematic regions. However, the discrepancy is covered by the uncertainty computed from the generator comparison with ALPGEN and POWHEG and doesn't have any significant impact on the analysis, since this region corresponds to a very small fraction of the total events.

The effectiveness of the Z veto applied on SF events can be appreciated from the invariant mass distribution of the two leptons, shown in Figures 5.17 for events passing the trigger requirements and the selection of 2 isolated leptons.

The m_{T2} distribution is shown in figure 5.18, after all selection cuts but for m_{T2} itself.

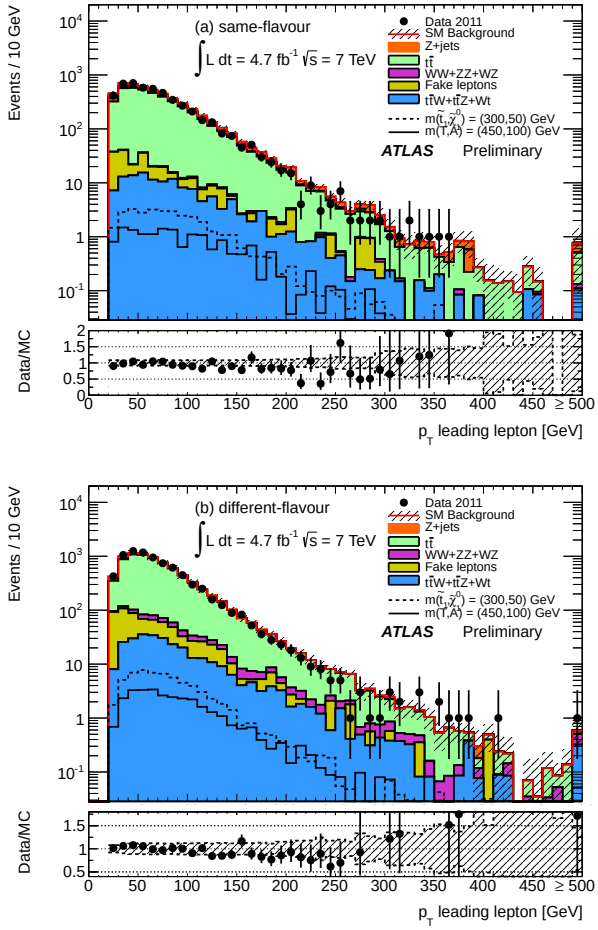

Figure 5.10: p_T distribution for the leading lepton in events passing all the signal candidate selection requirements, expect that on m_{T2}, for same-flavour events (a) and different-flavour events (b). The contributions from all SM backgrounds are shown, with the bands representing the total uncertainty. The distributions of the signal expected for two different models are also shown: the dashed line corresponds to signal with a 300 GeV top squark and a 50 GeV neutralino, while the solid line corresponds to a signal with a 450 GeV spin-1/2 top quark partner T and a 100 GeV A_0 particle.

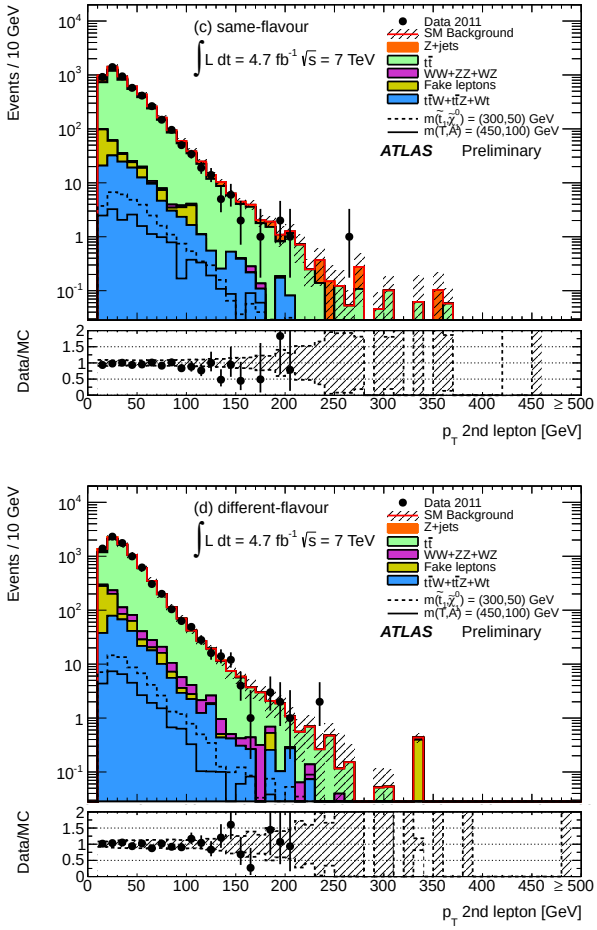

Figure 5.11: p_T distribution for the sub-leading lepton in events passing all the signal candidate selection requirements, expect that on m_{T2}, for same-flavour events (c) and different-flavour events (d). The contributions from all SM backgrounds are shown, with the bands representing the total uncertainty. The distributions of the signal expected for two different models are also shown: the dashed line corresponds to signal with a 300 GeV top squark and a 50 GeV neutralino, while the solid line corresponds to a signal with a 450 GeV spin-1/2 top quark partner T and a 100 GeV A_0 particle.

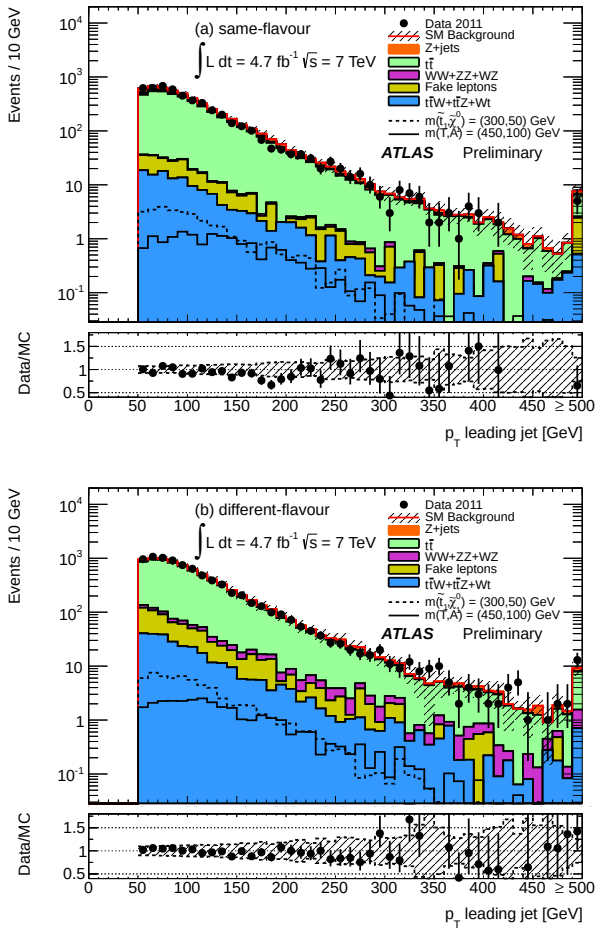

Figure 5.12: p_T distribution for the leading jet in events passing all the signal candidate selection requirements, expect that on m_{T2}, for same-flavour events (a) and different-flavour events (b). The contributions from all SM backgrounds are shown, with the bands representing the total uncertainty. The distributions of the signal expected for two different models are also shown: the dashed line corresponds to signal with a 300 GeV top squark and a 50 GeV neutralino, while the solid line corresponds to a signal with a 450 GeV spin-1/2 top quark partner T and a 100 GeV A_0 particle.

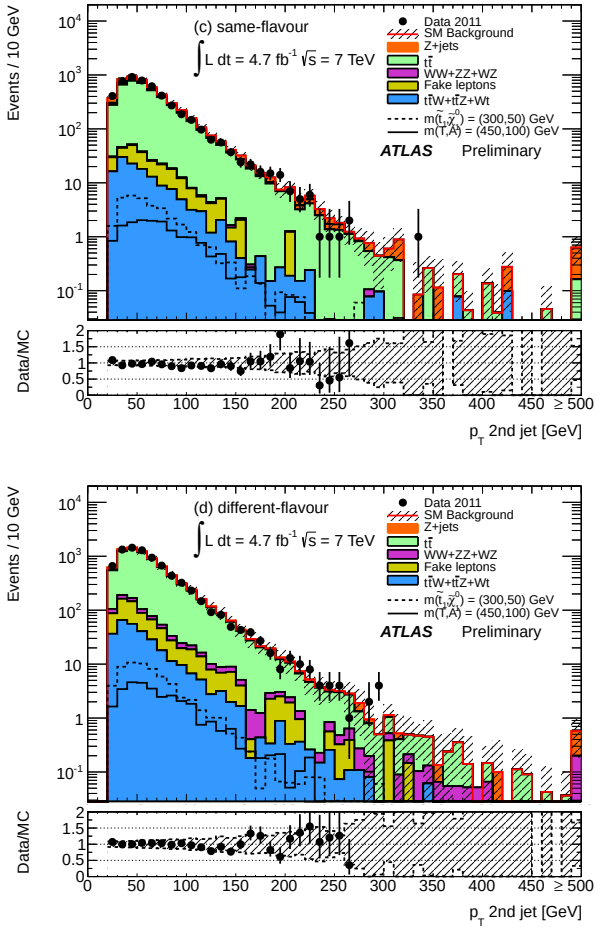

Figure 5.13: p_T distribution for the sub-leading jet in events passing all the signal candidate selection requirements, expect that on m_{T2}, for same-flavour events (c) and different-flavour events (d). The contributions from all SM backgrounds are shown, with the bands representing the total uncertainty. The distributions of the signal expected for two different models are also shown: the dashed line corresponds to signal with a 300 GeV top squark and a 50 GeV neutralino, while the solid line corresponds to a signal with a 450 GeV spin-1/2 top quark partner T and a 100 GeV A_0 particle.

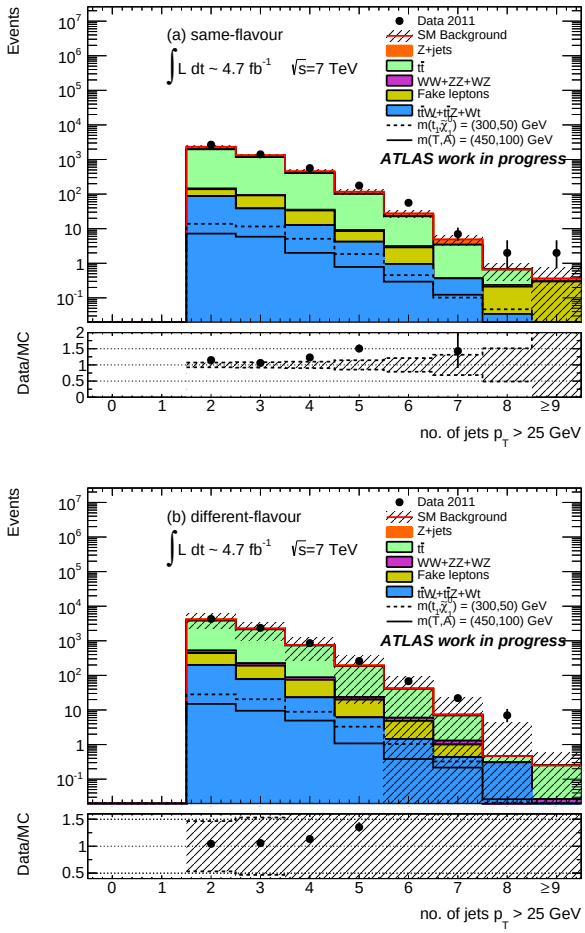

Figure 5.14: Jet multiplicity distribution in events passing all the signal candidate selection requirements, expect that on m_{T2}, for same-flavour events (a) and different-flavour events (b). The contributions from all SM backgrounds are shown, with the bands representing the total uncertainty. The distributions of the signal expected for two different models are also shown: the dashed line corresponds to signal with a 300 GeV top squark and a 50 GeV neutralino, while the solid line corresponds to a signal with a 450 GeV spin-1/2 top quark partner T and a 100 GeV A_0 particle.

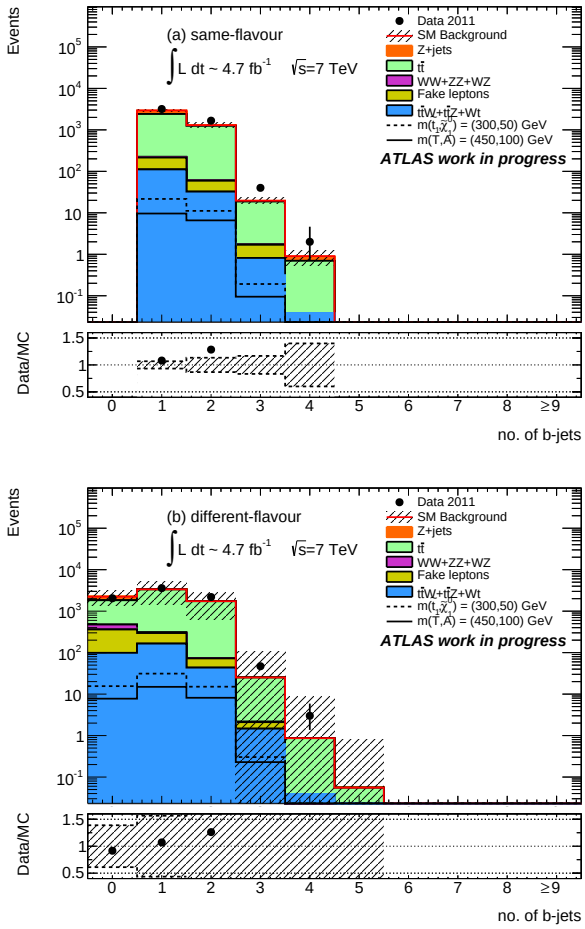

Figure 5.15: b-tagged jet multiplicity distribution in events passing all the signal candidate selection requirements, expect that on m_{T2}, for same-flavour events (a) and different-flavour events (b). The contributions from all SM backgrounds are shown, with the bands representing the total uncertainty. The distributions of the signal expected for two different models are also shown: the dashed line corresponds to signal with a 300 GeV top squark and a 50 GeV neutralino, while the solid line corresponds to a signal with a 450 GeV spin-1/2 top quark partner T and a 100 GeV A_0 particle.

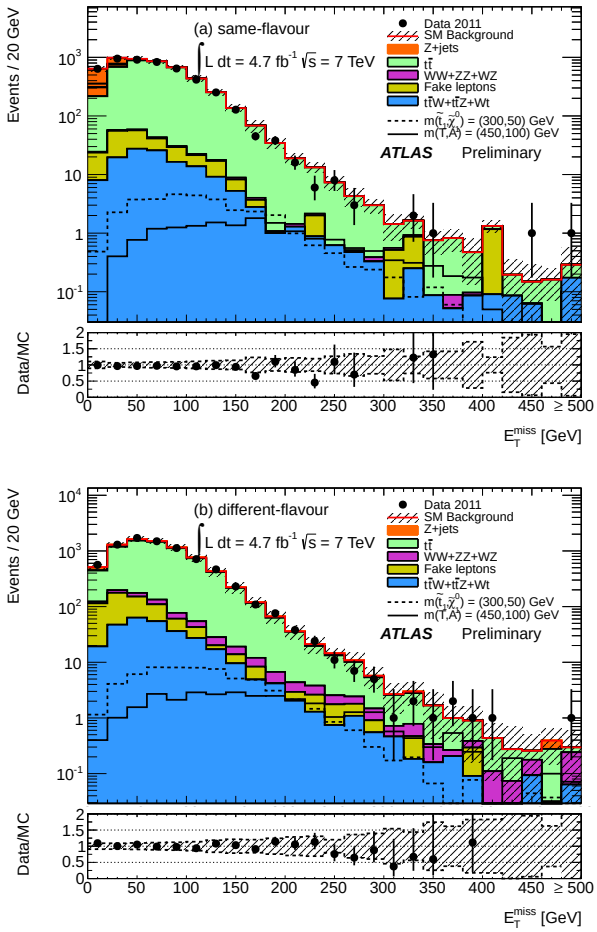

Figure 5.16: Missing transverse momentum distribution in events passing all the signal candidate selection requirements, expect that on m_{T2}, for same-flavour events (c) and different-flavour events (d). The contributions from all SM backgrounds are shown, with the bands representing the total uncertainty. The distributions of the signal expected for two different models are also shown: the dashed line corresponds to signal with a 300 GeV top squark and a 50 GeV neutralino, while the solid line corresponds to a signal with a 450 GeV spin-1/2 top quark partner T and a 100 GeV A_0 particle.

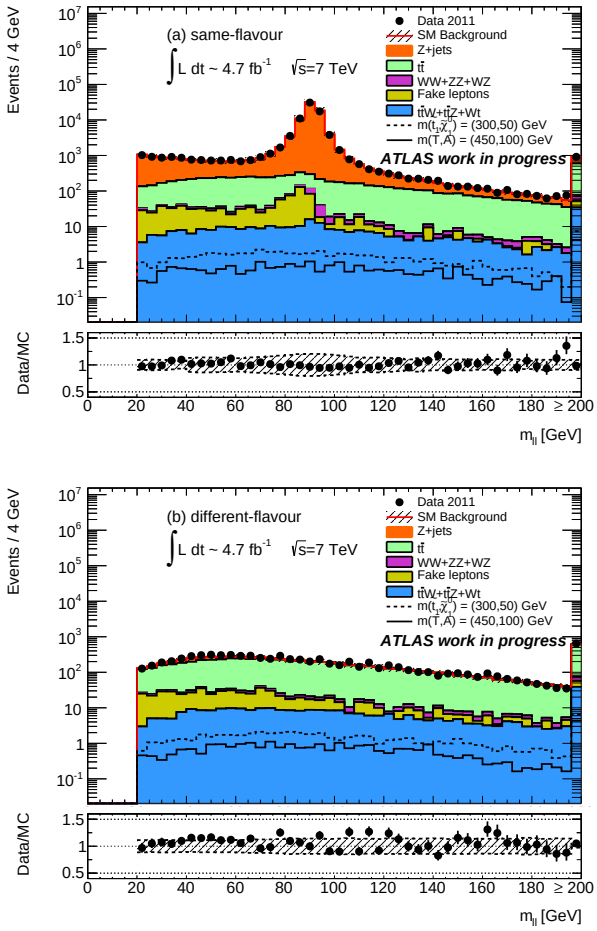

Figure 5.17: $m_{\ell\ell}$ distribution in events passing all the signal candidate selection requirements, expect that on m_{T2} and $m_{\ell\ell}$, for same-flavour events (a) and different-flavour events (b). The contributions from all SM backgrounds are shown, with the bands representing the total uncertainty. The distributions of the signal expected for two different models are also shown: the dashed line corresponds to signal with a 300 GeV top squark and a 50 GeV neutralino, while the solid line corresponds to a signal with a 450 GeV spin-1/2 top quark partner T and a 100 GeV A_0 particle.

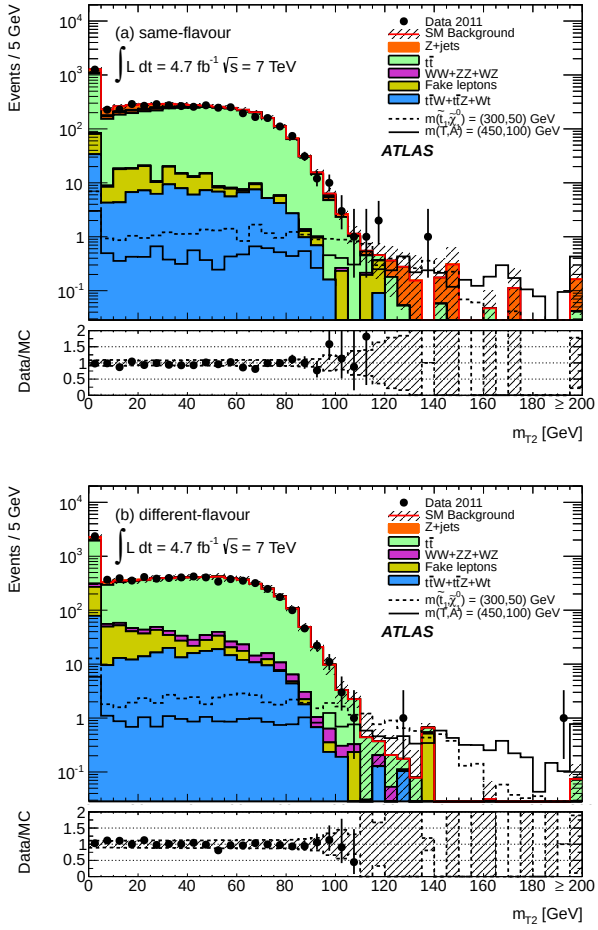

Figure 5.18: m_{T2} distribution in events passing all the signal candidate selection requirements, expect that on m_{T2}, for same-flavour events (a) and different-flavour events (b). The contributions from all SM backgrounds are shown, with the bands representing the total uncertainty. The distributions of the signal expected for two different models are also shown: the dashed line corresponds to signal with a 300 GeV top squark and a 50 GeV neutralino, while the solid line corresponds to a signal with a 450 GeV spin-1/2 top quark partner T and a 100 GeV A_0 particle.

5.5 Background estimate

The dominant SM background contribution to the SR is expected to be the top pair production. The normalization of this background is determined using the number of observed events in a control region (CR) populated mostly by $t\bar{t}$ events. The same approach is used to estimate the number of Z/γ^*+jets events. Cross-contamination between the respective CRs has been found negligible and hence both these backgrounds can be normalized independently.

Additional SM processes yielding two isolated leptons and $E_{\mathrm{T}}^{\mathrm{miss}}$ (diboson, Wt, Z+jets, Drell-Yan, $t\bar{t}+W$and $t\bar{t}+Z$) and providing a sub-dominant contribution to the SR are determined from MC.

The fake lepton background consists of semi-leptonic $t\bar{t}$, s-channel and t-channel single top, W+jets and light- and heavy-flavour jet production. The contribution from this background is small (less than 10% of the total background). It is estimated from data with a method described in section 5.5.4.

5.5.1 $t\bar{t}$ background

The dileptonic $t\bar{t}$ background contribution to the SR is estimated with a semi-data driven method. The number of $t\bar{t}$ events in the signal region N_{top}^{SR} is estimated by rescaling the number of events in data in a control region by a transfer factor measured on MC.

$$N_{t\bar{t}}^{SR} = \frac{N_{t\bar{t}}^{MC,SR}}{N_{t\bar{t}}^{MC,CR}} \times N_{t\bar{t}}^{data,CR} \tag{5.2}$$

In calculating $N_{t\bar{t}}^{MC,SR}$ and $N_{t\bar{t}}^{MC,CR}$ only MC $t\bar{t}$ events in which both W decay into leptons are considered, since the semileptonic and fully hadronic $t\bar{t}$ contributions to the background is already included in the data driven fake background estimation.

The CR is defined as events passing all the selection cuts but within an intermediate $\mathrm{m_{T2}}$ region, between 85 GeV and 100 GeV. The choice of this region has been driven by two different motivations:

- the uncertainty on the final estimation is dominated by the available MC statistics in the SR: so there would be no gain in expanding the CR either to lower or higher values of $\mathrm{m_{T2}}$.
- the 85 GeV - 100 GeV $\mathrm{m_{T2}}$ interval cannot be moved closer to the SR, as this would make the signal contamination much more important

The number of events in the CR $N_{t\bar{t}}^{data,CR}$ is estimated by correcting the data events in the CR for other background sources estimated from MonteCarlo or, in the case of the fake lepton background, with the data driven method described in Section 5.5.4.

$$N_{t\bar{t}}^{data,CR} = N^{data,CR} - N_{non-t\bar{t}}^{CR} \tag{5.3}$$

where $N_{non-t\bar{t}}^{CR}$ includes background sources different from fully leptonic top pairs.

Table 5.7 shows the rates of all expected backgrounds and observed data in the CR: please note that $t\bar{t}$ is indeed the dominant process in this region.

Table 5.7: CR composition for 4.71 fb^{-1}. The quoted uncertainties include both statistical and systematic uncertainties. The Z+jets rate in the DF channel is negligible for the reasons discussed in Section 5.5.2.

Process	DF rate in CR	SF rate in CR
$t\bar{t}$	68.1 ± 11.4	39.0 ± 11.2
$t\bar{t}+W$, $t\bar{t}+Z$	0.33 ± 0.09	0.17 ± 0.06
single top	2.7 ± 1.0	1.8 ± 0.5
Z/γ^*+jets	-	3.5 ± 1.4
Fakes	0.4 ± 0.3	0.5 ± 1.6
Diboson	0.49 ± 0.27	0.11 ± 0.10
Total non-$t\bar{t}$	3.9 ± 1.6	6.1 ± 3.7
Total Expected	72 ± 11	45 ± 12
Data	79	53

The signal contamination in the CR is shown in figure 5.19 as a function of both $\tilde{t}_1$(T) and $\tilde{\chi}_1^0(A_0)$ masses. The values reported in the figures are $N_{\text{signal}}^{CR}/(N^{data,CR} - N_{non-t\bar{t}}^{CR})$, which is the relative effect of the signal contamination on the top background normalization. The contamination is larger for smaller values of these masses: however, it is generally found to be small or negligible in the CR. In the top squark case, non-negligible signal contamination appears for a top squark mass around 200 GeV. The resulting background overestimation of about 20% will lower the sensitivity to a signal with those characteristics. However the analysis results won't be affected significantly, because of the low sensitivity to such a signal due to the similarity of the m_{T2} distributions for signal and backgrounds. In

the spin 1/2 case, the contamination is relevant for T masses well below the previously published limit.

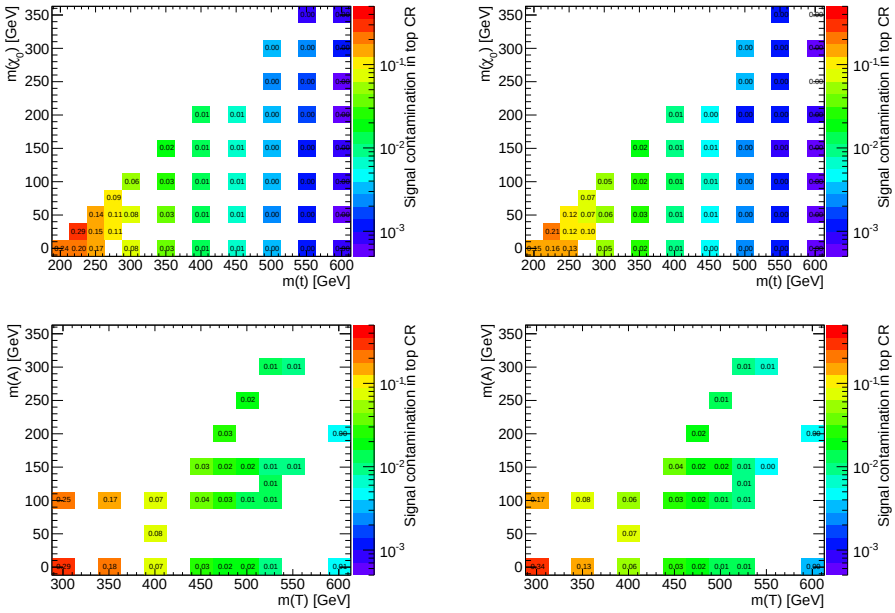

Figure 5.19: The plots show the rate of signal events inside the CR for 4.71 fb^{-1}as a function of top squark and neutralino masses (first row) or T and A masses (second row), normalized to the data driven top normalization. The plots in the first column show the rates for the DF channel, while those on the right are for the same flavor channel. The largest signal contamination appears for the lowest values of the particle masses.

In order to match the number of events observed in the CR (Table 5.7), a $t\bar{t}$ scale factor of 1.10 ± 0.13 and 1.21 ± 0.19 is needed for the DF and SF channels respectively, with the uncertainty dominated by the observed statistics.

By using Eq. 5.2, the predicted $t\bar{t}$ rate in the SR is found to be 0.43 ± 0.48 for the DF channel and 0.23 ± 0.23 for the SF channel.

$t\bar{t}$ MC generator uncertainty

The uncertainty associated to the choice of a specific MonteCarlo generator is the leading systematic on the SR/CR ratio in the DF channel and the sub-leading systematic in the SF channel, after MC statistics. Table 5.8 provides more details

on this uncertainty, reporting the rates predicted by each of the generators used in this estimation.

The nominal MC@NLO sample predictions are compared with the predictions of POWHEG (with two different hadronisation simulations done using PYTHIA and HERWIG) and ALPGEN. Since the POWHEG samples were reconstructed with a simplified detector simulation (*fast simulation*), also a dedicated MC@NLO sample has been reconstructed with the same simulation to produce a sensible comparison.

The sum in quadrature of the three differences is taken as final $t\bar{t}$ generator uncertainty. These differences, while large, are all within the MC statistical uncertainty for the SR prediction and the SR/CR ratio.

Table 5.8: The tables show the $t\bar{t}$ expected rate in CR, SR and their ratio, as predicted by different MC generators. All uncertainties are the MC statistics.

	MC@NLO	**MC@NLO** *fast sim.*	**POWHEG** (Pythia)	**POWHEG** (Herwig)	**Alpgen**
			Different Flavour		
CR	68.1 ± 1.8	70.1 ± 2.1	73.3 ± 3.6	73.0 ± 3.6	67.5 ± 2.8
SR	0.39 ± 0.13	0.17 ± 0.12	0.52 ± 0.30	0.34 ± 0.21	0.24 ± 0.18
SR/CR $\times 10^{-3}$	5.7 ± 2.0	2.5 ± 1.7	7.1 ± 4.1	4.7 ± 2.9	3.6 ± 2.6
			Same Flavour		
CR	39.0 ± 1.3	44.3 ± 1.7	46.5 ± 2.8	44.3 ± 2.8	30.5 ± 1.7
SR	0.19 ± 0.12	0.26 ± 0.14	0.35 ± 0.23	0.34 ± 0.25	0.15 ± 0.09
SR/CR $\times 10^{-3}$	4.9 ± 3.0	5.8 ± 3.2	7.6 ± 5.0	7.7 ± 5.6	4.8 ± 2.8

5.5.2 Z+jets background

The background from Z/γ^*+jets can be divided in two components, depending on the flavor of the final state leptons. The case where the Z decays into leptons and muons and the case where it decays in taus must be evaluated separately for two reasons: the decay into electrons and muons does not provide a significant background for the DF channel, and the m_{T2} distribution is very different for the two cases, as can be seen in Fig. 5.20, where the decay into taus does not contribute

to the high m_{T2} tail. In the following the estimation of the contribution of the decay into e and μ to the SF channel of the analysis is described.

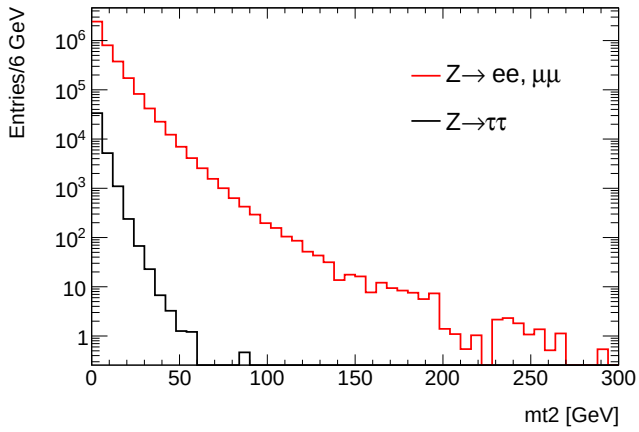

Figure 5.20: Distribution of m_{T2} for Z decaying into e and μ (red) or in τ (black) for events with two signal leptons.

In order to perform this estimate four regions are defined (see Fig. 5.21):

- nZ_SR: $m_{T2} > 120$ GeV and $m_{\ell\ell}$ outside of the (71,111) GeV window. This corresponds to the SR, minus the b-tagging requirement.
- nZ_CR: $90 < m_{T2} < 120$ GeV and $m_{\ell\ell}$ outside of the (71,111) GeV window.
- Z_SR: $m_{T2} > 120$ GeV and $m_{\ell\ell}$ inside the (71,111) GeV window.
- Z_CR: $90 < m_{T2} < 120$ GeV and $m_{\ell\ell}$ inside of the (71,111) GeV window.

Tables 5.9 and 5.10 show the data and MonteCarlo yields for events passing all of the selection cuts for the SF channel, except the Z veto and the m_{T2} cut, for the four regions respectively without and with the b-tagging requirement. A good agreement between data and Monte Carlo is observed both for the DF samples dominated by $t\bar{t}$, Wt, WW production and the SF ones with a significant Z contribution.

The baseline estimate is performed analogously to what is done for the $t\bar{t}$ background in a semi data-driven way as:

$$Z/\gamma^* + jets(b\_nZ\_SR) = Data_{sub}(b\_Z\_SR) \times F_{MC}$$

Table 5.9: Data and Monte Carlo yields for events passing all of the selection cuts except Z veto, m_{T2} and b-tagging requirement. The Z/γ^*+jets includes all $Z \to ee$ or $\mu\mu$). The label *others* indicates the sum of $t\bar{t}$, Wt, WW, $Z \to \tau\tau$,ZZ and WZ. Total uncertainties are shown (statistics + systematics).

Sample	**Data (SF)**	Z/γ^***+jets (SF)**	$t\bar{t}$ **(SF)**	**others (SF)**
Z_CR	231.00	239.61 ± 13.20	13.11 ± 1.52	14.78 ± 1.13
Z_SR	74.00	71.97 ± 4.71	-0.02 ± 0.06	9.54 ± 0.83
nZ_CR	70.00	27.90 ± 2.48	32.31 ± 3.47	2.79 ± 0.49
nZ_SR	10.00	8.03 ± 1.03	0.28 ± 0.13	0.04 ± 0.03

Sample	**Data (DF)**	Z/γ^***+jets (DF)**	$t\bar{t}$ **(DF)**	**others (DF)**
Z_CR	10.00	0.00 ± 0.00	9.92 ± 1.28	0.53 ± 0.27
Z_SR	0.00	0.00 ± 0.00	0.00 ± 0.06	0.00 ± 0.00
nZ_CR	37.00	0.00 ± 0.00	33.45 ± 3.65	3.27 ± 0.72
nZ_SR	2.00	0.00 ± 0.00	0.42 ± 0.13	0.20 ± 0.26

Table 5.10: Data and Monte Carlo yields for events passing all of the selection cuts except Z veto and m_{T2}. The Z/γ^*+jets includes all $Z \to ee$ or $\mu\mu$). The label *others* indicates the sum of $t\bar{t}$, Wt, WW, $Z \to \tau\tau$,ZZ and WZ. Total uncertainties are shown (statistics + systematics).

Sample	**Data (SF)**	Z/γ^***+jets (SF)**	$t\bar{t}$ **(SF)**	**others (SF)**
b_Z_CR	33.00	23.66 ± 1.94	10.06 ± 1.20	1.91 ± 0.37
b_Z_SR	11.00	7.03 ± 1.10	0.03 ± 0.03	0.53 ± 0.16
b_nZ_CR	39.00	2.53 ± 0.60	24.82 ± 2.70	1.40 ± 0.34
b_nZ_SR	1.00	0.92 ± 0.29	0.19 ± 0.12	0.00 ± 0.00

Sample	**Data (DF)**	Z/γ^***+jets (DF)**	$t\bar{t}$ **(DF)**	**others (DF)**
b_Z_CR	7.00	0.00 ± 0.00	7.42 ± 1.01	0.12 ± 0.10
b_Z_SR	0.00	0.00 ± 0.00	0.00 ± 0.06	0.00 ± 0.00
b_nZ_CR	29.00	0.00 ± 0.00	25.85 ± 2.88	1.39 ± 0.36
b_nZ_SR	1.00	0.00 ± 0.00	0.34 ± 0.11	0.13 ± 0.25

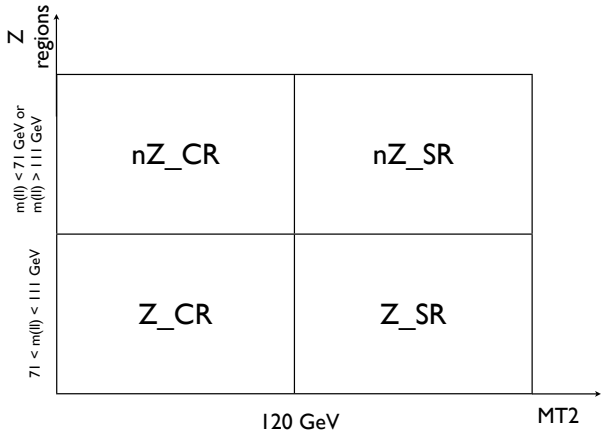

Figure 5.21: Definition of the four regions used to perform the estimate of the Z+jets Background.

where $Data_{sub}$ indicates the data from which the MC estimate of all the contributions different from Z/γ^*+jets are subtracted. The factor F_{MC} is the extrapolation factor from the Z to the nZ region calculated with the Z/γ^*+jets Monte Carlo as

$$F_{MC} \equiv \frac{Z/\gamma^* + jets(nZ\_SR)}{Z/\gamma^* + jets(Z\_SR)} = 0.11 \pm 0.01$$

This factor is calculated for the Z/γ^*+jets Monte Carlo without b-tagging as the number of Monte Carlo events for Z/γ^*+jets in the b-tagged signal region is zero. The estimate thus performed yields:

$$Z/\gamma^* + jets(b\_nZ\_SR) = 1.17 \pm 0.40$$

where the error includes the statistical error on data in the CR and the statistical error of the Monte Carlo, and is dominated by the statistical error of the data in the control region.

The assumption underlying this estimate is that the b-tagging requirement does not affect the calculation of F_{MC}, and that this number is correctly simulated in the Monte Carlo. The b-tagging independence can be studied by re-evaluating the Monte Carlo transfer factor F_{MC} from the Z mass peak to the nZ region in the control region with $90 < m_{\mathrm{T2}} < 120$ GeV. The obtained numbers are 0.12 ± 0.01 if no b-tagging is applied, and 0.11 ± 0.03 with b-tagging applied, thus showing

that in a kinematic region very close to the signal region the b-tagging does not influence significantly the value of F_{MC}.

5.5.3 Minor backgrounds

The diboson production is estimated with Monte Carlo simulation, normalised to the NLO cross sections of 43.8 ± 2.8 pb, 19.1 ± 1.3 pb, and 6.2 ± 0.3 pb for WW, WZ, and ZZ respectively. The most relevant of these backgrounds is WW which has the highest $\sigma \times BR$ for two lepton production, and for which the $\mathrm{m_{T2}}$ distribution extends to much higher higher values than for $t\bar{t}$, making it the dominant backgrounds for $m_{\mathrm{T2}} > 120$ GeV.

For the single top, only the Wt process is included, and the s-channel and t-channel contribution are included by the data driven estimate of processes with at least one fake or non isolated lepton described in the next section.

For $t\bar{t} + W$and $t\bar{t} + Z$the Leading Order (LO) MadGraph samples are used. The sensitivity to higher order QCD radiation is expected to be small because the signal region selection does not require more jets than present at LO.

5.5.4 Fake lepton background

The background originating from fake leptons includes double-fake sources from the QCD multi-jet background, with misidentified jets and non-prompt leptons, and true-fake sources such as $t\bar{t}$ and W/Z+jets in both electron and muon channels. Photon conversions also contribute as a background source of fake leptons.

The fake lepton background is estimated with the data-driven Matrix Method: this method relies on two lepton selection criteria (referred to as "tight" and "loose") to extract the number of expected events with real(R)-fake(F) and fake(F)-fake(F) leptons directly from data by comparing the observed composition of the dilepton sample in terms of tight and exclusively loose leptons. Tight leptons pass all standard object selection requirements as described in section 5.2. Exclusively loose leptons differ from tight leptons by failing isolation requirements. In the following, N refers to the number of events with one or two leptons fulfilling loose (L), exclusively loose (l) or tight (T) requirements. The notation N_{lT} or N_{Tl} translates into ordered lepton pairs.

The fake rate f and the real efficiency r are defined as the probabilities that a

fake or real loose lepton will pass the tight criteria as in Eq. 5.4

$$f = \frac{N_T^F}{N_L^F} \quad \text{and} \quad r = \frac{N_T^R}{N_L^R} \tag{5.4}$$

Considering events with two leptons, one has:

$$\begin{cases} N_{TT}^{RR} = N_{LL}^{RR} r_1 r_2 \\ N_{TT}^{RF} = N_{LL}^{RF} r_1 f_2 \\ N_{TT}^{FR} = N_{LL}^{FR} f_1 r_2 \\ N_{TT}^{FF} = N_{LL}^{FF} f_1 f_2 \end{cases} \tag{5.5}$$

The number of events with double-fake and fake-real tight leptons (N_{TT}^{FF} and $N_{TT}^{RF} + N_{TT}^{FR}$ respectively) can be obtained from the number of events with double-fake and fake-real loose leptons (N_{LL}^{FF} and $N_{LL}^{RF} + N_{LL}^{FR}$) once the fake rates f_i and efficiencies r_i are known. In turn, N_{TT}^{FF}, N_{TT}^{FR} and N_{TT}^{RF} can be obtained by inverting the matrix M:

$$\begin{pmatrix} N_{TT} \\ N_{Tl} \\ N_{lT} \\ N_{ll} \end{pmatrix} = M \begin{pmatrix} N_{LL}^{RR} \\ N_{LL}^{RF} \\ N_{LL}^{FR} \\ N_{LL}^{FF} \end{pmatrix} \tag{5.6}$$

with:

$$M = \begin{pmatrix} r_1 r_2 & r_1 f_2 & f_1 r_2 & f_1 f_2 \\ r_1(1-r_2) & r_1(1-f_2) & f_1(1-r_2) & f_1(1-f_2) \\ (1-r_1) r_2 & (1-r_1) f_2 & (1-f_1) r_2 & (1-f_1) f_2 \\ (1-r_1)(1-r_2) & (1-r_1)(1-f_2) & (1-f_1)(1-r_2) & (1-f_1)(1-f_2) \end{pmatrix} \tag{5.7}$$

It is possible to extract the contribution due to double-fake and fake-real events in the signal region (N_{TT}^{FF} and $N_{TT}^{FR} + N_{TT}^{RF}$) from the observable quantities N_{TT}, N_{Tl}, N_{lT} and N_{ll}.

The Matrix Method relies on suitable control regions for determining the fake rate and real efficiency, as described in the following.

Fake rate

The fake rate is estimated in QCD-enriched CRs, defined in Table 5.11, exploiting cuts on the event E_{T}^{miss}, jet multiplicity n_{jets} and angular separation $\Delta\phi(\ell, E_{\mathrm{T}}^{miss})$.

In the case of the two-lepton CRs (defined from a $e\mu$ same-sign sample) an anti-tag&probe method is used: one of the two leptons in the event is tagged to be exclusively loose (anti-tag) and the other is probed against tight requirements.

For each CR, the contamination of events with prompt (real) leptons originating from SM background such as W+jets, Z+jets, top pairs, single top and di-bosons, has been evaluated by MC and subtracted to the number of observed events in data.

Table 5.11: QCD-enriched control regions used for the fake rate measurement: definition, number of events with (exactly) one loose lepton N_L, number of events with (exactly) one tight lepton N_T.

CR	**Selection**	$\mathbf{N}_L$	$\mathbf{N}_T$
1L(e)	$E_{\mathrm{T}}^{miss} < 25$, $n_{jets} \geq 2$, $\Delta\phi(\ell, E_{\mathrm{T}}^{miss}) < 0.5$	2.0×10^6	0.5×10^6
1L(μ)	$E_{\mathrm{T}}^{miss} < 25$, $n_{jets} \geq 2$, $\Delta\phi(\ell, E_{\mathrm{T}}^{miss}) < 0.5$	9.9×10^5	3.8×10^5
2L(μe)	same-sign, anti-tag, $E_{\mathrm{T}}^{miss} < 25$, $n_{jets} > 0$	1.8×10^4	0.4×10^4
2L($e\mu$)	same-sign, anti-tag, $E_{\mathrm{T}}^{miss} < 25$, $n_{jets} > 0$	2.3×10^4	1.0×10^4

The final estimation of the fake rate has been evaluated by using a weighted average of the one and two leptons CRs.

The contribution from conversions is naturally included in this estimate. Another component that is expected to have an effect on the fake rate estimation is the heavy flavour content of the CR as compared to the SR. This has been taken into account by duplicating each CR and measuring for each of them two different fake rates: one without the b-jet requirement (to be used in the pre-tag scenarios) and one with the b-jet requirement (to be used for predictions in SR where b-jets are explicitly required).

To better model the fake contribution, f is parameterized as a function of different lepton quantities, such as η, $\mathrm{p_T}$ isolation ($\Delta R_{\ell j}^{min}$) as well as on global variables as $\sum E_T$.

Real efficiency

The real efficiency is extracted from a sample of highly purified Z boson events. This is achieved by requiring two opposite-sign loose leptons with same flavor whose invariant mass lies in the range 86-96 GeV. The real efficiency is then esti-

mated with a tag&probe method: one of the two leptons is required to pass tight criteria, the other one is then probed for tight selection cuts. The real efficiency is also measured as a function of η and p_{T} of the leptons, while other additional dependences are found to be negligible.

Signal Region predictions

The estimated SR fake contribution by applying the Matrix Method to the observed event yields is of -0.06±0.06(stat.)±0.02(syst.) events in the SF channel and 0.49±0.54(stat.)±0.06 (syst.) in the DF channel.

The number of events observed in the SR is very small and hence the background prediction has a large statistical uncertainty. Furthermore, the reduced yield could also suffer from severe signal contamination. To cope with this problems, the Matrix Method SR predictions have been validated with an additional approach based on the measurement of the fake background in suitable CRs and projection of the contribution in the SR by means of transfer factors.

In the SF channel, the number of events in the SR (N_{fakes}^{SRnoZ}) are estimated by means of the Matrix Method after dropping the explicit Z-veto requirement[2] (N_{fakes}^{SRZ}). The Z-veto cut efficiency is measured before the $\mathrm{m_{T2}}$ requirement and applied a posteriori as a scaling factor.

$$N_{fakes}^{SRnoZ} = N_{fakes}^{SRZ} \times \frac{N_{fakes}^{noZ}}{N_{fakes}^{Z}}, \tag{5.8}$$

The estimated number of fakes events in the SF SR becomes -0.20±0.11(stat.)±0.09(syst.)

The DF channel is treated with a similar technique: an extrapolation procedure has been implemented on the basis of $\mathrm{m_{T2}}$ and the $\mathrm{p_T}$ of the sub-leading jet. Four regions have been defined as follows:

- *A*: $m_{\mathrm{T2}} < 120$ GeV, $p_{\mathrm{T}}^{sub-lead\ jet} > 25$ GeV
- *B*: $m_{\mathrm{T2}} > 120$ GeV, $p_{\mathrm{T}}^{sub-lead\ jet} > 25$ GeV (corresponding to the SR)
- *C*: $m_{\mathrm{T2}} < 120$ GeV, $p_{\mathrm{T}}^{sub-lead\ jet} < 25$ GeV
- *D*: $m_{\mathrm{T2}} > 120$ GeV, $p_{\mathrm{T}}^{sub-lead\ jet} < 25$ GeV

[2] $m_{\ell\ell} < 76$ or $m_{\ell\ell} > 111$ GeV.

The number of fake events in the SR is predicted from the following equation:

$$N_{SR}^{QCD} = N_B = N_D \times \frac{N_A}{N_C}, \tag{5.9}$$

while the number of fake events in regions A,C and D is estimated using the Matrix Method, and is listed in table 5.12. The estimated number of fakes events in the DF SR is -0.08$\pm$0.08(stat.)$\pm$0.03(syst.).

Table 5.12: Number of estimated events with fake leptons in region A, C and D for the DF channel. The quoted errors are only statistical.

Region	**Fakes**
A	421.8$\pm$20.6
C	51.9$\pm$7.5
D	-0.01$\pm$0.01

The results obtained by projections into the SR are found compatible with the results given by the Matrix Method itself. However, since they are affected by smaller uncertainties, these will be used as baseline estimations for the fake background.

5.6 Systematic uncertainties

Various systematic uncertainties affecting the predicted background rates in the signal regions are considered. Such uncertainties are either used directly in the evaluation of the predicted background in the SR when this is derived by the pure MC prediction or to compute the uncertainty on the transfer factor and propagate it to the predicted event yields in the SR when the background is constrained from a CR, as described in Sections 5.5.1 and 5.5.2.

The most important instrumental uncertainties are the Jet Energy Scale, the Jet Energy Resolution and the uncertainty on $E_{\mathrm{T}}^{miss,CellOut}$. The b-tagging and the uncertainties on leptons are smaller by an order of magnitude.

In addition to these uncertainties also the statistical error coming from the limited MC statistics, which is often denoted as "stat.", has to be considered. Each source of systematics is handled following the ATLAS combined performance group recommendations.

The control region statistics is the leading uncertainty for the fake and Z+jets backgrounds. Among theoretical uncertainties, the generator and ISR/FSR are the most important systematics for the $t\bar{t}$ and diboson estimates. Luminosity and cross section uncertainties are relatively small.

In the following, a detailed description of how the various sources have been considered, is given.

5.6.1 Experimental systematics

The following experimental systematic uncertainties were found to be non-negligible:

- **Jet energy scale and resolution**. The uncertainty on the jet energy scale (JES), derived using single particle response and test beam data, varies as a function of the jet $\mathrm{p_T}$ and pseudorapidity η [101]. Additional systematic uncertainties arise from the dependence of the jet response on the number of interactions per bunch crossing and on the jet flavor. The components of the jet energy scale uncertainty are varied by $\pm 1\sigma$ in the MC simulation in order to obtain the resulting uncertainty in the event yield.

  Uncertainties related to the jet energy resolution (JER) are obtained with an in-situ measurement of the jet response asymmetry in di-jet events [102]. Their impact on the event yield is estimated by applying an additional smearing to the jet transverse momenta.

The JES and JER variations applied to the jet momenta are propagated to the $E_{\mathrm{T}}^{\mathrm{miss}}$.

- $E_{\mathrm{T}}^{miss,CellOut}$ **and pile-up**. The uncertainties related to the contribution to E_{T}^{miss} from the calorimeter cells not associated to reconstructed physics objetcs and also from low momentum (7 GeV $< p_T <$ 25 GeV) jets have been evaluated separately and added in quadrature.

  The uncertainty due to the modeling of pile-up is computed by rescaling the value of the average number μ of proton-proton interactions per bunch crossing used in the reweighting to match the μ profile observed in data by $\pm$10%, and comparing the results with the nominal sample which does not use any rescaling. The resulting systematic uncertainty is symmetrized.

- **b-tagging efficiency and mis-tagging**. This uncertainty is evaluated by varying the *b*-tagging efficiency and mis-tagging rates within the uncertainties measured in situ. This uncertainty only affects the SF channel and is relatively small (about 1% of the total event yield).

- **Lepton efficiency, energy scale and resolution** As discussed in Section 5.2, all selected leptons in a given MC event contribute with a multiplicative weight to the overall event weight in order to account for differences in efficiency with respect to data (including corrections for both identification and reconstruction efficiency). The impact of these uncertainties is taken into account by checking the variation of results obtained by using the nominal scale factors and the scale factors varied by the systematic uncertainty provided by the combined performance groups.

  The electron energy scale uncertainty is estimated by scaling up and down the energy and the momentum of all selected electrons by $\pm$3%, while the energy resolution uncertainty is quantified by comparing the nominal results and those obtained by imposing a smearing on electron energies according to a Gaussian with $\mathrm{p_T}$ and η dependent sigma.

  The uncertainties on muon momentum are estimated comparing the nominal results with the ones obtained by applying smearings on the individual MS and ID estimates of muon momentum.

5.6.2 Theoretical systematics

The following theoretical systematic uncertainties have been taken into account:

- $t\bar{t}$ **production generator**. The uncertainty associated to the choice of a specific MonteCarlo generator. This is evaluated comparing the predictions of MC@NLO, POWHEG (with two different hadronisation simulations) and ALPGEN samples.

- **ISR/FSR**. The uncertainty related to ISR and FSR in $t\bar{t}$ events is evaluated considering two dedicated ACERMC samples with varying settings, and taking half of the difference between these samples as systematic uncertainty.

- **Z+jets generator**. The predictions of the baseline ALPGEN generator are compared with those from SHERPA.

- **Diboson generator**. The baseline SHERPA sample is compared with ALPGEN to evaluate the uncertainty associated to the request of two jets, and with HERWIG to evaluate the uncertainty associated to the m_{T2} spectrum.

5.6.3 Other systematics

- **Luminosity**. The uncertainty on the luminosity [103] estimated for the whole dataset used in the analysis is taken to be 3.9%.

- **Cross section**. The uncertainty related to the cross section value is taken to be 5% for the Z/γ^*+jets boson production [104]. For $t\bar{t}$, the recommended value of $\sigma_{t\bar{t}} = 167^{+17}_{-18}$ pb is used for a top quark mass of 172.5 GeV as obtained from approximate NNLO QCD calculations [105]. The cross section uncertainties for WW, ZZ and WZ are 6%, 5% and 7% respectively [46, 63]. For single top, the cross section of 15.7 ± 1.2 pb is used for the Wt channel [47]. For $t\bar{t} + W$ a cross section of $0.168^{+0.023}_{-0.037}$ pb is used [64]. For $t\bar{t} + Z$ a cross section of 0.130 ± 0.019 pb is used [64]. A 25% uncertainty is considered on the W+jets in the fake rate estimate.

  The uncertainties for $t\bar{t}$and Z/γ^*+jets production cross section do not play any role in the background estimate because these processes are normalized to data in appropriate control regions, but they contribute to the uncertainty on the MC predictions shown in the figures. The uncertainty on single top, $t\bar{t} + Z$ and $t\bar{t} + W$ cross sections contribute to the background uncertainty in

the SR but they are negligible compared to other uncertainties, because of the small rates of these backgrounds in the SR.

- **Fake-lepton background**. An uncertainty of 33% (25%) is assigned to the fake background in the SF (DF) channel from the comparison of results of the fake rate measurement from different CRs. An additional 30% is taken as systematic uncertainty due to the extrapolation into the SR. The uncertainties on lepton ID measurement and on trigger modeling have been found to have a negligible impact on the analysis.

The breakdown of the main background uncertainties in individual sources is reported in Table 5.13. The largest uncertainties come from MC statistics and the $t\bar{t}$theory uncertainty. The total uncertainty is found to be about 40% (60%) for the SF (DF) channel.

Table 5.13: Breakdown of the dominant systematic uncertainties on background estimates in the two signal regions. The absolute uncertainty is given. Note that the individual uncertainties can be correlated, and do not necessarily add up quadratically to the total background uncertainty.

Signal Region	**SF**	**DF**
Total background uncertainty	$^{+0.60}_{-0.59}$	± 0.6
JES	± 0.04	± 0.2
JER	± 0.26	± 0.07
b-tagging	± 0.02	-
Cross sections & Luminosity	± 0.02	± 0.03
pileup	± 0.03	± 0.1
$E_{\mathrm{T}}^{miss,CellOut}$	± 0.12	± 0.21
$t\bar{t}$ modeling	± 0.20	± 0.44
Z/γ^*+jets modeling	± 0.12	± 0.0
MC statistics	± 0.42	± 0.19

5.7 Results

The number of events observed in the signal region for the two channels is reported in Table 5.14, and compared to the total expected background. The breakdown of the background in its individual components, together with the total uncertainties discussed in the previous section, is also reported.

Since the fake lepton estimate central value is negative, it has been set to zero to compute the total background, and the fake estimate uncertainty only contributes to the upwards error on the total background.

Good agreement is found between data and the expected SM background in both the same flavour and the different flavour channels.

Table 5.14: Observed and expected number of events in the signal region for the two channels of the analysis. The breakdown of the background in the individual components is also reported. The Z+jets contribution to DF is negligible. The expected yield for two signal models is also shown, with the associated uncertainties (theoretical and experimental).

	SF	**DF**
Observed	1	2
Expected	$1.58^{+0.63}_{-0.59}$	0.94 ± 0.60
$t\bar{t}$	$0.23^{+0.24}_{-0.23}$	$0.43^{+0.48}_{-0.43}$
$t\bar{t}+W$	0.06 ± 0.04	0.11 ± 0.08
$t\bar{t}+Z$	0.05 ± 0.04	0.08 ± 0.05
Wt	$0.00^{+0.19}_{-0.10}$	$0.10^{+0.19}_{-0.10}$
Z/γ^*+jets	1.17 ± 0.49	-
WW	$0.01^{+0.02}_{-0.01}$	0.19 ± 0.18
WZ	0.03 ± 0.03	0.03 ± 0.03
ZZ	0.02 ± 0.02	$0.00^{+0.03}_{-0.00}$
Fake leptons	$0.00^{+0.14}_{-0.00}$	$0.00^{+0.09}_{-0.00}$
$(m_{\tilde{t}_1}, m_{\tilde{\chi}^0_1})$ = (300, 50) GeV	2.2 ± 0.4	3.7 ± 0.7
(m_T, m_{A_0}) = (450,100) GeV	3.1 ± 0.5	5.8 ± 0.9

5.8 Interpretation and limit setting

The observed event yield in the SF and in DF channels (summarized in Table 5.14) is compared to the SM expectations using a frequentist significance test. We define a likelihood function $\mathcal{L}(n_s)$ as follows:

$$\mathcal{L}(n_s; \mu b, \theta) = Poiss(n_s|s(\mu, b, \theta)) \times N_{\text{syst}}(\theta_0, \theta) \tag{5.10}$$

where $Poiss(n_s)$ is a Poisson probability density function (pdf) describing the expected event counts n_s in each channel, given the expectation s. μ is the SUSY signal strength to be tested, b is the number of background events and θ describes the systematic uncertainties as nuisance parameters modeled by a Gaussian pdf. N_{syst} models the different systematic uncertainties described in Section 5.6: each parameter θ can be varied around the nominal values θ_0.

The signal prediction uncertainties include all the experimental uncertainties discussed there, together with cross section, luminosity, and finite MC statistics. The signal cross section uncertainty has been estimated from an envelope of cross section predictions, as described in Section 2.6.

The correlation between signal and background in the JES, the b-tagging and luminosity uncertainties are taken into account, while the other uncertainties which act independently on the signal and on the the background are summed up to define two groups of uncorrelated uncertainties.

The profile likelihood ratio is used as test statistic [106]. Distributions are obtained generating toys to take into account the statistic and systematic effects for the different signal strength hypotheses. The combined likelihood for the two independent channels in the analysis is defined as the product of the two separate likelihoods. Further information on the statistical techniques used to treat the data can be found in appendix A.

No excess of events in data is observed, and limits at 95% CL are derived on the visible cross section $\sigma_{\text{vis}} = \sigma \times \epsilon \times \mathcal{A}$, where σ is the total production cross section for the non-SM signal, $\mathcal{A}$ is the acceptance defined by the fraction of events passing the geometric and kinematic selections at particle level, and ϵ is the detector reconstruction, identification and trigger efficiency. These observed and expected limits are shown in Table 5.15. Only background uncertainties are considered for the model independent limits.

The results obtained are interpreted deriving limits on the mass of a pair-produced heavy top-quark partner decaying into a top quark and a weakly in-

Table 5.15: Observed and expected upper limits at 95% confidence level on $\sigma_{vis} = \sigma \times \epsilon \times \mathcal{A}$, and $\pm 1\sigma$ errors on the expected limits.

	SF	**DF**
σ_{vis}^{obs}[fb]	< 0.86	< 1.08
σ_{vis}^{exp}[fb]	$< 0.89^{+0.28}_{-0.18}$	$< 0.79^{+0.41}_{-0.09}$

teracting particle, assuming a 100% branching ratio. The limits are shown in the plane defined by the masses of the two particles for two scenarios: a model with a top squark $\tilde{t}_1$ and a spin-1/2 neutralino $\tilde{\chi}_1^0$ and one with a spin-1/2 top-quark partner T and a scalar boson A_0.

In both scenarios, the limits are derived after combining the SF and DF channels. No exclusion is either expected or observed in the SF channel alone because of the reduced acceptance, however some sensitivity can be recovered in the statistical combination with the more sensitive DF channel.

The limits are shown in figure 5.22 for the top squark and spin-1/2 top-quark partner models.

A top squark of mass close to 300 GeV and a nearly massless neutralino is excluded at 95% CL. The effect of signal uncertainties is significant, the excluded range for the nominal cross section being from 279 GeV to 348 GeV, and the expected exclusion from 258 GeV to 374 GeV. This is in part due to the fact that near the maximum of the sensitivity, the p-value varies relatively little with the mass, so that a small variation in the cross section results in a large variation of the limit.

The region of the mass plane which is excluded for a spin-1/2 top-quark partner production is instead larger, thanks to the larger expected production cross section. A spin-1/2 top-quark partner with a mass between 300 GeV and 480 GeV (if the A_0 mass is lower than 100 GeV) is excluded at 95% CL. The established limit improves significantly the previous limit of 420 GeV established by ATLAS with 1 fb^{-1} in the single lepton channel [107].

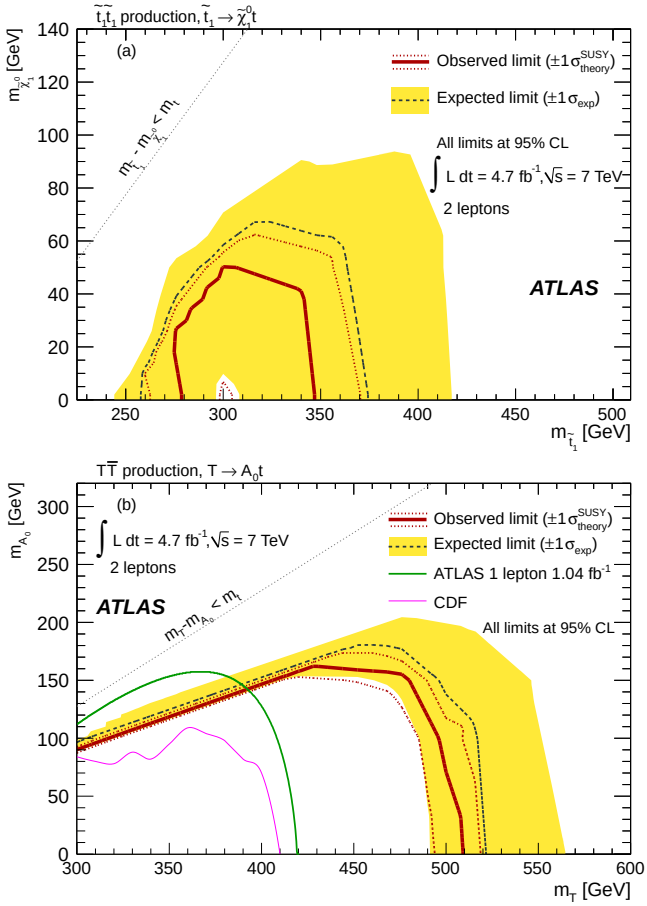

Figure 5.22: Expected and observed 95% CL limits (a) in the $\tilde{t}_1 \to t\tilde{\chi}_1^0$ model as a function of the top squark and neutralino masses, and (b) in the $T \to tA_0$ model as a function of the spin-1/2 top-quark partner T and A_0 masses. The dashed line and the shaded band are the expected limit and its $\pm 1\sigma$ uncertainty, respectively. The thick solid line is the observed limit for the central value of the signal cross section. The dotted lines show the effect on the observed limit of varying the signal cross section by $\pm 1\sigma$ of the theoretical uncertainty.

CHAPTER 6

Search for top squarks decaying to a chargino and a bottom quark

ln the following chapter a search for top squarks decaying in the $b + \tilde{\chi}_1^{\pm}$ final state will be presented. This analysis uses all the data collected by ATLAS during the 2012 run at $\sqrt{s} = 8$ TeV and shares with the analysis presented in Chapter 5 the background estimation strategy and the main discriminating variable, the stransverse mass.

6.1 Introduction

The analysis of 2011 data by the searches for third generation squarks at ATLAS covered a wide range of production and decay mechanisms. Both the direct and gluino mediated production of scalar bottom and scalar top quarks had been studied. Table 6.1 gives an overview of the scenarios investigated by the ATLAS collaboration.

In all the cases, no significant excess from the SM expectations has been observed and exclusion limits have been set in different areas of parameter space.

In particular, five different analyses depending on the top squark decay mode and on the number of isolated leptons in the decay chain have been carried out and limits on $m_{\tilde{t}_1}$ and $m_{\tilde{\chi}_1^0}$ have been derived as summarized in figure 6.1.

The search for top squark production in final states with two leptons targeting the decay to a top quark and a neutralino above the limits established by the 7 TeV searches is severely limited. The expected $\sim 50\%$ increase in the top squark pair production cross-section with respect to the 7 TeV values is not sufficient to compensate the sensitivity loss due to the rapidly decreasing expected cross-sections

Channel	Final state	Luminosity	Ref.
gluino-mediation	4-6 jets + 3 b-tags + E_T^{miss}	4.7 fb^{-1} (7 TeV) and 12.8 fb^{-1} (8 TeV)	[108, 109]
gluino-mediation	3 leptons + $\geq$ 4 jets + E_T^{miss}	13.0 fb^{-1} (8 TeV)	[110]
$\tilde{t}_1 \to b + \tilde{\chi}_1^{\pm}$	2-lep + E_T^{miss}	4.7 fb^{-1} (7 TeV)	[111]
$\tilde{t}_1 \to b + \tilde{\chi}_1^{\pm}$	1/2-lep + b-jet + E_T^{miss}	4.7 fb^{-1} (7 TeV)	[112]
$\tilde{t}_1 \to t + \tilde{\chi}_1^0$	0-lep + b-jet + E_T^{miss}	4.7 fb^{-1} (7 TeV)	[113]
$\tilde{t}_1 \to t + \tilde{\chi}_1^0$	1-lep + b-jet + E_T^{miss}	4.7 fb^{-1} (7 TeV)	[114]
$\tilde{t}_1 \to t + \tilde{\chi}_1^0$	2-lep + b-jet + E_T^{miss}	4.7 fb^{-1} (7 TeV)	[2]
$\tilde{b}_1 \to b + \tilde{\chi}_1^0$	0-lep + 2 b-jet + E_T^{miss}	2.05 fb^{-1} (7 TeV) and 12.8 fb^{-1} (8 TeV)	[115, 116]
Natural GMSB	Z + b-jet + E_T^{miss}	2.05 fb^{-1} (7 TeV)	[117]

Table 6.1: Overview over searches for third generation squarks at ATLAS performed at the time of the analysis design.

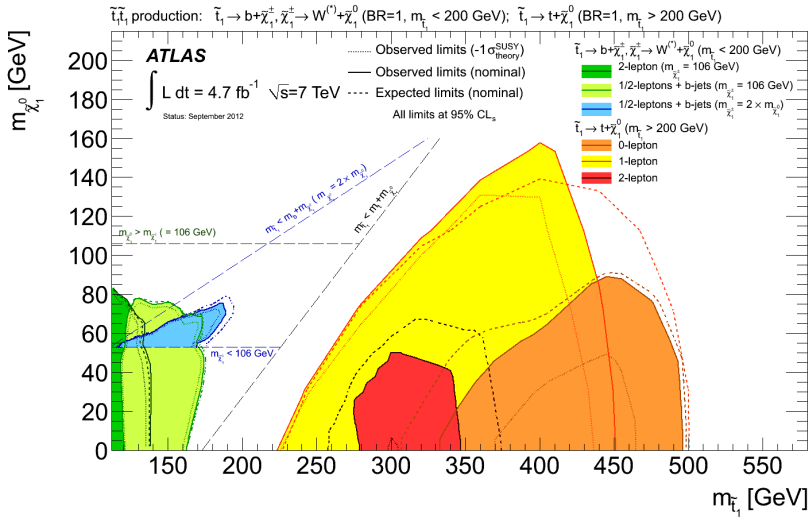

Figure 6.1: Summary of the five dedicated ATLAS searches for scalar top quark pair production based on 4.7 fb^{-1} of proton-proton collision data taken at $\sqrt{s} = 7$ TeV [111, 112, 113, 114, 2]

of more massive signals, combined with the reduced branching ratio of the dileptonic final state.

However, the dileptonic final state can still be exploited to set limits on the decay either through a real chargino, if $m(\tilde{t}_1) - m(b) > m(\tilde{\chi}_1^{\pm})$,

$$\tilde{t}_1\tilde{t}_1 \to \tilde{\chi}_1^{\pm} b \;\; \tilde{\chi}_1^{\mp}\bar{b} \to \tilde{\chi}_1^0 b l^+ \nu \;\; \tilde{\chi}_1^0 \bar{b} l^- \nu \tag{6.1}$$

or directly with a 3-body decay, if $m(\tilde{t}_1) - m(b) < m(\tilde{\chi}_1^{\pm})$ (off-shell chargino) or if

$m(\tilde{t}_1) - m(\tilde{\chi}_1^0) < m(t)$ (off-shell top)

$$\tilde{t}_1\tilde{t}_1 \to bW^+\tilde{\chi}_1^0 \;\; bW^-\tilde{\chi}_1^0 \to bl^+\nu\tilde{\chi}_1^0 \;\; \bar{b}l^-\nu\tilde{\chi}_1^0. \tag{6.2}$$

where $\tilde{t}_1$ is the supersymmetric top squark, $\tilde{\chi}_1^\pm$ are the lightest charginos and $\tilde{\chi}_1^0$ is the lightest neutralino, which is supposed to be the LSP. The second process requires also that $m(\tilde{t}_1) > m(b) + m_W + m(\tilde{\chi}_1^0)$.

The signature considered is the same as in the analysis presented in Chapter 5: it contains two b-jets, two W bosons, real or virtual, and two invisible particles.

The main difference with respect to the analysis presented in the previous chapter is that the kinematics of the final state particles can change significantly, depending on the mass spectrum of the supersymmetric particles involved in the decay. In particular, in the case of small mass splittings between the $\tilde{t}_1$ and the $\tilde{\chi}_1^\pm$, the b-jets are expected to be very soft. This leads to very small hadronic activity in the detector. In order to retain sensitivity to this kind of scenario, a selection without explicit cuts on the presence of jets has been studied.

The main irreducible backgrounds come from $t\bar{t}$ and diboson production. Two main criteria are used to separate the signal from the background: a set of angular cuts with respect to the E_{T}^{miss} direction and a selection on m_{T2} computed from the two leptons momenta and E_{T}^{miss} (see Section 5.1.1). For signal models including the decay shown in Eq.6.1, it is bounded by $\sqrt{m^2(\tilde{\chi}_1^\pm) - m^2(\tilde{\chi}_1^0)}$. By selecting events with large values of m_{T2}, the analysis is thus sensitive to models with $m^2(\tilde{\chi}_1^\pm) - m^2(\tilde{\chi}_1^0) > m_W^2$.

6.2 Trigger selection and object definition

Events are selected using a combination of single and di-lepton triggers: a set of different p_T thresholds has been used to achieve a flat efficiency for electrons and muons with $p_T > 25$ GeV. This choice is motivated by the decision to maximize the analysis acceptance: the use of the double lepton triggers recovers additional efficiency for the signal candidates.

The MC trigger efficiency has been tested on both a signal and the main background samples and found to be 99.5% in the electron channel and $\sim$ 95% in the muon channel. To check if the latter value well reproduces the efficiency in data, a trigger scale factor has been computed using the same techniques described in section 3.2. The scale factor is measured in the muon channel for the logical OR of the single muon triggers; the additional requirement of the dileptonic triggers is not taken into consideration in the scale factor measurement since 95% of the muon events are delivered by these single lepton triggers. A constant negative 3% effect has been observed on the number of events if the scale factor is applied. Since the effect is small, an overall systematic of 3% is considered for the muon trigger efficiency, but no scale factor is applied throughout the analysis.

- *Proton-proton interaction vertex* is selected as in Section 5.2.

- *Jets* are reconstructed using the anti-k_t jet algorithm with the distance parameter R set to 0.4 and topological clusters as input. The jets are calibrated with the LCW+JES scheme (see section 4.3). They are kept only if they have $p_T > 20$ GeV and lie within $|\eta| < 2.5$. An additional cut on the JVF is required to suppress pile-up jets, asking for JVF > 0.5 for jets with p_T¡ 50 GeV and $|\eta| < 2.4$. The choice of the value of the cut is motivated by the different shapes of the distributions for pile-up and hard-scatter jets, shown in figure 6.2 (left), with the ATLAS recommended cut at 0.5 being found optimal for the analysis. The JVF requirement is applied only to jets within $|\eta| < 2.4$ in order to avoid rejecting hard-scatter jets with their core located outside the ID acceptance. This is shown by the blue line in figure 6.2 (right), representing the number of calorimeter jets which do not have associated tracks. Finally the upper cut on the jet $p_T$is motivated by the fact that the jet multiplicity distribution for jets with $p_T > 50$ GeV has been found independent of pile-up even before the JVF cut, as shown in figure 6.3.

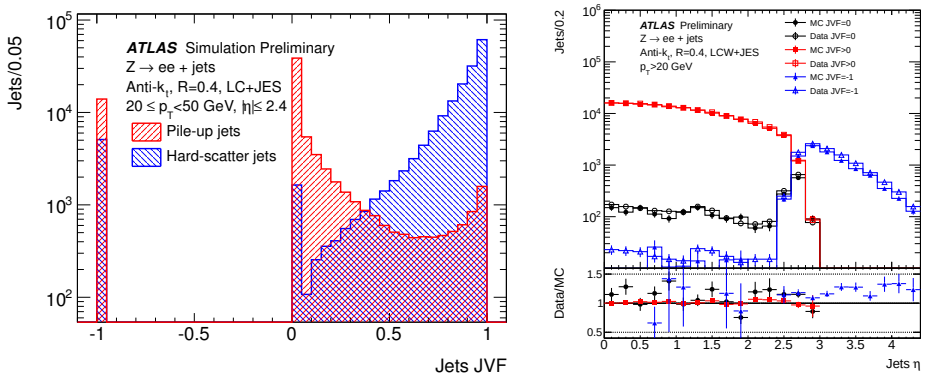

Figure 6.2: Left: JVF distribution for hard-scatter (blue) and pile-up (red) jets with $20 \leq p_{\mathrm{T}} \leq 50$ GeV in simulated Z+jets events. Using JVF directly as a discriminating variable provides a way to separate both classes of jets.
Right: jet η distribution for pure pile-up jets (black), jets with tracks coming from the hard scatter (red) and calorimeter jets which do not have associated tracks (blue) in Z+jet events. [118]

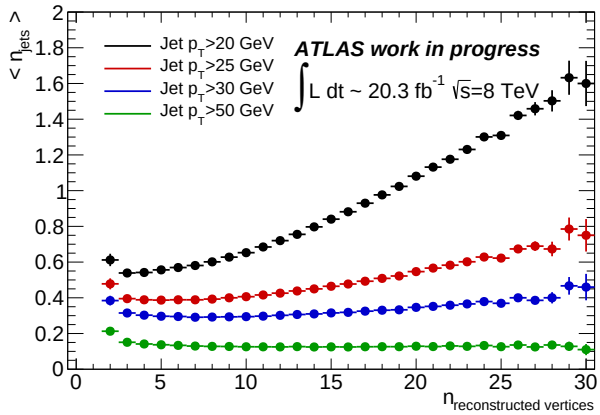

Figure 6.3: Distribution of the average number of jets per event as a function of the average number of reconstructed vertices, without applying any JVF cut. The distributions for jets with $p_{\mathrm{T}} > 50$ GeV are independent on pile-up.

- *Electron* candidates are required to have $p_{\mathrm{T}} > 10$ GeV, $|\eta| < 2.47$ and to satisfy "medium" electromagnetic shower shape and track selection quality criteria described in section 4.4. These preselected electrons are then required to pass "tight" quality criteria which places additional requirements

on the ratio of calorimetric energy to track momentum, and on the fraction of hits in the straw tube tracker that pass a higher threshold for transition radiation. The electron candidates are then required to be isolated: the scalar sum of the p_T, $\sum p_T$, of inner detector tracks, not including the electron track, with $p_{\mathrm{T}} > 1$ GeV within a cone in the $\eta - \phi$ plane of radius $\Delta R = \sqrt{\Delta\eta^2 + \Delta\phi^2} = 0.2$ around the electron candidate must be less than 10% of the electron p_T. In MC a multiplicative event weight is applied for each selected electron to the overall event weight in order to correct for differences in efficiency between data and MC.

- *Muon* candidates are reconstructed using either a full muon spectrometer track matched to an inner detector track, or a muon spectrometer segment matched to an extrapolated inner detector track. They must be reconstructed with more than one hit in the pixels, more than five hits in both the strips and straw tube detectors. They are required to have $p_{\mathrm{T}} > 10$ GeV, $|\eta| < 2.4$ and must have longitudinal and transverse impact parameters within 1 mm and 0.2 mm of the primary vertex, respectively.

  Muon candidates have been also required to be isolated. The $\sum p_{\mathrm{T}}$ of the tracks in a cone of $\Delta R < 0.2$ must be less than 1.8 GeV (excluding the muon track).

- The *missing transverse energy* calculation uses calorimeter cells with $|\eta| < 4.9$ and the muons from the STACO container. The cells are calibrated according to the object they belong to. The objects considered are the jets calibrated with the LCW+JES scheme for $p_{\mathrm{T}} > 20$ GeV and with the LCW scheme for 10 GeV $< p_{\mathrm{T}} <$ 20 GeV, and "medium" electrons with $p_{\mathrm{T}} > 10$ GeV. Cells not belonging to any of the object above are again calibrated at the EM scale.

Following the object reconstruction described above, overlaps between jet, electron and muon candidates are resolved. Any jet within $\Delta R = 0.2$ of preselected electrons is discarded. Electrons or muons within $\Delta R = 0.4$ of any remaining jet are then discarded to reject leptons from the decay of a *b*- or *c*-hadron.

6.3 Event selection

Only the differences with respect to the event selection described in Section 5.3 will be highlighted here.

Events which contain exactly two opposite-sign leptons (electrons or muons) are selected if at least one lepton satisfies the leading p_{T} requirement of $p_{\mathrm{T}} > 25$ GeV in order to be in the trigger efficiency plateau.

In order to reduce high m_{T2} backgrounds where the value of E_T^{miss}, and hence of m_{T2} is increased by a mismeasurement of the hadronic part of the event, two angular cuts are applied: $\Delta\phi_b < 1.5$ and $\Delta\phi_{\mathrm{min}} > 1$.

The variable $\Delta\phi_b$ is the azimuthal angle between the E_T^{miss} vector and the $\vec{p}_{\mathrm{Tb}}^{\,ll} = \vec{E}_T^{\,\mathrm{miss}} + \vec{p}_T(l_1) + \vec{p}_T(l_2)$ vector, where the $\vec{p}_{\mathrm{Tb}}^{\,ll}$ variable, introduced in [119], is the opposite of the vector sum of all the hadronic activity in the event. For WW and $t\bar{t}$ backgrounds it measures the transverse boost of the WW system, and for the signal the transverse boost of the chargino-chargino system.

The $\Delta\phi_{\mathrm{min}}$ variable is the azimuthal angle difference between the E_T^{miss} vector and the closest jet, where the jets used are those passing the selection described in section 6.2.

These cuts suppresses the Z+jets background to negligible levels in the SF channel, and they also select the signal with larger efficiency than the dominant WW and top pair backgrounds.

Finally, signal candidates are required to have m_{T2} values in excess of 90 GeV. Alternative signal regions with tighter selections shown in table 6.2 are also used to increase the sensitivity to specific families of signal models with different mass hierarchies for the particles involved in the decay: in particular this involves applying selections on the hadronic activity of the event if a large $\Delta m(\tilde{t}_1, \tilde{\chi}_1^{\pm})$ is expected.

6.3.1 Event selection optimization

As previously explained, the analysis strategy is based on the selection of events with two leptons and a value of $\mathrm{m_{T2}}$ larger than the W mass.

As discussed in section 5.3.1, the distribution of $\mathrm{m_{T2}}$ after requiring only the trigger and the presence of two isolated leptons has still a significant tail of SM processes. For the DF channel the dominant background at high $\mathrm{m_{T2}}$ is $t\bar{t}$, followed by WW. The WW presents a longer tail populated by events where one the

Table 6.2: Signal regions used in the analysis. The last two rows of the table show the SUSY mass hierarchies that are targeted by each SR.

SR	**L90**	**L100**	**L110**	**L120**
p_{T} leading lepton [GeV]		> 25		
$\Delta\phi_{min}$ [rad]		> 1.0		
$\Delta\phi_b$ [rad]		< 1.5		
m_{T2} [GeV]	> 90	> 100	> 110	> 120
p_{T} leading jet [GeV]	-	> 100	> 20	-
p_{T} second jet [GeV]	-	> 50	> 20	-
$\Delta m(\tilde{t}_1, \tilde{\chi}_1^{\pm})$	small	large	small	small
$\Delta m(\tilde{\chi}_1^{\pm}, \tilde{\chi}_1^0)$	moderate	large	moderate	large

W is produced off-shell with a mass much higher than the W nominal mass. For the SF background, even after vetoing invariant masses in the Z region a long tail is observed, requiring additional cuts to separate the signal from the background.

A simple requirement on $\mathrm{m_{T2}}$ would already ensure sensitivity over a significant fraction of the parameter space in the DF channel. The main possibilities for extending the region of sensitivity of the analysis are:

- to extend the reach to as high as possible masses by reducing the high tail of the $\mathrm{m_{T2}}$ distribution
- to extend the reach to as low as possible chargino-neutralino mass differences. In order to achieve this, the kinematic boundary of the $\mathrm{m_{T2}}$ distribution for backgrounds must be sharpened. This approach will be relevant for the lower masses considered, 180 and 240 GeV, which is a crucial region not well covered by previous analyses.

The $\mathrm{m_{T2}}$ tail from top events is dominated by events where the $E_{\mathrm{T}}^{\mathrm{miss}}$ is increased by experimental effects. Similarly, for Z events, the high $\mathrm{m_{T2}}$ tails are from high $E_{\mathrm{T}}^{\mathrm{miss}}$ events produced by experimental effects. The additional $E_{\mathrm{T}}^{\mathrm{miss}}$ will point towards the hadronic jets which get mismeasured and away from the vector sum of the leptonic activity in the event. Two variables, $\Delta\phi_b$ and $\Delta\phi_{min}$, were already introduced in section 6.3 for this purpose.

The scatter plots of these two variables are shown for $t\bar{t}$ and Z events with

$m_{T2} > 90$ GeV in figure 6.4. The E_T^{miss} alignment is very clear for Z, where all of the E_T^{miss} is from instrumental effects, less clear for $t\bar{t}$ into two leptons which has a significant E_T^{miss} coming from the neutrinos. For the signal, as shown in figure 6.5, the upper left corner is populated.

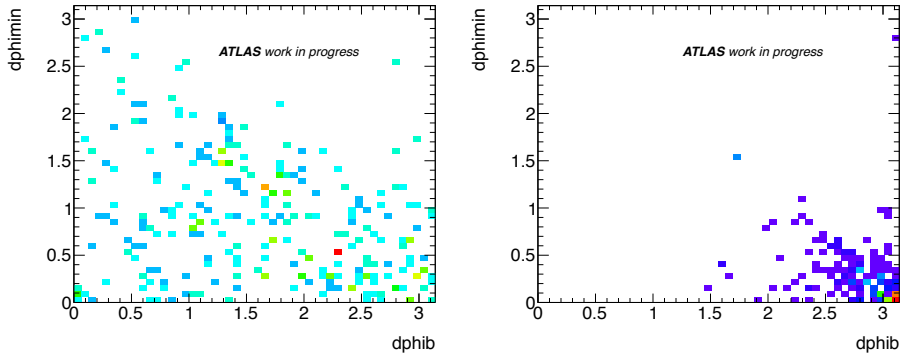

(a) $t\bar{t}$ (b) Z

Figure 6.4: Distribution of the $\Delta\phi_{\min}$ vs $\Delta\phi_b$ for events with $m_{T2} > 90$ GeV in $t\bar{t}$ (left) and Z/γ^* (right) samples.

The selections on $\Delta\phi_b$ and $\Delta\phi_{\min}$ were optimized over the full signal grid finding $\Delta\phi_b < 1.5$ and $\Delta\phi_{\min} > 1$ to be the optimal cuts. The distributions of m_{T2} after the cuts on the $\Delta\phi$ variables can be found in figure 5.18. The tail is dominated by $t\bar{t}$ up to 100 GeV, and for higher values by WW.

Signal candidates thus selected are required to have m_{T2} values in excess of at least 90 GeV (100 GeV, 110 GeV, 120 GeV).

A scan on the p_T selection on the two leading jets has been performed for each m_{T2} cut and four signal regions have been chosen with optimal sensitivity to different regions of parameter space. The optimization has been done using the expected CLs as figure of merit. In particular, moderate cuts on the jets p_T(L110) are chosen for points with moderate values of $\Delta m(\tilde{t}_1, \tilde{\chi}_1^{\pm})$. Tighter cuts (L100) are used for regions with large $\Delta m(\tilde{t}_1, \tilde{\chi}_1^{\pm})$. The tightest cut on m_{T2} (L120) was found to be useful for points with very large $\Delta m(\tilde{\chi}_1^{\pm}, \tilde{\chi}_1^0)$.

The 3-body decay scenario has been studied looking at the kinematic distribution of many different kinematic variables including m_{eff} (defined as the scalar sum of the lepton transverse momenta, E_T^{miss} and the first two jet transverse momenta), $m_{\ell\ell jj}$ and $\Delta\phi(\ell_1, \ell_2)$. The effect of changing the value of the angular se-

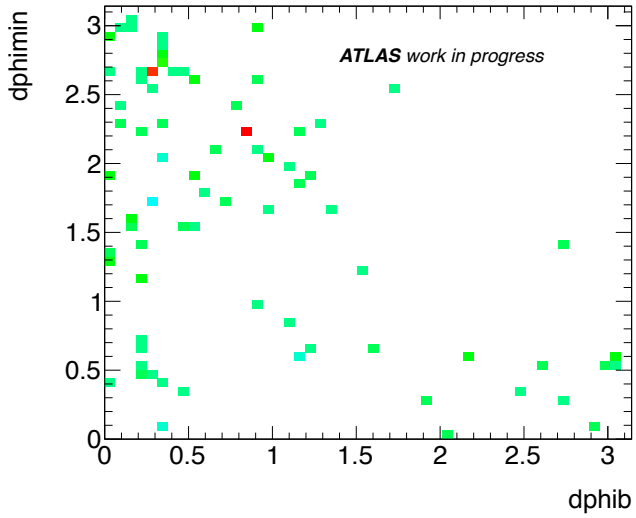

Figure 6.5: Distribution of the $\Delta\phi_{\min}$ vs $\Delta\phi_b$ variable for events with $m_{\mathrm{T2}} > 90$ GeV in the case of a signal model with $m(\tilde{t}) = 180$ GeV, $m(\tilde{\chi}^{\pm}) = 160$ GeV, $m(\tilde{\chi}^0) = 60$ GeV.

lections, applying a jet veto and varying m_{T2} cuts has also been investigated. The most sensitive variable appeared to be m_{eff} (shown in figure 6.6 in the case of a selection corresponding to SR L90): two signal regions were built using this variable (asking $m_{eff} < 250$ GeV and $m_{eff} > 250$ GeV on top of the SR L90 selection) and statistically combined. However, no significant gain in sensitivity has been observed with respect to the statistical combination of the remaining SRs (L90 to L120) optimized for the two body decay and the choice of using the m_{eff} variable was then abandoned.

The expected background and signal rates after all selections are reported in Table 6.3.

A summary of the SR selection criteria is reported in table 6.2.
Table 6.4 shows the amount of events passing these cuts in data, using the full analyzed data sample.

Table 6.3: Expected rates for the main background processes, for the four signal regions used in the analysis. All the predictions are taken from MC simulation, except for the fake leptons background which is from the data-driven estimate) For two signal points, the expected rate and expected CLs are also reported.

channel	**L90**	**L100**	**L110**	**L120**
Total background events	304.19 ± 50.11	5.43 ± 2.48	9.10 ± 3.71	17.45 ± 7.59
Expected $t\bar{t}$ events	189.78 ± 40.49	3.90 ± 2.39	3.73 ± 3.23	$1.16^{+1.20}_{-1.16}$
Expected WW events	61.50 ± 8.53	0.75 ± 0.38	2.56 ± 0.98	9.10 ± 4.98
Expected WZ events	5.53 ± 0.91	$0.10^{+0.19}_{-0.10}$	0.42 ± 0.31	1.38 ± 1.18
Expected ZZ events	8.07 ± 1.59	0.16 ± 0.12	0.66 ± 0.34	3.46 ± 1.26
Expected $Z/\gamma^* \to \ell\ell$ events	2.79 ± 1.44	$0.14^{+0.14}_{-0.14}$	$0.09^{+0.14}_{-0.09}$	$0.07^{+0.09}_{-0.07}$
Expected $t\bar{t}$+V events	1.83 ± 0.59	0.35 ± 0.14	0.62 ± 0.21	0.51 ± 0.18
Expected Wt events	21.05 ± 6.77	$0.00^{+0.19}_{-0.00}$	0.00 ± 0.00	$0.35^{+0.39}_{-0.35}$
Expected tZ events	0.04 ± 0.02	0.00 ± 0.00	0.01 ± 0.01	0.01 ± 0.01
Expected *Higgs* events	0.65 ± 0.22	$0.02^{+0.02}_{-0.02}$	0.03 ± 0.03	0.31 ± 0.12
Events with fakes leptons	12.95 ± 3.45	0.00 ± 0.00	0.98 ± 0.64	1.10 ± 0.83
m($\tilde{t}_1, \tilde{\chi}_1^\pm, \tilde{\chi}_1^0$) = (400,250,1) GeV	11.75	4.12	6.25	4.85
Expected CLs	0.68	0.02	0.03	0.33
m($\tilde{t}_1, \tilde{\chi}_1^\pm, \tilde{\chi}_1^0$) = (150,120,1) GeV	337.82	0.00	6.81	7.95
Expected CLs	0.00	0.81	0.44	0.98

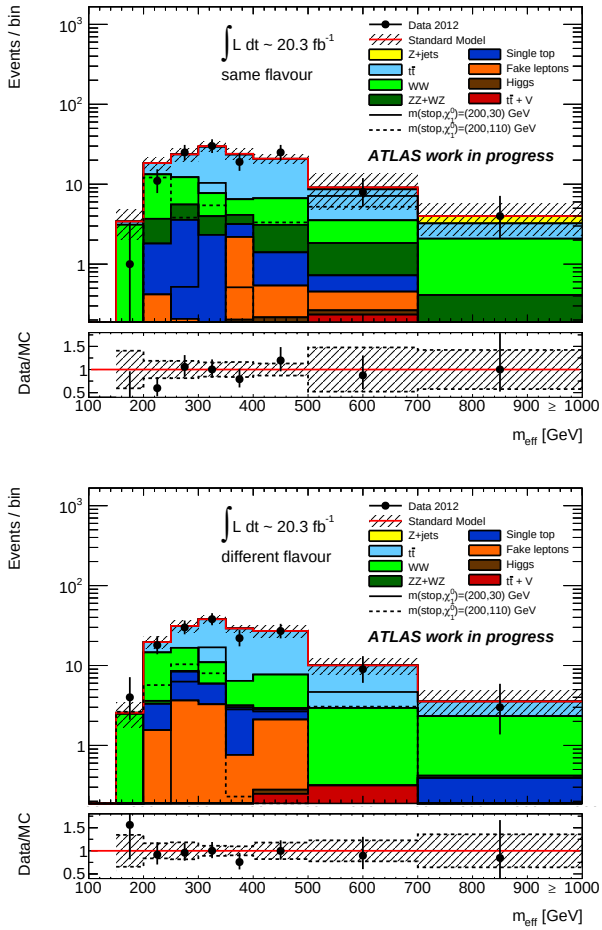

Figure 6.6: Distribution of the m_{eff} for events with two isolated leptons passing SR L90 cuts. The plots report the distribution for same flavour (top) and different flavour (bottom) lepton pairs respectively.

Table 6.4: Number of events passing cuts at various cutflow stages for data. The Z veto selection is applied only for the same flavor channels.

Cut	$e^{\pm}e^{\mp}$	$\mu^{\pm}\mu^{\mp}$	$e^{\pm}\mu^{\mp}$
Two Leptons	6416941	9393857	187482
Z Veto	581129	865870	-
$\Delta\phi_{min} > 1$	483934	711893	142230
$\Delta\phi_b < 1.5$	419804	610342	124315
L90	43	80	151
L100	1	1	1
L110	2	5	1
L120	4	5	9

6.4 Kinematic distributions

In this section, a comparison is made between data and MC simulation for the main observables used in the analysis. In all plots, the minor MC backgrounds use the nominal cross sections, while the major backgrounds ($t\bar{t}$, WW and $WZ + ZZ$) are normalized using the scale factors from CR measurements described in Section 6.5. The uncertainty band includes the MC statistics, the main detector response uncertainties (JES, JER, and E_T^{miss} cellout term), the cross section uncertainty, the generator and ISR/FSR uncertainties for $t\bar{t}$. The distributions are also shown separately the same and different flavor channels. The overall agreement between data and Monte Carlo is good.

Figures 6.7, 6.8, 6.9, 6.10 and 6.15 show the distributions of the p_T of the leading lepton, the p_T of the sub-leading lepton, the p_T of the leading jet, the p_T of the sub-leading jet and of the transverse missing energy respectively, after all selection cuts but for m_{T2}.

The jet multiplicity and p_{Tb}^{ll} variable distributions are shown respectively in figures 6.12 and 6.11 for the same selection level. The discrepancy between the nominal background prediction and the data at large jet multiplicities is mainly due to the poor performance of MC@NLO in describing these kinematic regions. However, the discrepancy is covered by the uncertainty computed from the generator comparison with POWHEG and doesn't have any significant impact on the analysis, since this region corresponds to a negligible fraction of the total events.

The two angular variables $\Delta\phi_{\text{min}}$ and $\Delta\phi_b$, are shown after applying all SR L90 selection cuts, except for the one the shown variable itself in figures 6.13, 6.14, respectively. These figures show clearly how the angular selections have an higher efficiency for signal than for the main SM backgrounds.

The effectiveness of the Z veto applied on SF events can be appreciated from the invariant mass distribution of the two leptons, shown in Figures 6.16 for events passing the trigger requirements and the selection of 2 isolated leptons.

The m_{T2} distribution for the different SRs are shown in figures 6.17, 6.18 and 6.19 after all selection cuts but for m_{T2} itself.

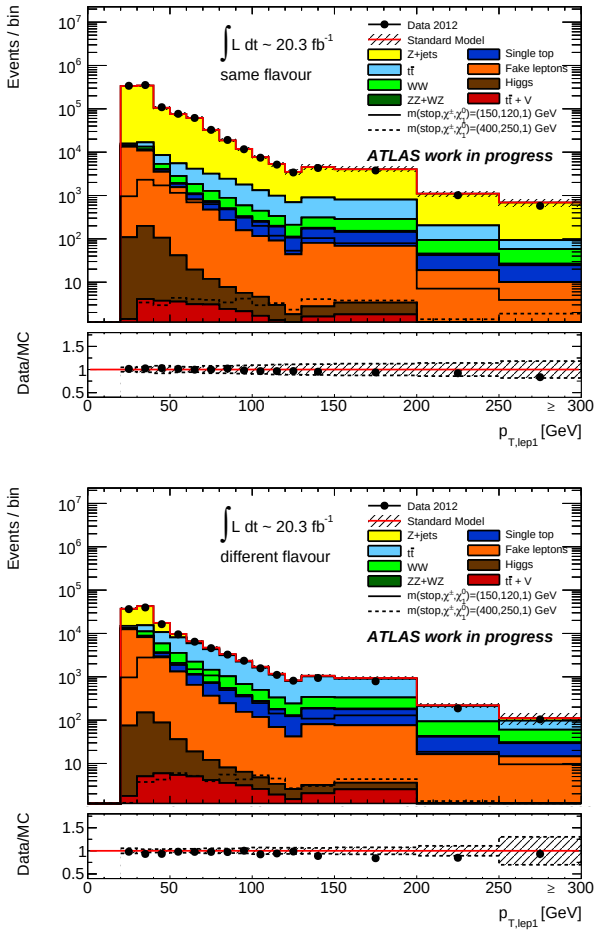

Figure 6.7: p_T distribution for the leading lepton in events passing all the signal candidate selection requirements, except that on m_{T2}, for same-flavour events (top) and different-flavour events (bottom). The contributions from all SM backgrounds are shown, with the bands representing the total uncertainty. The distributions for two different expected signal models are also shown.

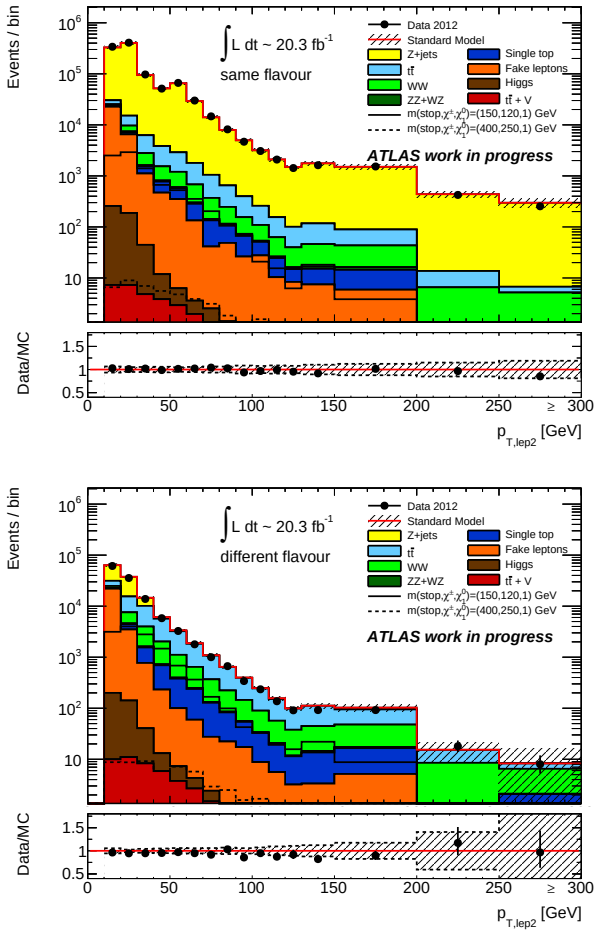

Figure 6.8: p_T distribution for the sub-leading lepton in events passing all the signal candidate selection requirements, except that on m_{T2}, for same-flavour events (top) and different-flavour events (bottom). The contributions from all SM backgrounds are shown, with the bands representing the total uncertainty. The distributions for two different expected signal models are also shown.

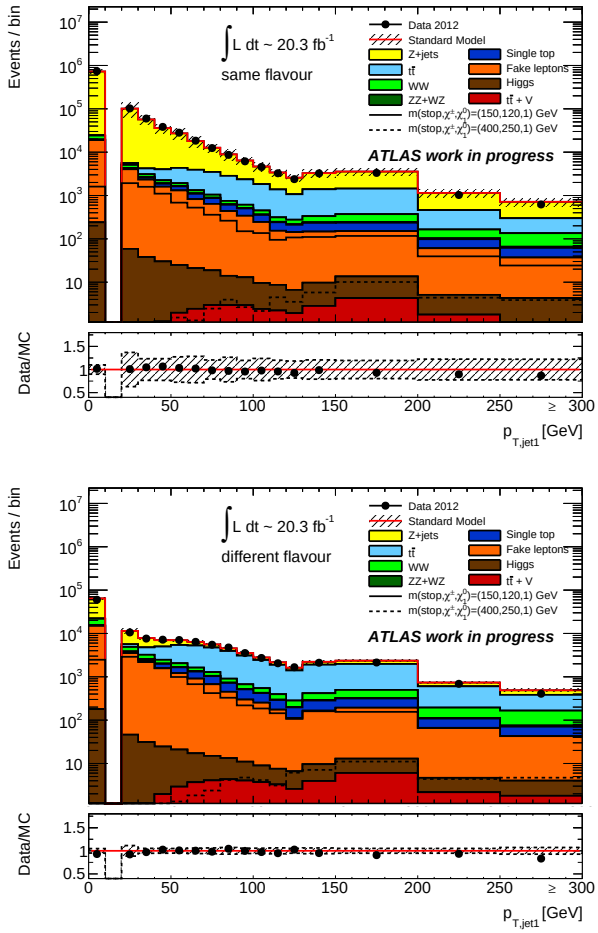

Figure 6.9: p_T distribution for the leading jet in events passing all the signal candidate selection requirements, except that on m_{T2}, for same-flavour events (top) and different-flavour events (bottom). The contributions from all SM backgrounds are shown, with the bands representing the total uncertainty. The distributions for two different expected signal models are also shown.

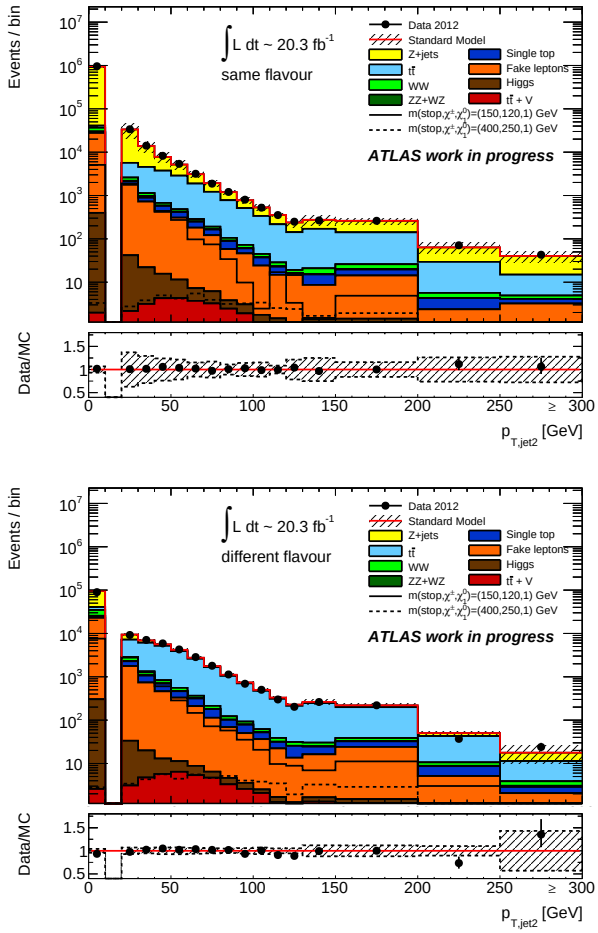

Figure 6.10: p_T distribution for the sub-leading jet in events passing all the signal candidate selection requirements, except that on m_{T2}, for same-flavour events (top) and different-flavour events (bottom). The contributions from all SM backgrounds are shown, with the bands representing the total uncertainty. The distributions for two different expected signal models are also shown.

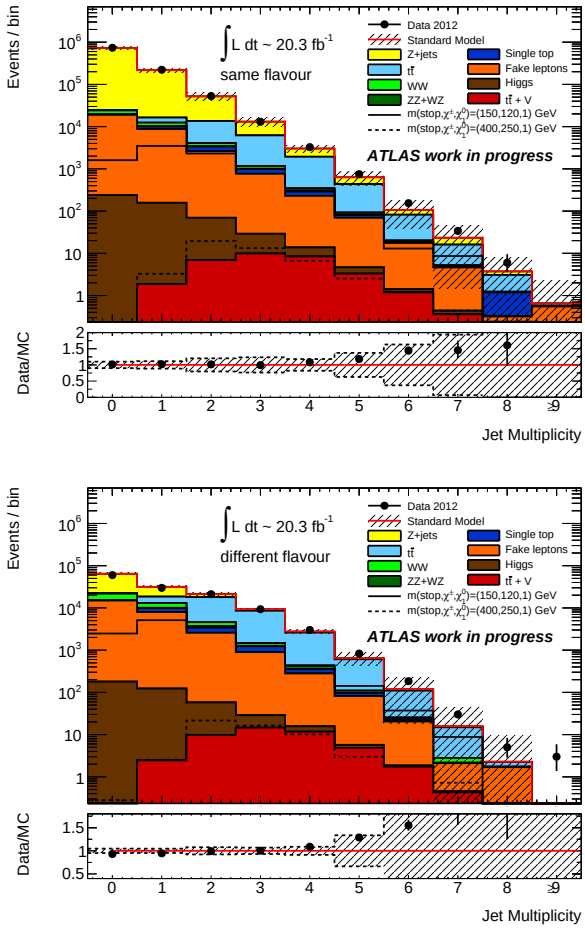

Figure 6.11: Jet multiplicity distribution in events passing all the signal candidate selection requirements for SR L90, except that on m_{T2}, for same-flavour events (top) and different-flavour events (bottom). The contributions from all SM backgrounds are shown, with the bands representing the total uncertainty. The distributions for two different expected signal models are also shown.

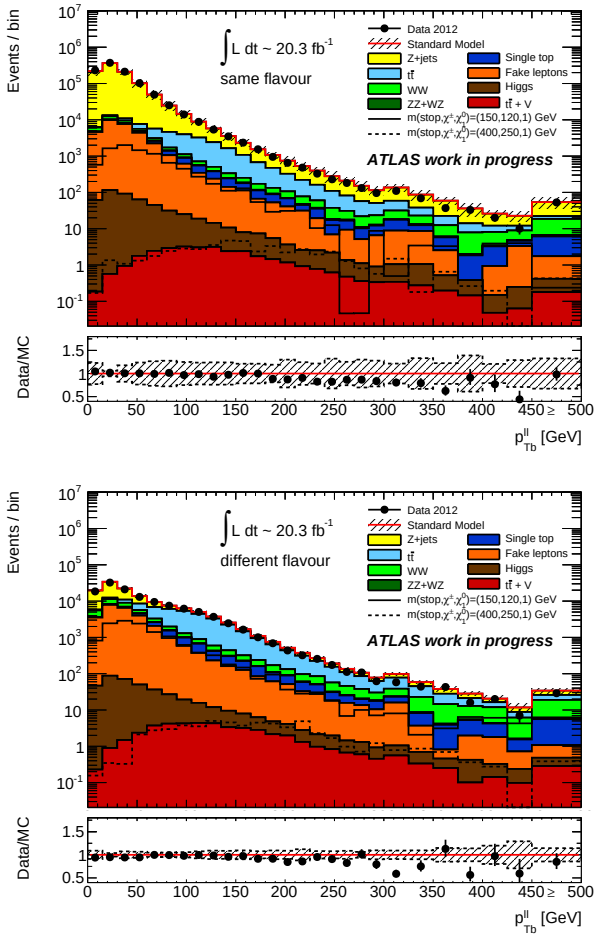

Figure 6.12: Distribution of the p_{Tb}^{ll} variable, in events passing all the signal candidate selection requirements, except that on m_{T2}, for same-flavour events (top) and different-flavour events (bottom). The contributions from all SM backgrounds are shown, with the bands representing the total uncertainty. The distributions for two different expected signal models are also shown.

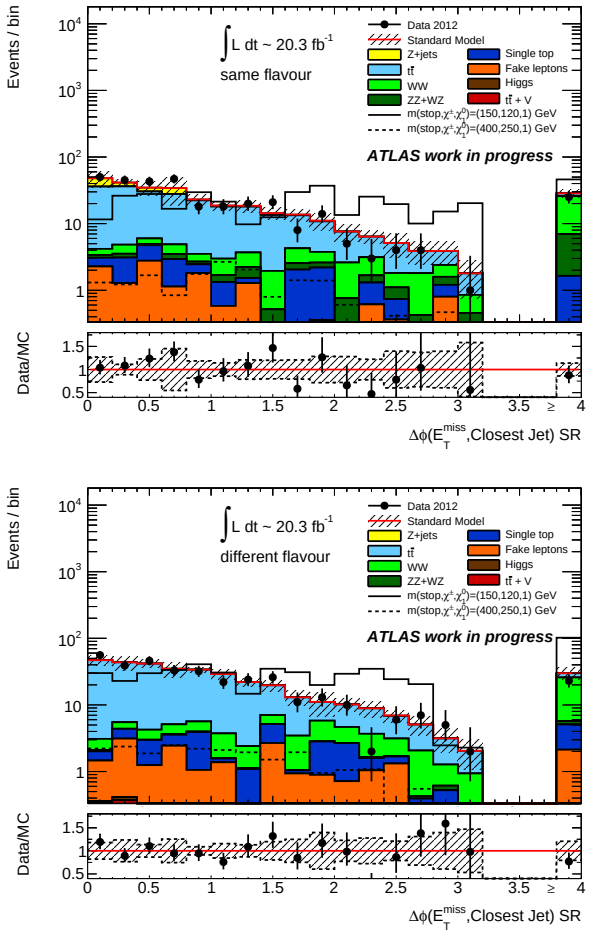

Figure 6.13: Distribution of the angle $\Delta\phi_{min}$ between transverse missing energy and the closest jet, in events passing all the signal candidate selection requirements but for the $\Delta\phi_{min}$ cut itself and $m_{\mathrm{T2}} > 90$ GeV, for same-flavour events (top) and different-flavour events (bottom). The contributions from all SM backgrounds are shown, with the bands representing the total uncertainty. The distributions for two different expected signal models are also shown. The entries in the last bin are for those events without jets

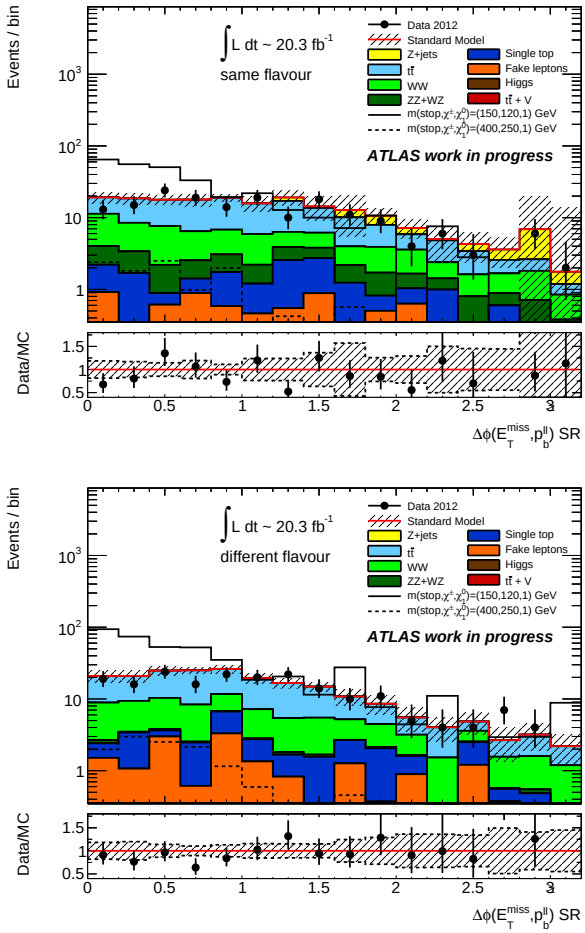

Figure 6.14: Distribution of the angle $\Delta\phi_b$ between transverse missing energy and the p_{Tb}^{ll} vector, in events passing all the signal candidate selection requirements but for the $\Delta\phi_b$ cut itself and $m_{\mathrm{T2}} > 90$ GeV, for same-flavour events (top) and different-flavour events (bottom). The contributions from all SM backgrounds are shown, with the bands representing the total uncertainty. The distributions for two different expected signal models are also shown.

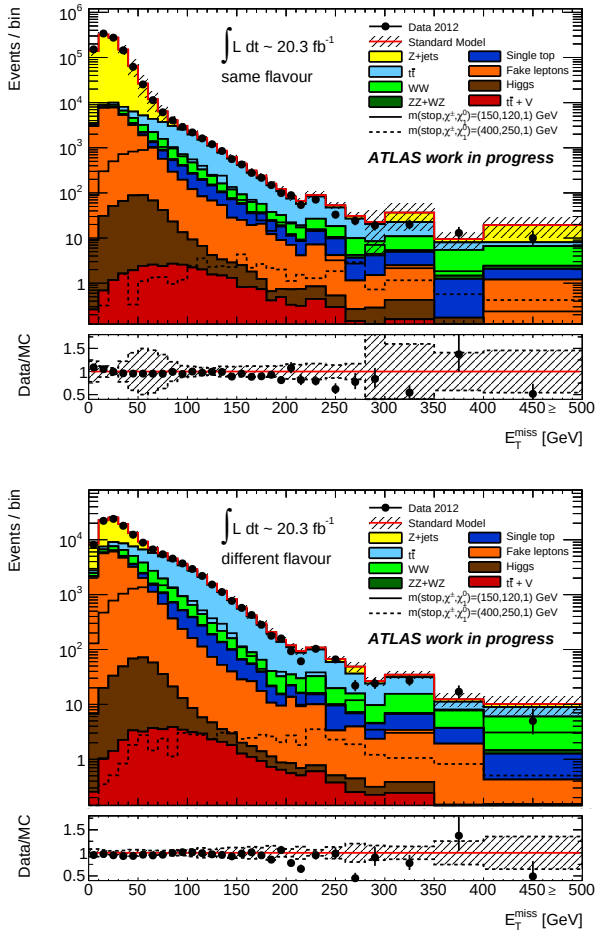

Figure 6.15: Missing transverse momentum distribution in events passing all the signal candidate selection requirements, except that on m_{T2}, for same-flavour events (top) and different-flavour events (bottom). The contributions from all SM backgrounds are shown, with the bands representing the total uncertainty. The distributions for two different expected signal models are also shown.

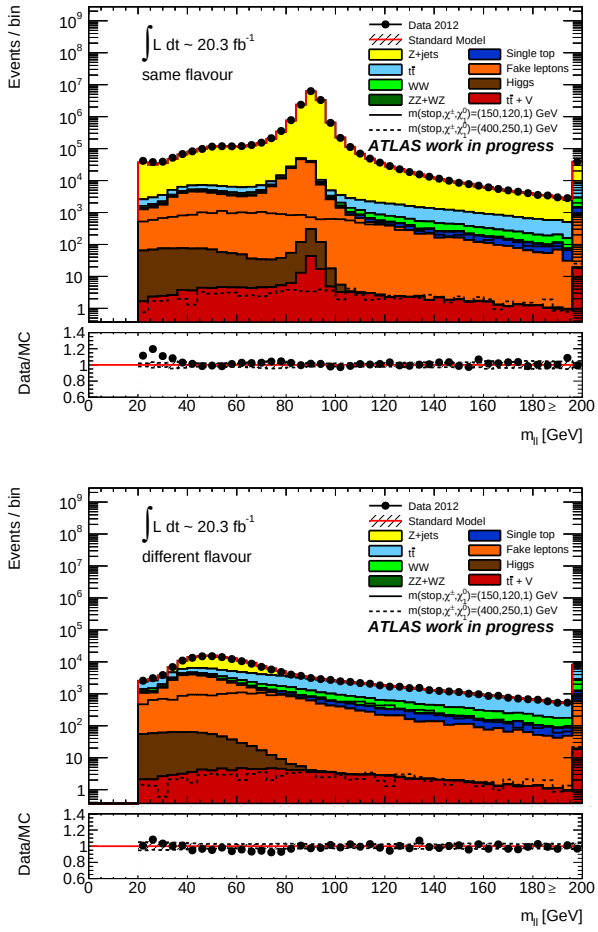

Figure 6.16: $m_{\ell\ell}$ distribution in events passing all the signal candidate selection requirements, except that on m_{T2} and $m_{\ell\ell}$, for same-flavour events (top) and different-flavour events (bottom). The contributions from all SM backgrounds are shown, with the bands representing the total uncertainty. The distributions for two different expected signal models are also shown.

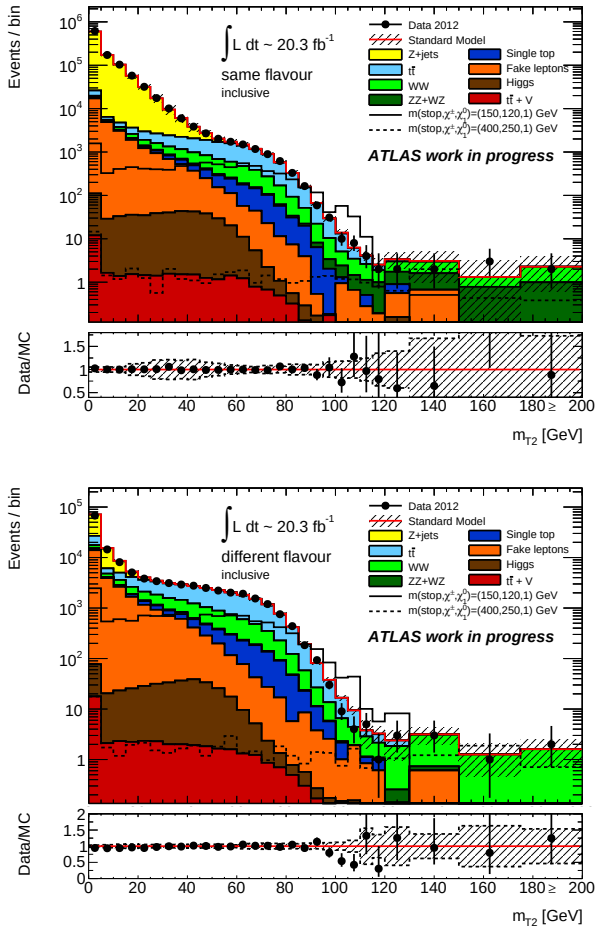

Figure 6.17: m_{T2} distribution in events passing all the signal candidate selection requirements for SR L90 (L120), except that on m_{T2}, for same-flavour events (top) and different-flavour events (bottom). The contributions from all SM backgrounds are shown, with the bands representing the total uncertainty. The distributions for two different expected signal models are also shown.

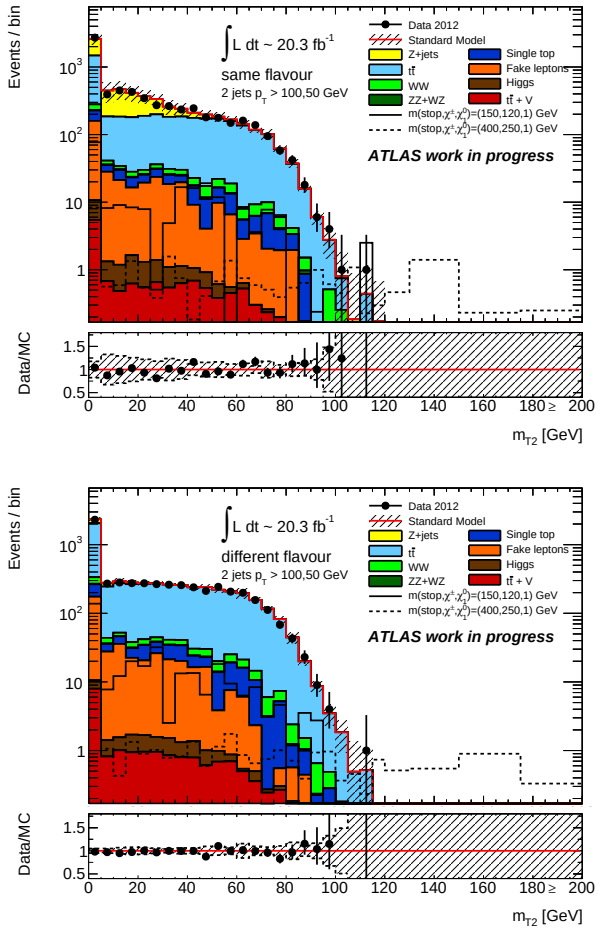

Figure 6.18: m_{T2} distribution in events passing all the signal candidate selection requirements for SR L100, except that on m_{T2}, for same-flavour events (top) and different-flavour events (bottom). The contributions from all SM backgrounds are shown, with the bands representing the total uncertainty. The distributions for two different expected signal models are also shown.

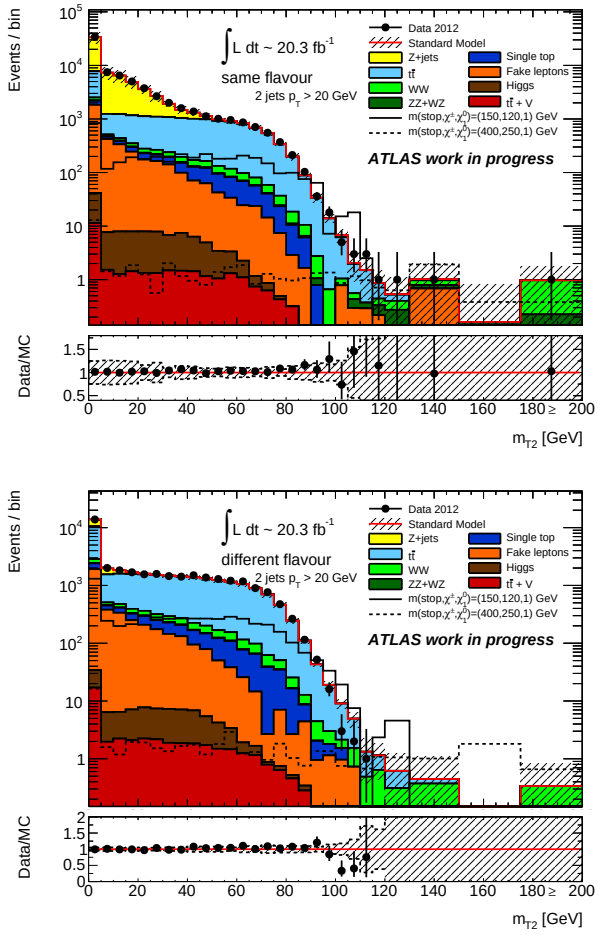

Figure 6.19: m_{T2} distribution in events passing all the signal candidate selection requirements for SR L110, except that on m_{T2}, for same-flavour events (top) and different-flavour events (bottom). The contributions from all SM backgrounds are shown, with the bands representing the total uncertainty. The distributions for two different expected signal models are also shown.

6.5 Background estimate

The dominant SM background contribution to the SR are expected to be the top and the W pair production. The other diboson processes (WZ and ZZ, or ZV) are also expected to be a significant background. The normalization of these backgrounds are determined using the number of observed events in three control regions (CR), each of which is populated mostly by one of the targeted background sources.

Additional SM processes yielding two isolated leptons and $E_{\mathrm{T}}^{\mathrm{miss}}$ (Wt, Z/γ^*+jets, Higgs, $t\bar{t}+W$ and $t\bar{t}+Z$) and providing a sub-dominant contribution to the SR are determined from MC.

The fake lepton background consists of semi-leptonic $t\bar{t}$, s-channel and t-channel single top, W+jets and light- and heavy-flavour jet production. The contribution from this background is small (less than 10% of the total background). It is estimated from data with a method described in section 6.5.3.

The number of events $N_{\mathrm{CR}}^{\mathrm{obs}}$ observed in each control region is related to the backgrounds yields by the equation

$$N_{\mathrm{CR}}^{\mathrm{obs}} = \mu_{t\bar{t}} N_{t\bar{t},\mathrm{CR}}^{\mathrm{MC}} + \mu_{WW} N_{WW,\mathrm{CR}}^{\mathrm{MC}} + \mu_{ZV} N_{WZ+ZZ,\mathrm{CR}}^{\mathrm{MC}} + N_{\mathrm{others,CR}}^{\mathrm{MC}} + N_{\mathrm{fakes,CR}}^{\mathrm{DD}} \quad (6.3)$$

where $N_{t\bar{t},\mathrm{CR}}^{\mathrm{MC}}$, $N_{WW,\mathrm{CR}}^{\mathrm{MC}}$, $N_{WZ+ZZ,\mathrm{CR}}^{\mathrm{MC}}$ are the yields predicted by MC in the CR for $t\bar{t}$, WW, and the sum of WZ and ZZ events, respectively. The μ terms are scale factors which are applied to these backgrounds. $N_{\mathrm{others,CR}}^{\mathrm{MC}}$ is the MC yield for the sum of Wt, tZ, Z/γ^*+jets, Higgs, $t\bar{t}+W$ and $t\bar{t}+Z$ processes, while the number $N_{\mathrm{fakes,CR}}^{\mathrm{DD}}$ of events with fake leptons is determined from data. The scale factors $\mu_{t\bar{t}}$, μ_{WW}, and μ_{ZV} are determined by solving the system defined by equation 6.3 for the three CRs. The expected background in the SR is then given by the same equation

$$N_{\mathrm{SR}}^{\mathrm{obs}} = \mu_{t\bar{t}} N_{t\bar{t},\mathrm{SR}}^{\mathrm{MC}} + \mu_{WW} N_{WW,\mathrm{SR}}^{\mathrm{MC}} + \mu_{ZV} N_{WZ+ZZ,\mathrm{SR}}^{\mathrm{MC}} + N_{\mathrm{others,SR}}^{\mathrm{MC}} + N_{\mathrm{fakes,SR}}^{\mathrm{DD}} \quad (6.4)$$

With this approach, the ratio of events from each background source in the different CR and in the SR is used to derive the normalization of the main backgrounds from the data. The systematic uncertainties described in section 6.6 affect the ratio of MC expected yields in the various regions and are taken into account to determine the uncertainty on the background prediction.

6.5.1 Background Fit

The background in the signal region is estimated with a fit based on the profile likelihood method [106]. The inputs to the fit are as follows, for each of the signal regions:

1. The number of events observed in each of the CRs, and the corresponding number of events expected from simulation.

2. The transfer factors (obtained from the simulation) which relate the number of predicted background events in their associated control region to that predicted in the signal region.

3. The number of misidentified lepton events in each region obtained with the data-driven method.

4. The number of events predicted by the simulation in each region for the minor backgrounds.

The number of events in each of these regions is described using a Poisson probability density function. There are three free parameters considered per channel corresponding to an overall normalization scale ($\mu_{background}$) for each of the $t\bar{t}$, WW and ZV backgrounds. The other background sources are allowed to vary in the fit within their respective uncertainties.

The statistical and systematic uncertainties (see Section 6.6) on the expected values are included in the fit as nuisance parameters which are typically constrained by a Gaussian function with a width corresponding to the size of the uncertainty considered but are not constrained by the fit itself. Systematic uncertainties which are one-sided (like the JER) are symmetrised and correlations between these parameters are taken into account. The product of the various probability density functions forms the likelihood which the fit maximizes by adjusting the free and nuisance parameters.

6.5.2 Control Regions definition

In order to target the main SM backgrounds, three control regions are defined:

- **CRT**, defined by DF events with 40 GeV $< m_{\mathrm{T2}} <$ 80 GeV, $p_{\mathrm{Tb}}^{ll} >$ 30 GeV, and passing all the SR selections on other variables. This region is expected to be populated mostly by $t\bar{t}$ events, with a purity of 75%.

- **CRW**, defined by DF events with 40 GeV $< m_{\mathrm{T2}} <$ 80 GeV and $p_{\mathrm{Tb}}^{ll} <$ 15 GeV, and passing all the SR selections on other variables. This is expected to be populated mostly by WW events, with a purity of 61%.
- **CRZ**, defined by same flavor events which pass all the selections of the SR with $m_{T2} >$ 90 GeV, except that the two-lepton invariant mass is required to be between 71 GeV and 111 GeV. This region is expected to be populated mostly by WZ and ZZ events, with a purity of 68%.

The DF requirement for the top pair and WW CR ensures better purity, since the contamination of Z+jets in the SF channels is significant.

Figure 6.20 shows the distribution of the main variables used to define the three CRs: p_{Tb}^{ll} and $\mathrm{m_{T2}}$. The p_{Tb}^{ll} distribution is shown for events passing all the cuts of CRT and CRW except p_{Tb}^{ll} itself, the two CR thus correspond to the events with $p_{\mathrm{Tb}}^{ll} >$ 30 GeV and $p_{\mathrm{Tb}}^{ll} <$ 15 GeV, respectively. The distribution of $\mathrm{m_{T2}}$ is shown for same flavor events passing all the cuts of CRZ except that on $\mathrm{m_{T2}}$ itself. The CR corresponds to the events with $m_{\mathrm{T2}} >$ 90 GeV in the figure.

The signal contamination in CRT and CRW is in general negligible, with the exception of signal models with top squark masses close to the top quark mass. In this case, the signal contamination can be as high as about 20% in CRT and up to 100% in CRW. Signal contamination in CRZ is generally below 10%, but for signal models with top squark masses below 250 GeV where it becomes closer to 30% and as high as 100% for signal models with small $\Delta m(\tilde{t}_1, \tilde{\chi}_1^{\pm})$. Sensitivity to models with high CR signal contamination is retained because of the very high expected signal yields.

These figures are done with the nominal MC scale factors, and they show that the number of events observed in the CR is in good agreement with the expectations. The expected background composition of the control regions is also reported in table 6.5.

$t\bar{t}$ background CR kinematic distributions

The events passing all the CRT selection requirements have been investigated to check the modeling of the $t\bar{t}$ background in simulation.

The leading and sub-leading lepton $\mathrm{p_T}$ distributions are shown respectively in figures 6.21, 6.22.

The same distributions are shown for the leading and sub-leading jet in figures 6.23, 6.24.

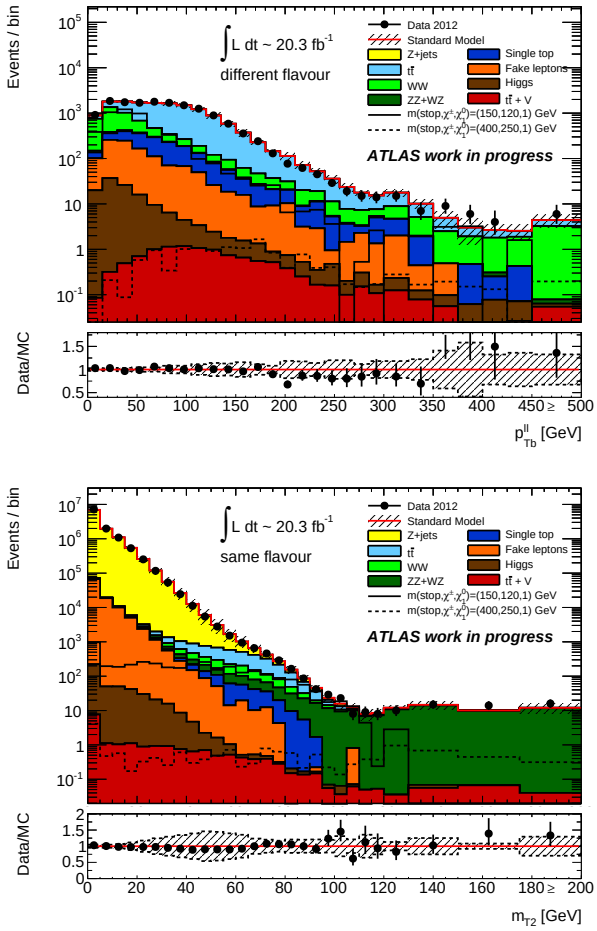

Figure 6.20: Left: distribution of p_{Tb}^{ll} for DF events with 40 GeV $< m_{\mathrm{T2}} <$ 80 GeV, $\Delta\phi > 1.0$ rad and $\Delta\phi_b < 1.5$ rad.
Right: Distribution of m_{T2} for SF events with a di-lepton invariant mass in the 71-111 GeV range, $\Delta\phi > 1.0$ rad and $\Delta\phi_b < 1.5$ rad.
The contributions from all SM backgrounds are shown; the bands represent the total uncertainty. The components labelled "fake lepton" are estimated from data as described in the text; the other backgrounds are estimated from MC simulation. The expected distribution for two signal models is also shown.

Table 6.5: Background fit results for the CRT, CRW and CRZ regions, for an integrated luminosity of 20.3 fb^{-1}. Nominal MC expectations (normalised to MC cross-sections) are given for comparison. The errors shown are the statistical plus systematic uncertainties. Dashes indicate contributions negligible with respect to the other backgrounds.

channel	**CRT**	**CRW**	**CRZ**
Observed events	12158	913	174
Total background events	12158 ± 110	913 ± 30	174 ± 13
Fitted $t\bar{t}$ events	8611 ± 398	136 ± 24	27 ± 6
Fitted WW events	1590 ± 364	626 ± 47	14 ± 4
Fitted WZ events	63 ± 12	14 ± 5	36 ± 7
Fitted ZZ events	1.8 ± 0.5	0.5 ± 0.3	76 ± 13
Expected $Z/\gamma^* \to \ell\ell$ events	9^{+11}_{-9}	$1.3^{+2.1}_{-1.3}$	19 ± 8
Expected $t\bar{t} + V$ events	10.8 ± 3.3	0.08 ± 0.04	0.64 ± 0.21
Expected Wt events	1070 ± 90	35 ± 7	1.4 ± 1.2
Expected tZ events	0.59 ± 0.08	-	0.36 ± 0.07
Expected *Higgs* events	67 ± 21	20 ± 6	0.08 ± 0.04
Events with fake leptons	740 ± 90	81 ± 16	-
Total expected SM events	12735 ± 698	798 ± 94	194 ± 18
Expected $t\bar{t}$ events	9512 ± 640	150 ± 25	30 ± 7
Expected WW events	1256 ± 108	494 ± 75	10.7 ± 2.5
Expected WZ events	73 ± 10	16 ± 5	41.9 ± 5.4
Expected ZZ events	2.1 ± 0.6	0.6 ± 0.3	89.6 ± 6.4
Expected $Z/\gamma^* \to \ell\ell$ events	9^{+11}_{-9}	$1.5^{+2.2}_{-1.5}$	19 ± 8
Expected $t\bar{t} + V$ events	10.8 ± 3.4	0.08 ± 0.04	0.64 ± 0.21
Expected Wt events	1070 ± 90	35 ± 7	1.6 ± 1.1
Expected tZ events	0.59 ± 0.08	-	0.36 ± 0.07
Expected *Higgs* events	67 ± 21	20 ± 6	0.08 ± 0.04
Events with fake leptons	740 ± 90	81 ± 16	-

Figure 6.25 shows the jet multiplicity distribution, while figure 6.26 shows the distributions of the missing transverse momentum.

By comparing figures 6.23-6.25 with the corresponding distributions shown in section 6.4, it is possible to see how selecting larger values of p_{Tb}^{ll} corresponds to the requirement of larger hadronic activity in the event.

A good agreement between data and MC simulation has been found, with no discrepancies observed outside of the estimated uncertainties.

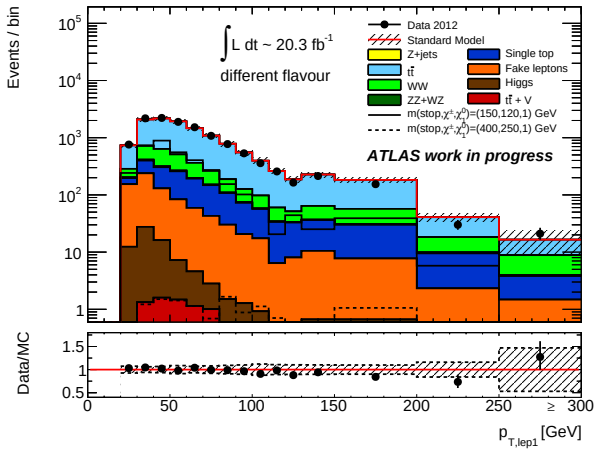

Figure 6.21: p_T distribution for the leading lepton in events passing all the CRT selection requirements. The contributions from all SM backgrounds are shown, with the bands representing the total uncertainty. The distributions for two different expected signal models are also shown.

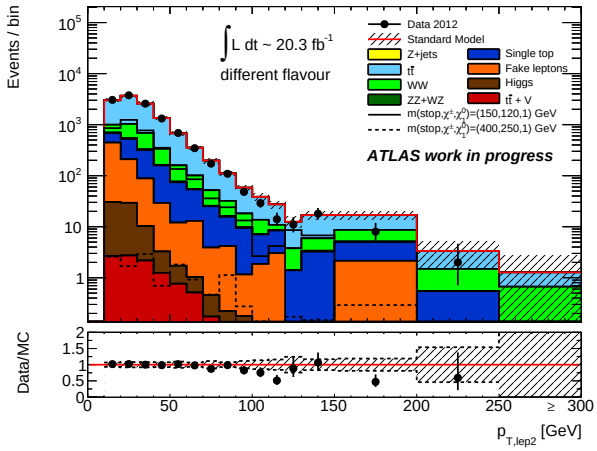

Figure 6.22: p_T distribution for the sub-leading lepton in events passing all the CRT selection requirements. The contributions from all SM backgrounds are shown, with the bands representing the total uncertainty. The distributions for two different expected signal models are also shown.

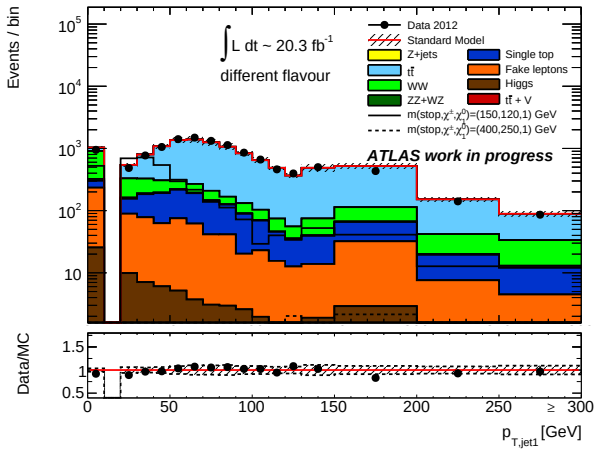

Figure 6.23: p_T distribution for the leading jet in events passing all the CRT selection requirements. The contributions from all SM backgrounds are shown, with the bands representing the total uncertainty. The distributions for two different expected signal models are also shown.

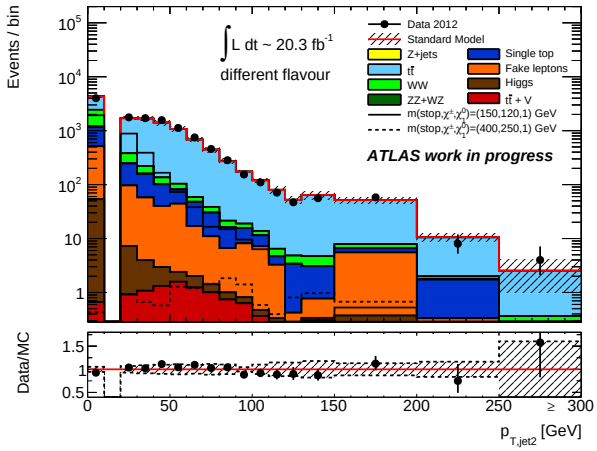

Figure 6.24: p_T distribution for the sub-leading jet in events passing all the CRT selection requirements. The contributions from all SM backgrounds are shown, with the bands representing the total uncertainty. The distributions for two different expected signal models are also shown.

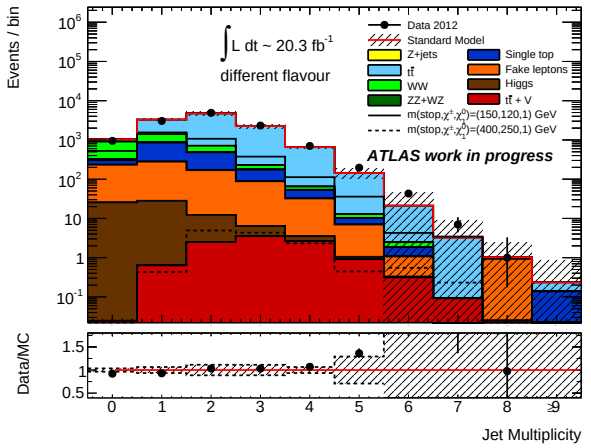

Figure 6.25: Jet multiplicity distribution in events passing all the CRT selection requirements. The contributions from all SM backgrounds are shown, with the bands representing the total uncertainty. The distributions for two different expected signal models are also shown.

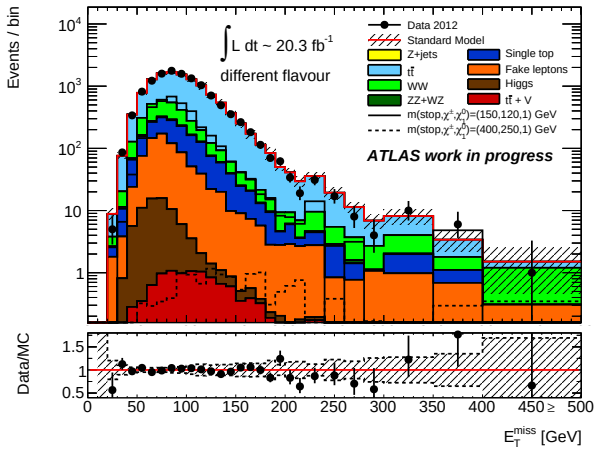

Figure 6.26: Missing transverse momentum distribution in events passing all the CRT selection requirements. The contributions from all SM backgrounds are shown, with the bands representing the total uncertainty. The distributions for two different expected signal models are also shown.

WW background CR kinematic distributions

The events passing all the CRW selection requirements have been investigated to check the modeling of the *WW* background in simulation.

The leading and sub-leading lepton p_T distributions are shown respectively in figures 6.27, 6.28.

The jet multiplicity distribution is illustrated in figure 6.29, effectively showing the effect of an upper cut on p_{Tb}^{ll}, that limits the hadronic activity in the event.

Figure 6.30 shows the distributions of the missing transverse momentum.

A good agreement between data and MC simulation has been found, with no discrepancies observed outside of the estimated uncertainties.

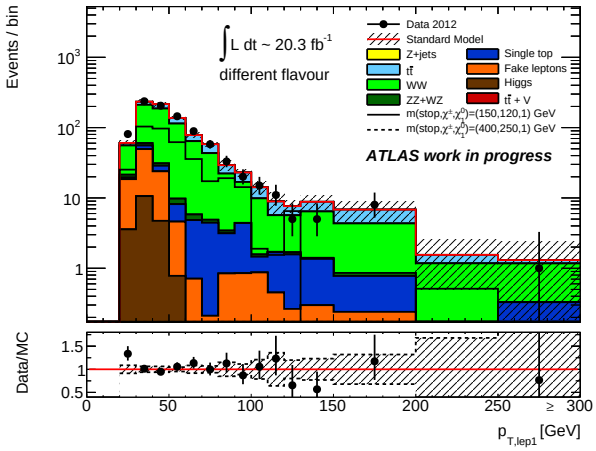

Figure 6.27: p_T distribution for the leading lepton in events passing all the CRW selection requirements. The contributions from all SM backgrounds are shown, with the bands representing the total uncertainty. The distributions for two different expected signal models are also shown.

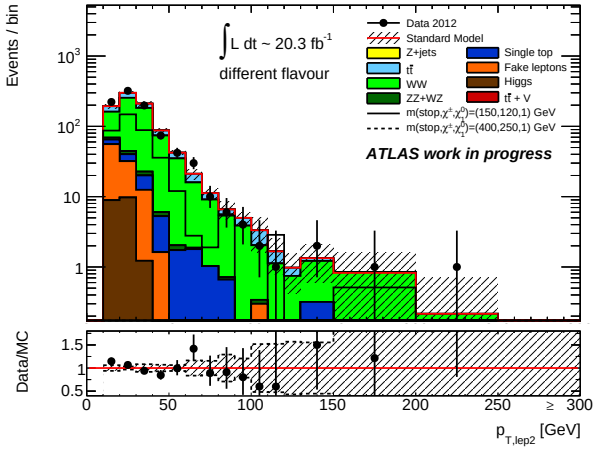

Figure 6.28: p_T distribution for the sub-leading lepton in events passing all the CRW selection requirements. The contributions from all SM backgrounds are shown, with the bands representing the total uncertainty. The distributions for two different expected signal models are also shown.

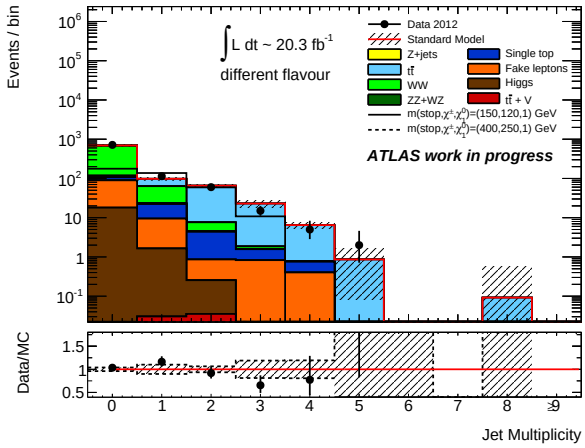

Figure 6.29: Jet multiplicity distribution in events passing all the CRW selection requirements. The contributions from all SM backgrounds are shown, with the bands representing the total uncertainty. The distributions for two different expected signal models are also shown.

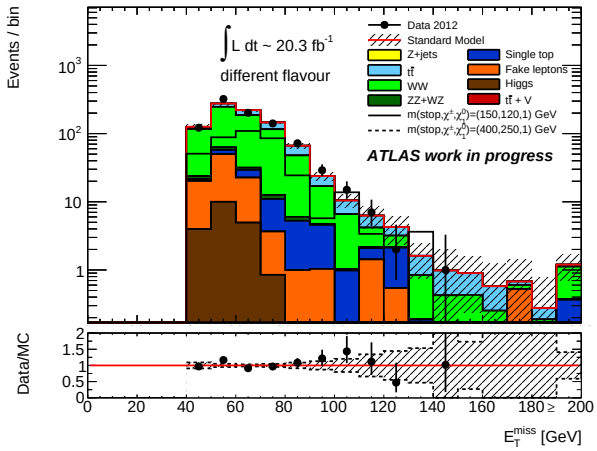

Figure 6.30: Missing transverse momentum distribution in events passing all the CRW selection requirements. The contributions from all SM backgrounds are shown, with the bands representing the total uncertainty. The distributions for two different expected signal models are also shown.

$WZ + ZZ$ background CR kinematic distributions

The events passing all the CRZ selection requirements have been investigated to check the modeling of the $WZ + ZZ$ background in simulation.

The p_T distribution for the leptonically decaying Z boson is shown in figure 6.31.

Figure 6.32 shows the distributions of the missing transverse momentum.

A good agreement between data and MC simulation has been found, with no discrepancies observed outside of the estimated uncertainties.

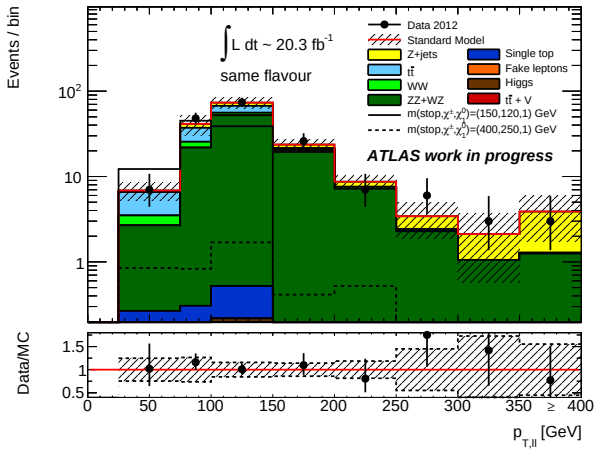

Figure 6.31: p_T distribution of the leptonically decaying Z boson in events passing all the CRZ selection requirements. The contributions from all SM backgrounds are shown, with the bands representing the total uncertainty. The distributions for two different expected signal models are also shown.

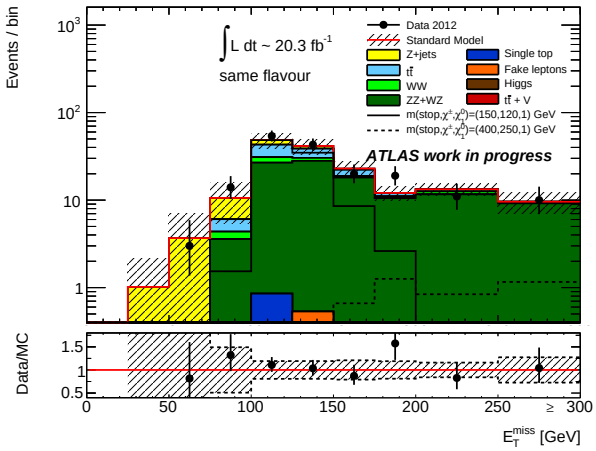

Figure 6.32: Missing transverse momentum distribution in events passing all the CRZ selection requirements. The contributions from all SM backgrounds are shown, with the bands representing the total uncertainty. The distributions for two different expected signal models are also shown.

Minor backgrounds

For the single top production, only the Wt process is included, and the s-channel and t-channel contribution are included by the data driven estimate of processes with at least one fake or non isolated lepton described in the next section. The production of single top in association with a Z boson is also take into account.

For $t\bar{t}+W$and $t\bar{t}+Z$the Leading Order (LO) MadGraph samples are used. The sensitivity to higher order QCD radiation is expected to be small because the signal region selection does not require more jets than present at LO.

With the strategy described above, the Z/γ^*+jets background is estimated from Monte Carlo. In order to assess the reliability of the MC simulation of this background at high values of m_{T2}, an additional region dominated by this background is defined.

In figures 6.33 and 6.34 the distribution of the $\Delta\phi_{\min}$ and $\Delta\phi_b$ variables is shown for events with same flavor lepton pairs and 71 GeV $< m_{\ell\ell} <$ 111 GeV. As it can be seen from the figure, the sample is expected to be dominated by Z+jets events for small (large) values of $\Delta\phi_{\min}$ ($\Delta\phi_b$) variable, while at large (small) values WZ and ZZ production is dominant. The CRZ for $WZ+ZZ$ is indeed derived

from this sample by applying the additional selections $\Delta\phi_{\text{min}} > 1.0$ and $\Delta\phi_b < 1.5$.

The data are in good agreement with the prediction. This proves that the MC simulation describes correctly the rate of Z/γ^*+jets events for large values of m_{T2}, and the fact that the $\Delta\phi_{\text{min}}$ and $\Delta\phi_b$ shapes are well described gives confidence that the Z/γ^*+jets yield after the cuts on these variables can also be derived from MC.

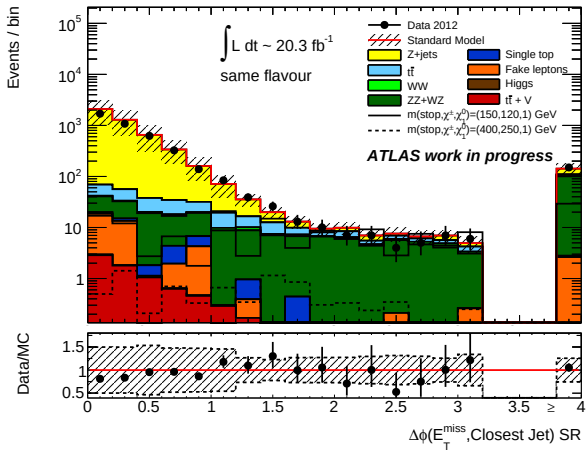

Figure 6.33: Distribution of $\Delta\phi_{\text{min}}$ for events with same flavor lepton pairs, 71 GeV $< m_{\ell\ell} <$ 111 GeV, and $m_{T2} > 90$ GeV. The contributions from all SM backgrounds are shown, with the bands representing the total uncertainty. The distributions for two different expected signal models are also shown.

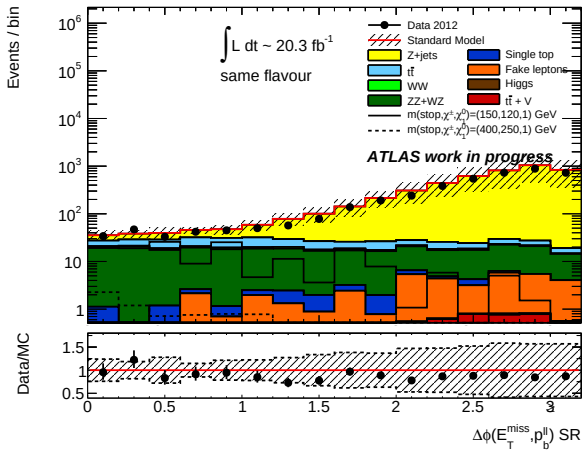

Figure 6.34: Distribution of $\Delta\phi_b$ for events with same flavor lepton pairs, 71 GeV $< m_{\ell\ell} <$ 111 GeV, and $m_{\mathrm{T2}} > 90$ GeV. The contributions from all SM backgrounds are shown, with the bands representing the total uncertainty. The distributions for two different expected signal models are also shown.

6.5.3 Fake lepton background

The estimation of this background is performed with a data-driven Matrix Method: the technique is similar to that used in the previous search and is exhaustively explained in section 5.5.4.

However, the measurement of the leptons fake rate f, i.e. the probability of a loose (baseline) fake lepton to pass the tight (signal) criteria, has been reviewed following a new strategy which will be described in the following section. The measurement of the real efficiency r is instead left unchanged.

Fake rate

The leptons fake rate is computed in two separate fake-enriched regions depending on the p_T of the lepton:

- Case A: $p_T < 25$ GeV. The event is assumed to be yielded by low-p_T dileptonic triggers. f is obtained from a sample of different-flavor same-sign events.
- Case B: $p_T > 25$ GeV. The event is assumed to be yielded by one-lepton triggers. f is measured from a one-lepton sample, collected with non-isolated prescaled triggers, and requiring $n_{jet} > 1$, $\Delta\phi_{\ell,E_T^{miss}} < 0.5$ and $E_T^{miss} < 25$ GeV.

The parametrisations of the fake rate are treated separately for the two cases.

In case A, f is parameterized in a set of two-dimensional planes defined by one variable out of the lepton η, p_T, the event m_{T2} or jets multiplicity against m_{eff} (defined as the scalar sum of the lepton p_T E_T^{miss} and the first four jet p_T).

In case B, the fake rate is measured as a function of the lepton p_T and η. In the muon channel, the parametrization is stopped at 40 GeV, since the high-p_T regions have a predominant contribution from prompt muons.

For each CR, the contamination of events with prompt (real) leptons originating from SM background such as W+jets, Z+jets, top pairs, single top and dibosons, has been evaluated by MC and subtracted to the number of observed events in data.

6.5.4 Validation Regions definition

In order to verify the goodness of the results of the background fit coming from the CRs, four validation regions (VR) are defined.

Two validation regions (VRSF and VRDF) have been designed to check the background estimate in a kinematic region as close as possible to the signal regions.
The remaining VRs (VRT20 and VRT100) have been used to validate the $t\bar{t}$ estimation for different selections of the jet momenta.

- **VRSF**, defined by SF events with 80 GeV $< m_{\mathrm{T2}} <$ 90 GeV and passing the SR selections on other variables. This region is expected to be populated by a background composition similar to the one in SR L90.

- **VRDF**, defined by DF events with 80 GeV$< m_{\mathrm{T2}} <$ 90 GeV and passing the SR selections on other variables. This region is expected to be populated by a background composition similar to the one in SR L90.

- **VRT20**, defined by events with 40 GeV $< m_{\mathrm{T2}} <$ 80 GeV, $p_{\mathrm{Tb}}^{ll} >$ 30 GeV, requiring at least 2 jets and passing the SR selections on other variables. This region is expected to be populated mostly (with 88% purity) by $t\bar{t}$ events.

- **VRT100**, defined by events with 40 GeV$< m_{\mathrm{T2}} <$ 80 GeV, $p_{\mathrm{Tb}}^{ll} >$ 30 GeV, requiring at least 1 jets with $p_{\mathrm{T}} >$ 100 GeV, an additional jet with $p_{\mathrm{T}} >$ 50 GeV and passing the SR selections on other variables. This region is expected to be populated mostly (with 90% purity) by $t\bar{t}$ events.

The expected background composition of the VR is reported in table 6.6.

The agreement of the background estimation with the observed data yields has been found excellent: the largest discrepancy is observed for VRT20, with the deviation below 1 standard deviation of the expected yield.

The signal contamination in the VRs can be up to $\sim$ 100% for signal models with top quark-like kinematics and becomes negligible when considering models with increasing top squark masses.

Table 6.6: Background fit results for the VRSF, VRDF, VRT20 and VRT100 regions, for an integrated luminosity of 20.3 fb^{-1}. The errors shown are the statistical plus systematic uncertainties. Dashes represent contributions negligible with respect to the other backgrounds.

channel	**VRSF**	**VRDF**	**VRT20**	**VRT100**
Observed events	494	622	8162	1370
Total background events	500 ± 40	620 ± 50	7800 ± 400	1390 ± 110
Fitted $t\bar{t}$ events	338 ± 19	430 ± 30	6800 ± 400	1230 ± 110
Fitted WW events	97 ± 22	120 ± 30	290 ± 70	40 ± 15
Fitted WZ events	3.6 ± 0.8	2.0 ± 1.2	13 ± 3	1.4 ± 1.2
Fitted ZZ events	2.2 ± 0.7	0.15 ± 0.07	0.27 ± 0.17	$0.02^{+0.02}_{-0.02}$
Expected $Z/\gamma^* \to \ell\ell$ events	4^{+5}_{-4}	-	3^{+5}_{-3}	$1.0^{+1.1}_{-1.0}$
Expected $t\bar{t} + V$ events	0.48 ± 0.18	0.80 ± 0.27	10 ± 3	4.1 ± 1.3
Expected Wt events	40 ± 8	60 ± 10	430 ± 50	62 ± 8
Expected tZ events	0.04 ± 0.02	0.01 ± 0.01	0.33 ± 0.05	0.06 ± 0.02
Expected *Higgs* events	0.39 ± 0.16	0.55 ± 0.20	14 ± 4	1.7 ± 0.5
Events with fake leptons	10 ± 3	13 ± 4	280 ± 30	45 ± 7

6.6 Systematic uncertainties

Various systematic uncertainties affecting the predicted background rates in the signal regions are considered. Such uncertainties are either used directly in the evaluation of the predicted background in the SR when this is derived by the pure MC prediction or to compute the uncertainty on the transfer factor and propagate it to the predicted event yields in the SR when the background is constrained using the fitting method described in section 6.5 (for $t\bar{t}$ and dibosons).

The most important instrumental uncertainties are the Jet Energy Resolution and the uncertainty on E_{T}^{miss} soft terms scale. The uncertainties on the leptons are smaller by an order of magnitude.

In addition to these uncertainties also the statistical error coming from the limited MC statistics has to be considered. Each source of systematics is handled following the ATLAS combined performance group recommendations.

Among theoretical uncertainties, the generator and ISR/FSR are the most important systematics for the $t\bar{t}$ and diboson estimates. Luminosity and cross section uncertainties are relatively small.

Many uncertainties have been estimated with techniques similar to those shown in section 5.6, a complete description will be given only for the uncertainties that differ significantly from the previous analysis.

6.6.1 Experimental systematics

The following experimental systematic uncertainties were found to be non-negligible:

- **Jet energy scale and resolution**. The components of the jet energy scale uncertainty are varied by $\pm 1\sigma$ in the MC simulation in order to obtain the resulting uncertainty in the event yield. The impact on the event yield of jet energy resolution effects is estimated by applying an additional smearing to the jet transverse momenta. The JES and JER variations applied to the jet momenta are propagated to the $E_{\mathrm{T}}^{\mathrm{miss}}$.

- E_{T}^{miss} **soft terms energy scale and resolution, pile-up**. The uncertainties related to the contribution to $E_{\mathrm{T}}^{\mathrm{miss}}$ from the energy scale and resolution of the calorimeter cells not associated to electrons, muons or jets, and also from low momentum (7 GeV $< p_T <$ 25 GeV) jets have been evaluated separately and added in quadrature.

The uncertainty due to the modeling of pile-up is computed by comparing the nominal yields (obtained rescaling the value of the average number μ of proton-proton interactions per bunch crossing by 0.9 to match the μ profile observed in data) and the unrescaled yields. Please note that this procedure is the opposite of the one used in the analysis described in chapter 5. The resulting systematic uncertainty is symmetrized.

- **Lepton efficiency, energy scale and resolution** The impact of these uncertainties is taken into account by checking the variation of results obtained by using the nominal lepton scale factors and the scale factors varied by the systematic uncertainty provided by the combined performance groups.

- **Trigger efficiency** Since this analysis does not apply any reweighting to match the efficiency of the trigger scheme used on data, the difference between the nominal MC predictions for the main backgrounds and the reweighted ones has been taken has an additional uncertainty and applied to the whole SM background prediction. This was done since the difference between nominal and reweighed results is small (3%) and negligible with respect to the total background uncertainty.

6.6.2 Theoretical systematics

The following theoretical systematic uncertainties have been taken into account:

- $t\bar{t}$ **production generator**. The uncertainty associated to the choice of a specific MonteCarlo generator. This is evaluated comparing the predictions of MC@NLO and POWHEG (hadronised with HERWIG).

- $t\bar{t}$ **parton shower**. This uncertainty is evaluated comparing the predictions of HERWIG and PYTHIA when used to hadronize the same POWHEG sample.

- **ISR/FSR**. The uncertainty related to ISR and FSR in $t\bar{t}$ events is evaluated considering two dedicated ACERMC samples with varying settings, and taking half of the difference between these samples as systematic uncertainty.

- Z/γ^***+jets generator**. The predictions of the baseline SHERPA generator are compared with those from ALPGEN. Due to the low statistics of the ALPGEN samples, this uncertainty has been evaluated in a sample with looser selections: the angular cuts on $\Delta\phi_{min}$ and $\Delta\phi_b$ were removed.

- **Diboson generator**. The uncertainty associated to the choice of a specific MonteCarlo generator is evaluated comparing the predictions of POWHEG and SHERPA.

6.6.3 Other systematics

- **Luminosity**. The uncertainty on the luminosity [120] estimated for the whole dataset used in the analysis is taken to be 2.8%.

- **Cross section**. The uncertainty related to the cross section value is taken to be 5% for the Z/γ^*+jets boson production [104]. For $t\bar{t}$, the recommended value of $\sigma_{t\bar{t}} = 253^{+13}_{-15}$ pb is used for a top quark mass of 172.5 GeV as obtained from approximate NNLO QCD calculations [105]. The cross section uncertainties for WW, ZZ and WZ are 6%, 5% and 7% respectively [46, 63]. For single top, the cross section of 22.4 ± 1.5 pb is used for the Wt channel [47]. For $t\bar{t} + W$ and $t\bar{t} + Z$ a cross section of 0.23 ± 0.07 pb and 0.21 ± 0.06 pb are used respectively. A 25% uncertainty is considered on the W+jets in the fake rate estimate.

  The uncertainties for $t\bar{t}$ and diboson production cross section do not play any role in the background estimate because these processes are normalized to data in appropriate control regions, but they contribute to the uncertainty on the MC predictions shown in the figures. The uncertainty on single top, $t\bar{t} + Z$ and $t\bar{t} + W$ cross sections contribute to the background uncertainty in the SR but they are negligible compared to other uncertainties, because of the small rates of these backgrounds in the SR.

- **Fake-lepton background**. An uncertainty is assigned to the fake background from the comparison of results of the fake rate measurement from different CRs. An additional systematic uncertainty takes into account the limited statistics in the CRs. The uncertainties on lepton ID measurement and on trigger modeling have been found to have a negligible impact on the analysis.

The breakdown of the main background uncertainties in individual sources is reported in Table 6.7. The total uncertainty is found to vary from about 16% in SR L90 to about 45% in SR L120.

Table 6.7: Breakdown of the dominant systematic uncertainties on background estimates in the various signal regions. Note that the individual uncertainties can be correlated, and do not necessarily add up quadratically to the total background uncertainty.

Uncertainty of channel	**L90**	**L100**	**L110**	**L120**
Total background expectation	300	5.2	9.3	19
Total uncertainty	$\pm$50	$\pm$2.2	$\pm$3.5	$\pm$9
Jet energy resolution	$\pm$21.47	$\pm$1.04	$\pm$0.04	$\pm$0.75
$t\bar{t}$ generator	$\pm$20.68	$\pm$1.15	$\pm$2.57	$\pm$0.38
Soft term scale	$\pm$20.30	$\pm$0.56	$\pm$0.23	$\pm$0.31
Pile-up	$\pm$19.97	$\pm$0.49	$\pm$0.66	$\pm$1.00
μ_{WW}	$\pm$14.96	$\pm$0.18	$\pm$0.62	$\pm$2.21
$\mu_{t\bar{t}}$	$\pm$14.25	$\pm$0.29	$\pm$0.28	$\pm$0.09
$t\bar{t}$ cross section	$\pm$10.25	$\pm$0.21	$\pm$0.20	$\pm$0.06
$t\bar{t}$ ISRFSR	$\pm$9.01	$\pm$0.60	$\pm$0.03	$\pm$0.66
Trigger efficiency	$\pm$8.58	$\pm$0.16	$\pm$0.25	$\pm$0.54
Diboson generator	$\pm$8.45	$\pm$0.52	$\pm$1.42	$\pm$8.01
$t\bar{t}$ parton shower	$\pm$7.98	$\pm$0.44	$\pm$0.75	$\pm$0.46
Diboson cross section	$\pm$5.33	$\pm$0.07	$\pm$0.25	$\pm$0.93
Soft term resolution	$\pm$4.24	$\pm$0.36	$\pm$0.31	$\pm$0.04
μ_{ZV}	$\pm$2.15	$\pm$0.04	$\pm$0.17	$\pm$0.77
Fakes background estimate	$\pm$1.52	$\pm$0.00	$\pm$0.02	$\pm$0.08
Wt cross section	$\pm$1.40	$\pm$0.00	$\pm$0.00	$\pm$0.02
Jet energy scale	$\pm$1.06	$\pm$0.26	$\pm$0.12	$\pm$0.15
Z/γ^*+jets generator	$\pm$0.76	$\pm$0.04	$\pm$0.03	$\pm$0.02
Luminosity	$\pm$0.73	$\pm$0.01	$\pm$0.02	$\pm$0.03
$t\bar{t}$+V cross section	$\pm$0.55	$\pm$0.11	$\pm$0.18	$\pm$0.15
Higgs cross section	$\pm$0.19	$\pm$0.01	$\pm$0.01	$\pm$0.09
MC statistics	$\pm$6.86	$\pm$0.69	$\pm$1.02	$\pm$1.27

6.6.4 Background fit results and nuisance parameters

The scale factors determined by the background fit and used to normalize the main backgrounds are shown in table 6.8, together with theirs uncertainties.

All the measured values are consistent with unity, with the largest deviation coming from μ_{WW}. This result, while still being compatible with the nominal MC prediction, is not surprising. In fact, the ATLAS measurement of the WW cross section [**?**] is showing a similar deviation from the expected prediction.

Table 6.8: Fitted background scale factors and their total uncertainties.

Scale Factor	Value
$\mu_{t\bar{t}}$	0.91 ± 0.07
μ_{WW}	1.27 ± 0.24
μ_{ZV}	0.85 ± 0.16

The background fit is intended to determine the background normalizations and should not constrain the nuisance parameters associated to the various systematic uncertainties. Table 6.9 reports the output values for these parameters after the background fit: they all have a central value very close to zero (the nominal) and uncertainties close to 1, which indicates no change compared to the original allowed range.

Table 6.9: Results of the fit: nuisance parameters associate to systematic uncertainties and their global correlation.

Nuisance Parameter	**Final Value $\pm$ Error**	**Global Correlation**
Higgs cross section	0.00 ± 0.99	0.25
Jet energy resolution	-0.01 ± 0.99	0.46
Jet energy scale	0.00 ± 0.99	0.71
Wt cross section	0.01 ± 0.99	0.54
Z/γ^*+jets generator	-0.01 ± 0.99	0.32
Soft term scale	-0.01 ± 0.99	0.36
Soft term resolution	-0.01 ± 0.99	0.95
Diboson generator	-0.01 ± 0.99	0.25
Diboson cross section	0.01 ± 0.99	0.86
Pile-up	-0.01 ± 0.99	0.80
Fakes background estimate	0.00 ± 0.99	0.76
$t\bar{t}$ generator	0.01 ± 0.99	0.37
$t\bar{t}$ ISRFSR	0.01 ± 1.00	0.41
$t\bar{t}$ parton shower	0.00 ± 1.00	0.06
$t\bar{t}$ cross section	0.00 ± 1.00	0.99
Trigger efficiency	0.00 ± 0.99	0.96
$t\bar{t}$+V cross section	0.00 ± 0.99	0.03

6.7 Results

The number of events observed in each of the signal regions is reported in Table 6.10, and compared to the total expected background. The breakdown of the background in its individual components, together with the total uncertainties discussed in the previous section, is also reported.

Good agreement is found between data and the expected SM background in all the signal regions.

Table 6.10: Background fit results for the L90, L100, L110 and L120 regions, for an integrated luminosity of 20.3 fb^{-1}. The errors shown are the statistical plus systematic uncertainties. Dashes represent contributions negligible with respect to the other backgrounds.

channel	**L90**	**L100**	**L110**	**L120**
Observed events	274	3	8	18
Total background events	300 ± 50	5.2 ± 2.2	9.3 ± 3.5	19 ± 9
Fitted $t\bar{t}$ events	172 ± 33	3.5 ± 2.1	3.4 ± 2.9	$1.05^{+1.08}_{-1.05}$
Fitted WW events	78 ± 20	1.0 ± 0.5	3.2 ± 1.4	12 ± 6
Fitted WZ events	4.7 ± 1.0	$0.09^{+0.16}_{-0.09}$	0.36 ± 0.28	1.2 ± 1.0
Fitted ZZ events	6.9 ± 1.7	0.14 ± 0.11	0.56 ± 0.31	3.0 ± 1.1
Expected $Z/\gamma^* \to \ell\ell$ events	2.8 ± 1.4	$0.14^{+0.14}_{-0.14}$	$0.09^{+0.14}_{-0.09}$	$0.07^{+0.09}_{-0.07}$
Expected $t\bar{t} + V$ events	1.8 ± 0.6	0.35 ± 0.14	0.62 ± 0.21	0.51 ± 0.18
Expected Wt events	21 ± 7	$0.00^{+0.18}_{-0.00}$	-	$0.35^{+0.39}_{-0.35}$
Expected tZ events	0.04 ± 0.02	-	0.01 ± 0.01	0.01 ± 0.01
Expected *Higgs* events	0.7 ± 0.2	$0.02^{+0.02}_{-0.02}$	0.03 ± 0.03	0.31 ± 0.12
Events with fake leptons	13.0 ± 3.4	-	1.0 ± 0.6	1.1 ± 0.8

6.8 Interpretation and limit setting

The observed event yield in each of the signal regions (summarized in Table 6.10) is compared to the SM expectations using a frequentist significance test. We define a likelihood function $\mathcal{L}(n_s)$, following the same procedure that was described in section 5.8.

No excess of events in data is observed, and limits at 95% CL are derived on the

visible cross section $\sigma_{\text{vis}} = \sigma \times \epsilon \times \mathcal{A}$, where σ is the total production cross section for the non-SM signal, $\mathcal{A}$ is the acceptance defined by the fraction of events passing the geometric and kinematic selections at particle level, and ϵ is the detector reconstruction, identification and trigger efficiency. These observed and expected limits are shown in Table 6.11. Only background uncertainties are considered for the model independent limits. Further information on the statistical techniques used to treat the data can be found in appendix A.

Table 6.11: Expected and observed upper limits on the number of non-SM events and the visible cross-section. For each SR the numbers are calculated using toy Monte Carlo pseudo-experiments. The equivalent limits on the visible cross-section calculated using an asymptotic method [106] are given in parenthesis.

Signal Region	$S^{95}_{\text{exp.}}$	$S^{95}_{\text{obs.}}$	σ^{exp}_{vis}[**fb**]	σ^{obs}_{vis}[**fb**]
L90	85	74	4.2 (4.3)	3.6 (3.7)
L100	6.0	4.7	0.32 (0.30)	0.28 (0.24)
L110	9.6	9.4	0.46 (0.45)	0.44 (0.42)
L120	17	17	0.82 (0.85)	0.83 (0.82)

All the SRs used so far have been optimised for discovery. In order to improve the exclusion power of the analysis in the absence of any excesses above SM predictions, for each signal hypothesis the limits are obtained from a statistical combination of 7 statistically independent SRs. These SRs are labelled Sn, with n going from 1 to 7, and are constructed by selecting mutually exclusive regions in the (Jet selections, m_{T2}) plane defined as shown in Figure 6.35. These regions are the same as the original 4 SR but with discrimination of the shared regions of phase space.

The same background fit described in section 6.5 has been used to estimate the SM background in each of these SRs. Table 6.12 shows the number of events observed in each of the exclusion signal regions, compared to the total expected background.

The results obtained are statistically combined and used to derive limits on the mass of a pair-produced top squarks $\tilde{t}_1$ decaying with 100% branching ratio (BR) into the lightest chargino and a *bottom* quark.

The exclusion limits on these parameters are evaluated in various two-dimensional

Table 6.12: Background fit results for the S1, S2, S3, S4, S5, S6 and S7 signal regions, for an integrated luminosity of 20.3 fb^{-1}. The errors shown are the statistical plus systematic uncertainties. Dashes represent contributions negligible with respect to the other backgrounds.

channel	**S1**	**S2**	**S3**	**S4**
Observed events	250	1	2	3
Total background events	273 ± 42	3.4 ± 1.8	1.3 ± 0.6	3.7 ± 2.7
Fitted $t\bar{t}$ events	165 ± 29	2.6 ± 1.8	0.9 ± 0.5	$1.9^{+2.6}_{-1.9}$
Fitted WW events	65 ± 16	0.43 ± 0.28	$0.24^{+0.26}_{-0.24}$	1.0 ± 0.4
Fitted WZ events	3.4 ± 1.0	$0.05^{+0.08}_{-0.05}$	$0.02^{+0.09}_{-0.02}$	$0.10^{+0.15}_{-0.10}$
Fitted ZZ events	3.8 ± 0.7	$0.04^{+0.05}_{-0.04}$	$0.02^{+0.05}_{-0.02}$	$0.07^{+0.09}_{-0.07}$
Expected $Z/\gamma^* \to \ell\ell$ events	2.6 ± 1.4	$0.10^{+0.13}_{-0.10}$	$0.01^{+0.02}_{-0.01}$	$0.00^{+0.04}_{-0.00}$
Expected $t\bar{t} + V$ events	0.97 ± 0.32	0.15 ± 0.07	0.07 ± 0.04	0.14 ± 0.06
Expected Wt events	20 ± 6	0.00 ± 0.11	-	-
Expected tZ events	0.03 ± 0.01	-	-	-
Expected *Higgs* events	0.31 ± 0.12	$0.02^{+0.02}_{-0.02}$	-	-
Events with fake leptons	11.5 ± 3.3	-	-	0.4 ± 0.4

channel	**S5**	**S6**	**S7**
Observed events	0	3	15
Fitted bkg events	0.5 ± 0.4	3.8 ± 1.6	15 ± 7
Fitted $t\bar{t}$ events	$0.00^{+0.22}_{-0.00}$	$0.5^{+0.5}_{-0.5}$	$0.6^{+0.6}_{-0.6}$
Fitted WW events	0.28 ± 0.23	1.7 ± 1.1	9.5 ± 5.7
Fitted WZ events	$0.01^{+0.01}_{-0.01}$	0.23 ± 0.22	0.9 ± 0.9
Fitted ZZ events	0.08 ± 0.07	0.39 ± 0.16	2.5 ± 1.0
Expected $Z/\gamma^* \to \ell\ell$ events	0.02 ± 0.02	$0.05^{+0.09}_{-0.05}$	-
Expected $t\bar{t} + V$ events	0.14 ± 0.07	0.27 ± 0.11	0.10 ± 0.06
Expected Wt events	-	-	$0.35^{+0.39}_{-0.35}$
Expected tZ events	-	$0.01^{+0.01}_{-0.01}$	-
Expected *Higgs* events	-	0.03 ± 0.02	0.28 ± 0.11
Events with fake leptons	-	0.6 ± 0.5	$0.5^{+0.6}_{-0.5}$

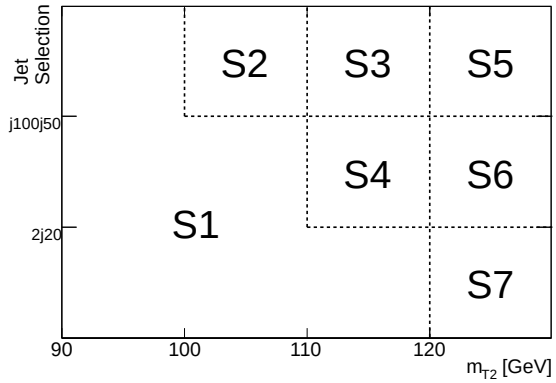

Figure 6.35: Definition of the SRs used for deriving the exclusion limits. The (jet selections, m_{T2}) plane has been divided in 7 non-overlapping SRs. The label "2j20" stands for the requirement of at least 2 jets above the minimal p_T threshold, while the label "j100j50" stands for the requirement of at least one jet with $p_T > 100$ GeV and an additional one with $p_T > 50$ GeV.

slices: in the top squark-chargino mass plane for a neutralino with a mass of 1 GeV (Figure 6.36); in the top squark-neutralino mass plane for a fixed value of $m(\tilde{t}_1) - m(\tilde{\chi}_1^{\pm}) = 10$ GeV (Figure 6.37); in the chargino-neutralino mass plane for a fixed 300 GeV top squark (Figure 6.38); and in the top squark-neutralino mass plane for $m(\tilde{\chi}_1^{\pm}) = 2m(\tilde{\chi}_1^0)$ (Figure 6.39) and in the top squark-neutralino mass plane for fixed 150 GeV chargino mass (Figure 6.40). Each of these figures shows also the observed upper limit on the signal cross-section for each of the specific supersymmetric mass hierarchies used in the interpretation.

Uncertainties on the detector response, SM process cross-sections, luminosity and MC samples statistics are taken into account. These limits are obtained by using a likelihood test comparing the numbers of events in the signal regions with the fitted background expectation, taking into account any signal contamination in the CRs.

For the case of a massless neutralino, a top squark $\tilde{t}_1$ with a mass between 150 and 435 GeV decaying to a b-quark and a chargino is excluded at 95% CL for a chargino approximately degenerate with the top squark. For a 300 GeV top squark decaying to a b-quark and a chargino, chargino masses between 100 and 290 GeV are excluded for a lightest neutralino with mass below 70 GeV.

Limits are also set for the first time on the direct 3-body decay mode, $\tilde{t}_1 \rightarrow W\tilde{\chi}_1^0 b$, excluding a top squark mass between 110 and 170 GeV, under the assumption of a massless neutralino. The analysis achieves the best sensitivity for intermediate values of $m(\tilde{t}_1) - m(\tilde{\chi}_1^0)$ and decreases approaching either the lower $m(\tilde{t}_1) - m(\tilde{\chi}_1^0) = m(W) + m(b)$ or upper $m(\tilde{t}_1) - m(\tilde{\chi}_1^0) = m(t)$ kinematic limits. This drop in sensitivity is due to a decrease of the acceptance of the m_{T2} cut. For low values of $m(\tilde{t}_1) - m(\tilde{\chi}_1^0)$ this is due to the decrease of the kinematic endpoint for this variable at truth level. For high values of $m(\tilde{t}_1) - m(\tilde{\chi}_1^0)$ the endpoint increases but kinematic configurations with m_{T2} close to the endpoint are strongly disfavored by the top quark propagator, which enhances kinematic configurations with high Wb invariant mass and low $\tilde{\chi}_1^0$ momenta.

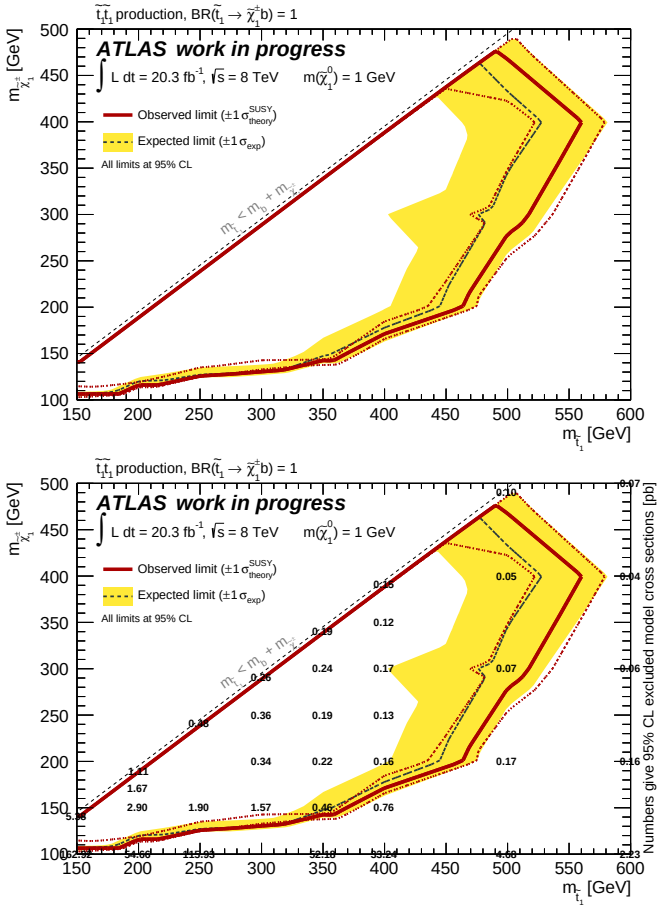

Figure 6.36: Exclusion limits (top) and observed upper limit on the signal cross-section (bottom) at 95% CL in the top-squark neutralino mass plane for a fixed value of $m(\tilde{\chi}_1^0) = 1$ GeV. The dashed and solid lines show the 95% C.L. expected and observed limits, respectively, including all uncertainties except for the theoretical signal cross-section uncertainty (PDF and scale). The band around the expected limit shows the $\pm 1\sigma$ result. The dotted $\pm 1\sigma$ lines around the observed limit represent the results obtained when moving the nominal signal cross-section up or down by the theoretical uncertainty.

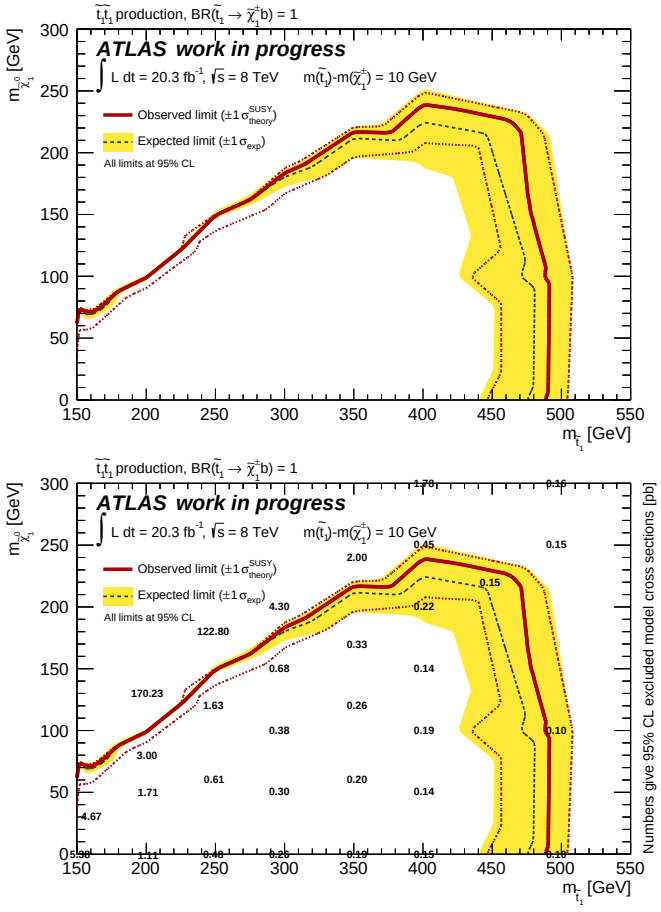

Figure 6.37: Exclusion limits (top) and observed upper limit on the signal cross-section (bottom) at 95% CL in the top-squark neutralino mass plane for a fixed value of $m(\tilde{t}_1) - m(\tilde{\chi}_1^{\pm}) = 10$ GeV. The dashed and solid lines show the 95% C.L. expected and observed limits, respectively, including all uncertainties except for the theoretical signal cross-section uncertainty (PDF and scale). The band around the expected limit shows the $\pm 1\sigma$ result. The dotted $\pm 1\sigma$ lines around the observed limit represent the results obtained when moving the nominal signal cross-section up or down by the theoretical uncertainty.

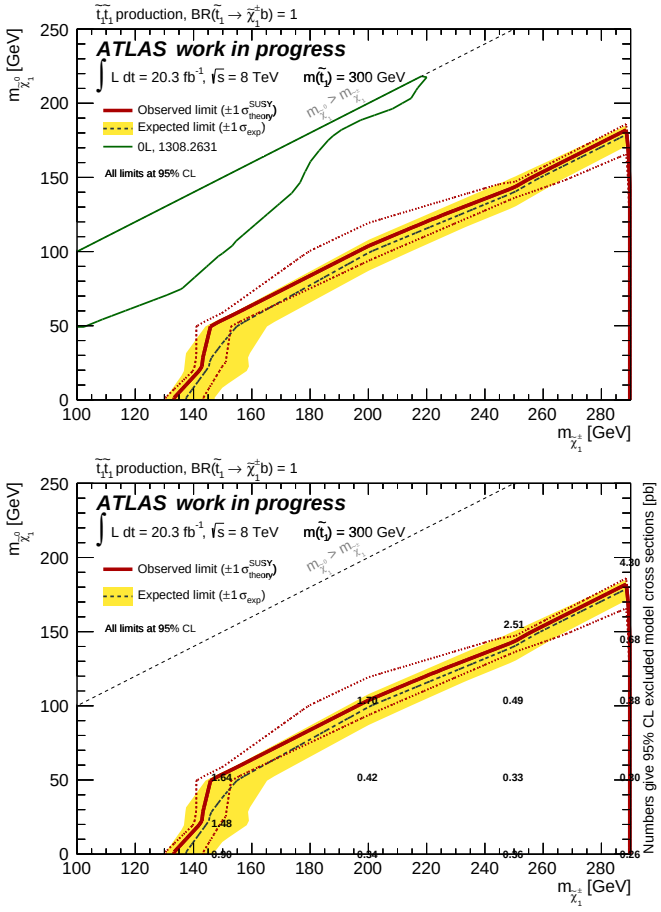

Figure 6.38: Exclusion limits (top) and observed upper limit on the signal cross-section (bottom) at 95% CL in the chargino-neutralino mass plane for a fixed value of $m(\tilde{t}_1) = 300$ GeV. The dashed and solid lines show the 95% C.L. expected and observed limits, respectively, including all uncertainties except for the theoretical signal cross-section uncertainty (PDF and scale). The band around the expected limit shows the $\pm 1\sigma$ result. The dotted $\pm 1\sigma$ lines around the observed limit represent the results obtained when moving the nominal signal cross-section up or down by the theoretical uncertainty.

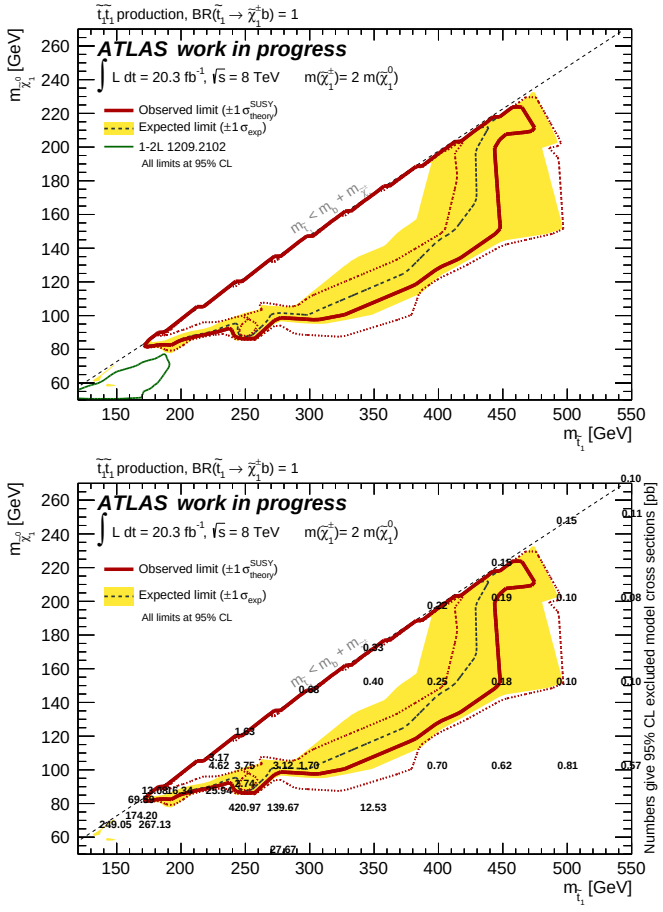

Figure 6.39: Exclusion limits (top) and observed upper limit on the signal cross-section (bottom) at 95% CL in the top squark-neutralino mass plane for $m(\tilde{\chi}_1^{\pm}) = 2m(\tilde{\chi}_1^0)$. The dashed and solid lines show the 95% C.L. expected and observed limits, respectively, including all uncertainties except for the theoretical signal cross-section uncertainty (PDF and scale). The band around the expected limit shows the $\pm1\sigma$ result. The dotted $\pm1\sigma$ lines around the observed limit represent the results obtained when moving the nominal signal cross-section up or down by the theoretical uncertainty.

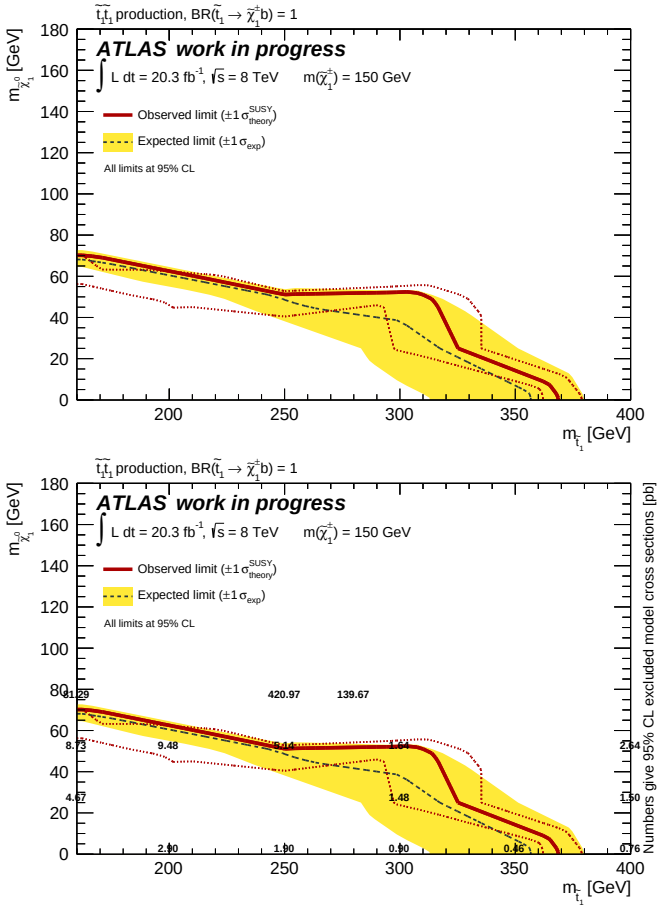

Figure 6.40: Exclusion limits (top) and observed upper limit on the signal cross-section (bottom) at 95% CL in the top squark-neutralino mass plane for a fixed value of $m(\tilde{\chi}_1^{\pm}) = 150$ GeV. The dashed and solid lines show the 95% C.L. expected and observed limits, respectively, including all uncertainties except for the theoretical signal cross-section uncertainty (PDF and scale). The band around the expected limit shows the $\pm 1\sigma$ result. The dotted $\pm 1\sigma$ lines around the observed limit represent the results obtained when moving the nominal signal cross-section up or down by the theoretical uncertainty.

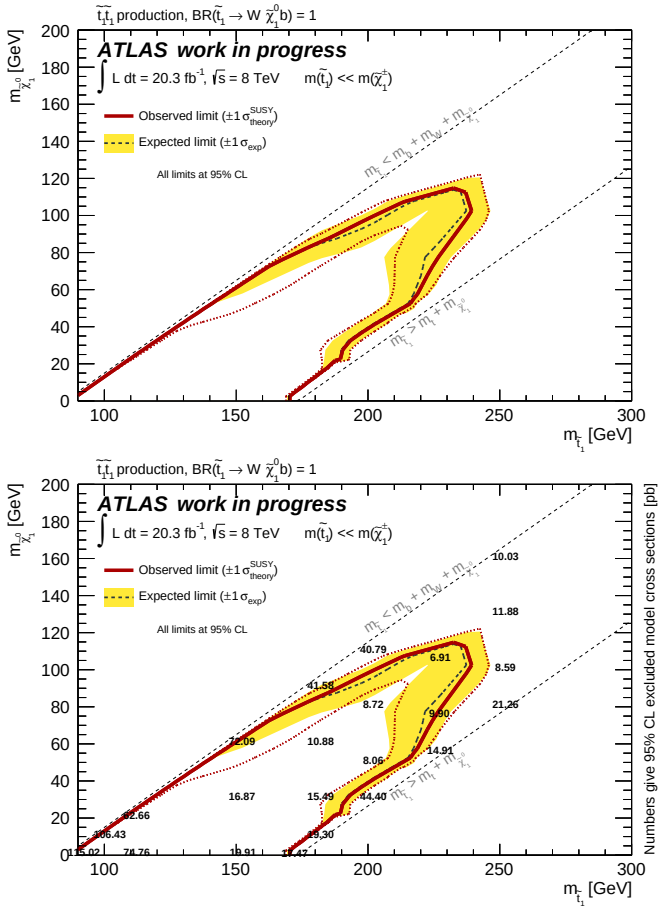

Figure 6.41: Exclusion limits (top) and observed upper limit on the signal cross-section (bottom) at 95% CL in the top squark-neutralino mass plane assuming $\tilde{t}_1 \to Wb\tilde{\chi}_1^0$ with 100% BR. The dashed and solid lines show the 95% C.L. expected and observed limits, respectively, including all uncertainties except for the theoretical signal cross-section uncertainty (PDF and scale). The band around the expected limit shows the $\pm 1\sigma$ result. The dotted $\pm 1\sigma$ lines around the observed limit represent the results obtained when moving the nominal signal cross-section up or down by the theoretical uncertainty.

Conclusions

This thesis focused on the search for top squarks in events with two leptons and missing transverse momentum in pp collisions at both $\sqrt{s} = 7$ TeV and $\sqrt{s} = 8$ TeV, collected by the ATLAS detector at LHC. Two analyses have been presented targeting different top squark decay modes.

The analysis presented in chapter 5 seeks for the evidence of the decay of a heavy partner of the top quark to a top quark and an invisible particle, using 4.7 fb^{-1}of pp collision data at $\sqrt{s} = 7$ TeV. A cut and count strategy has been used, exploiting the event's *stransverse mass* as main discriminant variable.

The number of observed events has been found to be consistent with the Standard Model expectation and limits have been derived on models considering either spin-1/2 heavy top-quark partners or top squarks. A spin-1/2 top-quark partner mass between 300 GeV and 480 GeV is excluded at 95% CL for a heavy neutral particle mass below 100 GeV. A supersymmetric top squark with a mass of 300 GeV decaying to a top quark and a massless neutralino is also excluded at 95% CL.

These results have been published in [2].

The analysis presented in chapter 6 seeks for the evidence of the decay of top squarks in a bottom quark and the lightest chargino, whose decay occurs via a W$^{(*)}$ boson, using 20.3 fb^{-1}of pp collision data at $\sqrt{s} = 8$ TeV. The analysis is based on a similar strategy with respect to the previous one, but has been optimized for various mass hierarchies for the particles involved in the decay chain.

The observed events has been found to be consistent with the Standard Model expectation and limits have been derived in different families of signal models.

For the case of a massless neutralino, a top squark $\tilde{t}_1$ with a mass between 150 and 435 GeV decaying to a b-quark and a chargino is excluded at 95% CL for a chargino approximately degenerate with the top squark. For a 300 GeV top squark decaying to a b-quark and a chargino, chargino masses between 150 and 290 GeV are excluded for a lightest neutralino with mass below 50 GeV.

Limits are also set for the first time on the direct 3-body decay mode, $\tilde{t}_1 \rightarrow W\tilde{\chi}_1^0 b$, excluding a top squark mass between 90 and 170 GeV, under the assumption of a massless neutralino.

Preliminary results regarding this search have been also been published in an ATLAS CONF note [3], and a paper is now in preparation.

The key motivation for searching third generation squarks at the LHC is the naturalness criterion: these particles play a fundamental role in the cancellation of the divergencies of the loops regulating the Higgs mass. The results presented in this thesis have contributed to the search of top squarks, where impressive limits have been set, excluding a significant amount of the parameter space and imposing harsh constraints on the natural spectrum motivated by the supersymmetric models.

APPENDIX A

Hypothesis testing

In this chapter the basic concepts needed for the understanding of the statistical treatment of the data are introduced, focusing on a precise definition and notation of the key components for setting exclusion limits on new physics processes.

The level of agreement of the observed data with a given hypothesis H is quantified by computing the $p-value$, defined as the probability, under assumption of H, of finding data of equal or greater incompatibility with the predictions of H:

$$p-value = P(q > q^{obs}|H) \tag{A.1}$$

where q^{obs} is the value of the test statistic obtained from comparing the observed data with a hypothesis H.

The hypothesis is regarded as excluded if its $p-value$ is observed below a specified threshold given by the size of the test $\alpha \in [0,1]$. It is possible to define the $Z-value$ corresponding to a given $p-value$ as the number of standard deviation Z at which a Gaussian random variable of zero mean would give a one-sided tail area equal to the $p-value$.

The particle physics community has tended to regard rejection of the background hypothesis with a significance of at least $Z = 5$ as an appropriate level to constitute a discovery. This corresponds to $p-value = 2.8 \times 10^{-7}$. For purposes of excluding a signal hypothesis, a threshold $p-value$ of $\alpha = 0.05$, is often used, which corresponds to $Z = 1.64$.

A.1 Profile likelihood-ratio

In addition to parameters of interest such as rate of the signal process (i.e., cross section), the predictions for both the signal and background yields, prior to the scrutiny of the observed data entering the statistical analysis, are subject to multiple uncertainties that are handled by introducing nuisance parameters, denoted by $\vec{\theta}$.

Therefore, the signal and background expectation become functions of these parameters: $S = S(\vec{\theta})$ and $B = B(\vec{\theta})$. In order to handle the nuissance parameters in the likelihoods for testing the compatibility of the data with the background-only and the signal+background hypotheses, the LHC has chosen the profile likelihood-ratio test statistic [106], defined as:

$$\tilde{q}_\mu = -2\log\tilde{\lambda}(\mu) \equiv -2\log\frac{\mathcal{L}(\vec{x}|\mu,\hat{\hat{\theta}}_\mu)}{\mathcal{L}(\vec{x}|\hat{\mu},\hat{\theta})} \quad \text{with the requirement } 0 \leq \hat{\mu} \leq \mu \quad \text{(A.2)}$$

Here, $\hat{\hat{\theta}}_\mu$ refers to the conditional maximum likelihood estimators of θ, given the signal strength parameter μ, and $\vec{x}$ may refer to the actual experimental observation or pseudo-data events. The pair of parameters $\hat{\mu}$ and $\hat{\theta}$ gives the global maximum of the likelihood. The lower constraint $0 \leq \hat{\mu}$ is imposed by physics, since signal rate is defined positive. On the other hand, the upper constraint $\hat{\mu} \leq \mu$ is added by hand in order to guarantee a one-sided confidence interval.

The presence of the nuisance parameters broadens the profile likelihood as a function of μ relative to what one would have if their values were fixed. This reflects the loss of information about μ due to the systematic uncertainties.

A.2 Limit setting

Having defined the test statistic, one constructs probability density functions of $\tilde{q}_\mu$ under the signal+background hypothesis assuming a signal with strength μ. The test-statistic $\tilde{q}_\mu$ can be constructed to decrease monotonically for decreasing signal-like experiments so that the confidence in the signal+background hypothesis is given by the probability that the test-statistic is bigger than or equal to the value observed in the experiment, $\tilde{q}_\mu^{obs}$ for a given tested μ.

This probability is referred to as CL_{s+b}:

$$p_\mu = CL_{s+b} = P(\tilde{q}_\mu \geq \tilde{q}_\mu^{\text{obs}}|\mu S + B) = \int_{q_\mu^{\text{obs}}}^{\infty} f(\tilde{q}_\mu|\mu, \hat{\hat{\boldsymbol{\theta}}}_{\boldsymbol{\mu}}^{\text{obs}})\, dq_\mu, \quad \text{(A.3)}$$

Similarly, the confidence in the background only hypothesis, referred to as CL_b, can be defined as:

$$1 - p_b = CL_b = P(\tilde{q}_\mu \geq \tilde{q}_\mu^{\text{obs}}|B) = \int_{q_\mu^{\text{obs}}}^{\infty} f(\tilde{q}_\mu|0, \hat{\boldsymbol{\theta}}_{\boldsymbol{\mu}}^{\text{obs}})\, dq_\mu, \tag{A.4}$$

Hence, values of CL_b very close to one indicate poor compatibility with the background only hypothesis.

The CL_s method is defined as the following ratio:

$$CL_s \equiv \frac{CL_{s+b}}{CL_b} = \frac{p_\mu}{1 - p_b} \tag{A.5}$$

If, for $\mu = 1$, $CL_s \leq 0.05$ the signal hypothesis is excluded with 95% CL_s confidence level (C.L.).

The CL_s method is introduced to reduce the exclusion of region where the sensibility is very small. In particular the CL_{s+b} method (equation (A.3)) excludes regions where $p_\mu < 0.05$ also when the expected number of signal events is much less than that of background. In the modified approach, using the CL_s, the p-value is effectively penalized by dividing by $1 - p_b$. If the two distributions $f(\tilde{q}_\mu|\mu = 0, \hat{\boldsymbol{\theta}}_{\mathbf{0}}^{\text{obs}})$ and $f(\tilde{q}_\mu|\mu, \hat{\boldsymbol{\theta}}_{\boldsymbol{\mu}}^{\text{obs}})$ are widely separated, then $1 - p_b$ is only slightly less than unity, the penalty is slight, and thus exclusion based in CL_s is similar to that obtained from the usual p-value p_{s+b}. If, however, one has little sensitivity to the signal model, then the two distributions are close together, $1 - p_b$ becomes small, and thus the p-value of $s + b$ is penalized (increased) more. In this way one is prevented from excluding signal models in cases of low sensitivity.

From the definition (A.5), one can see that CL_s is always greater than the p-value p_{s+b}. Thus the models excluded by requiring $CL_s < 0.05$ are a subset of those excluded by the usual criterion $p_{s+b} < 0.05$, and the upper limit from CL_s is therefore higher (weaker). In this sense the CL_s procedure is conservative.

Bibliography

[1] ATLAS Collaboration, *Searches for supersymmetry with the ATLAS detector using final states with two leptons and missing transverse momentum in $\sqrt{s} = 7$ TeV proton-proton collisions*, Phys.Lett. **B709** (2012) 137–157, arXiv:1110.6189 [hep-ex].

[2] ATLAS Collaboration, *Search for a heavy top-quark partner in final states with two leptons with the ATLAS detector at the LHC*, JHEP **1211** (2012) 094, arXiv:1209.4186 [hep-ex].

[3] ATLAS Collaboration, *Search for direct top squark pair production in final states with two leptons in $\sqrt{s}$ = 8 TeV pp collisions using 20fb^{-1} of ATLAS data.*, ATLAS-CONF-2013-048 (2013).

[4] L. Evans and P. Bryant, *LHC Machine*, J. Instrum. **3** (2008) S08001.

[5] https://twiki.cern.ch/twiki/bin/view/AtlasPublic/LuminosityPublicResults.

[6] ATLAS Collaboration, *The ATLAS Experiment at the CERN Large Hadron Collider*, J. Instrum. **3** (2008) S08003. 437 p.

[7] CMS Collaboration, *The CMS experiment at the CERN LHC*, J. Instrum. **3** (2008) S08004.

[8] LHCb Collaboration, *The LHCb Detector at the LHC*, J. Instrum. **3** (2008) S08005.

[9] ALICE Collaboration, *The ALICE experiment at the CERN LHC*, J. Instrum. **3** (2008) S08002.

[10] ATLAS Collaboration, *Readiness of the ATLAS Liquid Argon Calorimeter for LHC Collisions*, Eur. Phys. J. C **70** (2010).

[11] ATLAS Collaboration, *Readiness of the ATLAS Tile Calorimeter for LHC collisions*, Eur. Phys. J. C **70** (2010).

[12] ATLAS Collaboration, *Commissioning of the ATLAS Muon Spectrometer with Cosmic Rays*, Eur. Phys. J. C **70** (2010).

[13] ATLAS Collaboration, *Expected performance of the ATLAS experiment: detector, trigger and physics*, CERN-OPEN-2008-020 (2009).

[14] M. Kaku, *Quantum Field Theory: A Modern Introduction*. Oxford University Press, 1993.

[15] D. Perkins, *Introduction to High Energy Physics*. Cambridge University Press, 2000.

[16] S. P. Martin, *A Supersymmetry primer*, `arXiv:hep-ph/9709356 [hep-ph]`.

[17] R. Barbieri and G. Giudice, *Upper bounds on supersymmetric particle masses*, Nuclear Physics B **306** no. 1, (1988) 63 – 76.

[18] J. L. Feng, *Naturalness and the Status of Supersymmetry*, Ann.Rev.Nucl.Part.Sci. **63** (2013) 351–382, `arXiv:1302.6587 [hep-ph]`.

[19] D. Volkov and V. Akulov, *Is the Neutrino a Goldstone Particle?*, Phys.Lett. **B46** (1973) 109–110.

[20] J. Wess and B. Zumino, *Supergauge Invariant Extension of Quantum Electrodynamics*, Nucl.Phys. **B78** (1974) 1.

[21] J. Wess and B. Zumino, *Supergauge Transformations in Four-Dimensions*, Nucl.Phys. **B70** (1974) 39–50.

[22] Y. Golfand and E. Likhtman, *Extension of the Algebra of Poincare Group Generators and Violation of p Invariance*, JETP Lett. **13** (1971) 323–326.

[23] H. P. Nilles, *Supersymmetry, Supergravity and Particle Physics*, Phys.Rept. **110** (1984) 1–162.

[24] H. E. Haber and G. L. Kane, *The Search for Supersymmetry: Probing Physics Beyond the Standard Model*, Phys.Rept. **117** (1985) 75–263.

[25] J. Wess and J. Bagger, *Supersymmetry and Supergravity: (Revised Edition)*. Princeton Series in Physics. Princeton University Press, 1992.

[26] S. Dimopoulos and D. W. Sutter, *The Supersymmetric flavor problem*, Nucl.Phys. **B452** (1995) 496–512.

[27] M. Papucci, J. T. Ruderman, and A. Weiler, *Natural SUSY Endures*, JHEP **1209** (2012) 035, `arXiv:1110.6926 [hep-ph]`.

[28] W. Beenakker, M. Kramer, T. Plehn, M. Spira, and P. M. Zerwas, *Stop production at hadron colliders*, Nucl. Phys. **B515** (1998) 3–14, `hep-ph/9710451`.

[29] W. Beenakker, S. Brensing, M. Kramer, A. Kulesza, E. Laenen, and I. Niessen, *Supersymmetric top and bottom squark production at hadron colliders*, JHEP. **1008** (2010) 098, `arXiv:1006.4771 [hep-ph]`.

[30] W. Beenakker, S. Brensing, M. Kramer, A. Kulesza, E. Laenen, et al., *Squark and gluino hadroproduction*, Int.J.Mod.Phys. **A26** (2011) 2637–2664, `arXiv:1105.1110 [hep-ph]`.

[31] M. Kramer, A. Kulesza, R. van der Leeuw, M. Mangano, S. Padhi, et al., *Supersymmetry production cross sections in pp collisions at* $\sqrt{s} = 7$ *TeV*, `arXiv:1206.2892 [hep-ph]`.

[32] C. Boehm, A. Djouadi, and Y. Mambrini, *Decays of the lightest top squark*, Phys.Rev. **D61** (2000) 095006.

[33] H.-C. Cheng and I. Low, *TeV symmetry and the little hierarchy problem*, JHEP **0309** (2003) 051, `arXiv:hep-ph/0308199 [hep-ph]`.

[34] H.-C. Cheng and I. Low, *Little hierarchy, little Higgses, and a little symmetry*, JHEP **0408** (2004) 061, `arXiv:hep-ph/0405243 [hep-ph]`.

[35] H.-C. Cheng, I. Low, and L.-T. Wang, *Top partners in little Higgs theories with T-parity*, Phys.Rev. **D74** (2006) 055001, `arXiv:hep-ph/0510225 [hep-ph]`.

[36] T. Appelquist, H.-C. Cheng, and B. A. Dobrescu, *Bounds on universal extra dimensions*, Phys.Rev. **D64** (2001) 035002, `arXiv:hep-ph/0012100 [hep-ph]`.

[37] J. Aguilar-Saavedra, *Identifying top partners at LHC*, JHEP **0911** (2009) 030, arXiv:0907.3155 [hep-ph].

[38] F. del Aguila and M. J. Bowick, *The Possibility of New Fermions With $\Delta I = 0$ Mass*, Nucl.Phys. **B224** (1983) 107.

[39] B. Holdom, W. Hou, T. Hurth, M. Mangano, S. Sultansoy, and G. Unel, *Four statements about the fourth generation*, PMC Physics A **3** no. 1, (2009) 4. http://www.physmathcentral.com/1754-0410/3/4.

[40] S. Cetin, G. Hou, V. Ozcan, A. Rozanov, and S. Sultansoy, *Status of the Fourth Generation: A Brief Summary of B3SM-III Workshop in Four Parts*, arXiv:1112.2907 [hep-ph].

[41] M. Buchkremer, J.-M. Gerard, and F. Maltoni, *Closing in on a perturbative fourth generation*, JHEP **1206** (2012) 135, arXiv:1204.5403 [hep-ph].

[42] ATLAS Collaboration, *First tuning of HERWIG/JIMMY to ATLAS data*, ATL-PHYS-PUB-2010-014 (2010).

[43] ATLAS Collaboration, *Charged particle multiplicities in pp interactions at $\sqrt{s}$ = 0.9 and 7 TeV in a diffractive limited phase-space measured with the ATLAS detector at the LHC and new PYTHIA6 tune*, ATLAS-CONF-2010-031 (2010).

[44] ATLAS Collaboration, *The ATLAS Simulation Infrastructure*, Eur.Phys.J. **C70** (2010) 823–874, arXiv:1005.4568 [physics.ins-det].

[45] GEANT4 Collaboration, S. Agostinelli et al., *GEANT4: A Simulation toolkit*, Nucl.Instrum.Meth. **A506** (2003) 250–303.

[46] S. Frixione and B. R. Webber, *Matching NLO QCD computations and parton shower simulations*, JHEP **0206** (2002) 029, arXiv:hep-ph/0204244 [hep-ph].

[47] S. Frixione, E. Laenen, P. Motylinski, and B. R. Webber, *Single-top production in MC@NLO*, JHEP **0603** (2006) 092, arXiv:hep-ph/0512250 [hep-ph].

[48] G. Corcella, I. Knowles, G. Marchesini, S. Moretti, K. Odagiri, et al., *HERWIG 6: An Event generator for hadron emission reactions with interfering gluons (including supersymmetric processes)*, JHEP **0101** (2001) 010, arXiv:hep-ph/0011363 [hep-ph].

[49] J. Butterworth, J. R. Forshaw, and M. Seymour, *Multiparton interactions in photoproduction at HERA*, Z.Phys. **C72** (1996) 637–646, arXiv:hep-ph/9601371 [hep-ph].

[50] H.-L. Lai, M. Guzzi, J. Huston, Z. Li, P. M. Nadolsky, et al., *New parton distributions for collider physics*, Phys.Rev. **D82** (2010) 074024, arXiv:1007.2241 [hep-ph].

[51] S. Frixione, P. Nason, and C. Oleari, *Matching NLO QCD computations with Parton Shower simulations: the POWHEG method*, JHEP **0711** (2007) 070, arXiv:0709.2092 [hep-ph].

[52] T. Sjostrand, S. Mrenna, and P. Z. Skands, *PYTHIA 6.4 Physics and Manual*, JHEP **0605** (2006) 026, arXiv:hep-ph/0603175 [hep-ph].

[53] M. L. Mangano, M. Moretti, F. Piccinini, R. Pittau, and A. D. Polosa, *ALPGEN, a generator for hard multiparton processes in hadronic collisions*, JHEP **0307** (2003) 001, arXiv:hep-ph/0206293 [hep-ph].

[54] B. P. Kersevan and E. Richter-Was, *The Monte Carlo event generator AcerMC version 2.0 with interfaces to PYTHIA 6.2 and HERWIG 6.5*, arXiv:hep-ph/0405247 [hep-ph].

[55] ATLAS Collaboration, *Measurement of $t\bar{t}$ production with a veto on additional central jet activity in pp collisions at sqrt(s) = 7 TeV using the ATLAS detector*, Eur.Phys.J. **C72** (2012) 2043, arXiv:1203.5015 [hep-ex].

[56] ATLAS Collaboration, *Measurement of underlying event characteristics using charged particles in pp collisions at sqrts =900 GeV and 7 TeV with the ATLAS detector in a limited phase space*, ATLAS-CONF-2011-009 (2011).

[57] J. Pumplin, D. Stump, J. Huston, H. Lai, P. M. Nadolsky, et al., *New generation of parton distributions with uncertainties from global QCD analysis*, JHEP **0207** (2002) 012, arXiv:hep-ph/0201195 [hep-ph].

[58] J. Alwall, M. Herquet, F. Maltoni, O. Mattelaer, and T. Stelzer, *MadGraph 5 : Going Beyond*, JHEP **1106** (2011) 128, arXiv:1106.0522 [hep-ph].

[59] T. Gleisberg, S. Hoeche, F. Krauss, M. Schonherr, S. Schumann, et al., *Event generation with SHERPA 1.1*, JHEP **0902** (2009) 007, arXiv:0811.4622 [hep-ph].

[60] R. Hamberg, W. van Neerven, and T. Matsuura, *A Complete calculation of the order $\alpha - s^2$ correction to the Drell-Yan K factor*, Nucl.Phys. **B359** (1991) 343–405.

[61] M. Aliev, H. Lacker, U. Langenfeld, S. Moch, P. Uwer, et al., *HATHOR: HAdronic Top and Heavy quarks crOss section calculatoR*, Comput.Phys.Commun. **182** (2011) 1034–1046, arXiv:1007.1327 [hep-ph].

[62] N. Kidonakis, *Two-loop soft anomalous dimensions for single top quark associated production with a W- or H-*, Phys.Rev. **D82** (2010) 054018, arXiv:1005.4451 [hep-ph].

[63] T. Binoth, M. Ciccolini, N. Kauer, and M. Kramer, *Gluon-induced W-boson pair production at the LHC*, JHEP **0612** (2006) 046, arXiv:hep-ph/0611170 [hep-ph].

[64] A. Lazopoulos, T. McElmurry, K. Melnikov, and F. Petriello, *Next-to-leading order QCD corrections to $t\bar{t}Z$ production at the LHC*, Phys.Lett. **B666** (2008) 62–65.

[65] M. Bahr, S. Gieseke, M. Gigg, D. Grellscheid, K. Hamilton, et al., *Herwig++ Physics and Manual*, Eur.Phys.J. **C58** (2008) 639–707, arXiv:0803.0883 [hep-ph].

[66] M. Cacciari, M. Czakon, M. Mangano, A. Mitov, and P. Nason, *Top-pair production at hadron colliders with next-to-next-to-leading logarithmic soft-gluon resummation*, Phys.Lett. **B710** (2012) 612–622, arXiv:1111.5869 [hep-ph].

[67] P. Barnreuther, M. Czakon, and A. Mitov, *Percent Level Precision Physics at the Tevatron: First Genuine NNLO QCD Corrections to $q\bar{q} \to t\bar{t} + X$*, Phys.Rev.Lett. **109** (2012) 132001, arXiv:1204.5201 [hep-ph].

[68] M. Czakon and A. Mitov, *NNLO corrections to top-pair production at hadron colliders: the all-fermionic scattering channels*, JHEP **1212** (2012) 054, arXiv:1207.0236 [hep-ph].

[69] M. Czakon and A. Mitov, *NNLO corrections to top pair production at hadron colliders: the quark-gluon reaction*, JHEP **1301** (2013) 080, arXiv:1210.6832 [hep-ph].

[70] M. Czakon, P. Fiedler, and A. Mitov, *The total top quark pair production cross-section at hadron colliders through $O(alpha_S^4)$*, Phys.Rev.Lett. **110** (2013) 252004, arXiv:1303.6254 [hep-ph].

[71] M. Czakon and A. Mitov, *Top++: A Program for the Calculation of the Top-Pair Cross-Section at Hadron Colliders*, arXiv:1112.5675 [hep-ph].

[72] M. Botje, J. Butterworth, A. Cooper-Sarkar, A. de Roeck, J. Feltesse, et al., *The PDF4LHC Working Group Interim Recommendations*, arXiv:1101.0538 [hep-ph].

[73] A. Martin, W. Stirling, R. Thorne, and G. Watt, *Parton distributions for the LHC*, Eur.Phys.J. **C63** (2009) 189–285, arXiv:0901.0002 [hep-ph].

[74] A. Martin, W. Stirling, R. Thorne, and G. Watt, *Uncertainties on alpha(S) in global PDF analyses and implications for predicted hadronic cross sections*, Eur.Phys.J. **C64** (2009) 653–680, arXiv:0905.3531 [hep-ph].

[75] J. Gao, M. Guzzi, J. Huston, H.-L. Lai, Z. Li, et al., *The CT10 NNLO Global Analysis of QCD*, arXiv:1302.6246 [hep-ph].

[76] R. D. Ball, V. Bertone, S. Carrazza, C. S. Deans, L. Del Debbio, et al., *Parton distributions with LHC data*, Nucl.Phys. **B867** (2013) 244–289, arXiv:1207.1303 [hep-ph].

[77] T. Cornelissen, M. Elsing, S. Fleischmann, W. Liebig, E. Moyse, and A. Salzburger, *Concepts, Design and Implementation of the ATLAS New Tracking (NEWT)*, ATL-SOFT-PUB-2007-007. ATL-COM-SOFT-2007-002 (2007).

[78] ATLAS Collaboration, *Characterization of Interaction-Point Beam Parameters Using the pp Event-Vertex Distribution Reconstructed in the ATLAS Detector at the LHC*, ATLAS-CONF-2010-027 (2010).

[79] R. Fruhwirth, W. Waltenberger, and P. Vanlaer, *Adaptive vertex fitting*, J.Phys. **G34** (2007) N343.

[80] M. Cacciari, G. P. Salam, and G. Soyez, *The Anti-k(t) jet clustering algorithm*, JHEP **0804** (2008) 063.

[81] ATLAS Collaboration, *Measurement of the cross section for the production of a W boson in association with b-jets in pp collisions at $\sqrt{s}$ = 7 TeV with the ATLAS detector*, Phys. Lett. B **707** (2011).

[82] ATLAS Collaboration, *Measurement of the top quark pair production cross section in pp collisions at $\sqrt{s}$ = 7 TeV in dilepton final states with ATLAS*, Phys. Lett. B **707** (2011) 459–477.

[83] ATLAS Collaboration, *Measurement of the inclusive and dijet cross-sections of b-jets in pp collisions at $\sqrt{s}$ = 7 TeV with the ATLAS detector*, Eur. Phys. J. C **71** (2011).

[84] ATLAS Collaboration, *Calibrating the b-Tag Efficiency and Mistag Rate in 35 pb^{-1} of Data with the ATLAS Detector*, ATLAS-CONF-2011-089 (2011).

[85] ATLAS Collaboration, *b-Jet Tagging Efficiency Calibration using the System8 Method*, ATLAS-CONF-2011-143 (2011).

[86] ATLAS Collaboration, *Measurement of the b-tag Efficiency in a Sample of Jets Containing Muons with 5 fb^{-1} of Data from the ATLAS Detector*, ATLAS-CONF-2012-043 (2012). https://cds.cern.ch/record/1435197.

[87] W. Lampl, S. Laplace, D. Lelas, P. Loch, H. Ma, S. Menke, S. Rajagopalan, D. Rousseau, S. Snyder, and G. Unal, *Calorimeter Clustering Algorithms: Description and Performance*, ATL-LARG-PUB-2008-002; ATL-COM-LARG-2008-003 (2008).

[88] ATLAS Collaboration, *Electron and photon reconstruction and identification in ATLAS: expected performance at high energy and results at 900 GeV*, ATLAS-CONF-2010-005 (2010).

[89] D. Banfi, L. Carminati, and L. Mandelli, *Calibration of the ATLAS electromagnetic calorimeter using calibration hits*, ATL-LARG-PUB-2007-012; ATL-COM-LARG-2007-007 (2007).

[90] `https://twiki.cern.ch/twiki/bin/view/AtlasPublic/ElectronGammaPublicCollisionResults`.

[91] ATLAS Collaboration, G. Aad et al., *Electron performance measurements with the ATLAS detector using the 2010 LHC proton-proton collision data*, Eur.Phys.J. **C72** (2012) 1909, `arXiv:1110.3174 [hep-ex]`.

[92] S. Hassani, L. Chevalier, E. Lancon, J. F. Laporte, R. Nicolaidou and A. Ouraou, *A muon identification and combined reconstruction procedure for the ATLAS detector at the LHC using the (MUONBOY, STACO, MuTag) reconstruction packages*, Nucl. Instrum. Meth. **A572** (2007) 77.

[93] T. Lagouri et al., *A muon identification and combined reconstruction procedure for the ATLAS detector at the LHC at CERN*, IEEE Trans. Nucl. Sci. **51** (2004) 3030–3033.

[94] ATLAS Collaboration, *Muon Performance in Minimum Bias pp Collision Data at $\sqrt{s}$ = 7 TeV with ATLAS*, ATLAS-CONF-2010-036 (2010).

[95] `https://twiki.cern.ch/twiki/bin/view/Atlas/MuonPerformancePublicPlots`.

[96] ATLAS Collaboration, *Performance of Missing Transverse Momentum Reconstruction in Proton-Proton Collisions at $\sqrt{s}$ = 7 TeV with ATLAS*, Eur. Phys. J. C **72** (2011) 1844.

[97] R. Barbieri and G. Giudice, *Upper Bounds on Supersymmetric Particle Masses*, Nucl.Phys. **B306** (1988) 63.

[98] C. Lester and D. Summers, *Measuring masses of semiinvisibly decaying particles pair produced at hadron colliders*, Phys.Lett. **B463** (1999) 99–103.

[99] A. Barr, C. Lester, and P. Stephens, *m(T2): The Truth behind the glamour*, J.Phys. **G29** (2003) 2343–2363.

[100] C. Hensel, M. Hamer, F. Kohn, and A. Quadt, *Measurement of Trigger Efficiencies from Data and their Application in Physics Analyses*, ATL-COM-DAQ-2011-083 (2011).

[101] ATLAS Collaboration, *Jet energy measurement with the ATLAS detector in proton-proton collisions at $\sqrt{s}$ = 7 TeV*, CERN-PH-EP-2011-191 (2011).

[102] ATLAS Collaboration, *Jet energy resolution and selection efficiency relative to track jets from in-situ techniques with the ATLAS Detector Using Proton-Proton Collisions at a Center of Mass Energy sqrts = 7 TeV*, ATLAS-CONF-2010-054 (2010).

[103] ATLAS Collaboration, *Improved Luminosity Determination in* **pp** *Collisions at* $\sqrt{s}$ *= 7 TeV using the ATLAS Detector at the LHC*, ATLAS-CONF-2012-080 (2012).

[104] ATLAS Collaboration, *Measurement of the* $W \to \ell\nu$ *and* $Z/\gamma^* \to \ell\ell$ *production cross sections in proton-proton collisions at* $\sqrt{s} = 7$ *TeV with the ATLAS detector*, JHEP **1012** (2010) 060.

[105] M. Aliev, H. Lacker, U. Langenfeld, S. Moch, P. Uwer, et al., *HATHOR: HAdronic Top and Heavy quarks crOss section calculatoR*, Comput.Phys.Commun. **182** (2011) 1034–1046.

[106] G. Cowan, K. Cranmer, E. Gross, and O. Vitells, *Asymptotic formulae for likelihood-based tests of new physics*, Eur.Phys.J. **C71** (2011) 1554, `arXiv:1007.1727 [physics.data-an]`.

[107] ATLAS Collaboration, *Search for New Phenomena in* $t\bar{t}$ *Events With Large Missing Transverse Momentum in Proton-Proton Collisions at* $\sqrt{s} = 7$ *TeV with the ATLAS Detector*, Phys.Rev.Lett. **108** (2012) 041805, `arXiv:1109.4725 [hep-ex]`.

[108] ATLAS Collaboration, *Search for top and bottom squarks from gluino pair production in final states with missing transverse energy and at least three b-jets with the ATLAS detector*, CERN-PH-EP-2012-194 (2012).

[109] ATLAS Collaboration, *Search for gluino pair production in final states with missing transverse momentum and at least three b-jets using 12.8* fb^{-1} *of pp collisions at sqrts* $= 8$ *TeV with the ATLAS Detector.*, ATLAS-CONF-2012-145 (2012).

[110] ATLAS Collaboration, *Search for supersymmetry using events with three leptons, multiple jets, and missing transverse momentum in 13.0* fb^{-1} *of pp collisions with the ATLAS detector at* $\sqrt{s} = 8$ *TeV*, ATLAS-CONF-2012-151 (2012).

[111] ATLAS Collaboration, *Search for light scalar top quark pair production in final states with two leptons with the ATLAS detector in* $\sqrt{s} = 7$ *TeV proton-proton collisions*, CERN-PH-EP-2012-211 (2012).

[112] ATLAS Collaboration, *Search for light top squark pair production in final states with leptons and b-jets with the ATLAS detector in $\sqrt{s} = 7$ TeV proton–proton collisions*, ATLAS-CONF-2012-070 (2012).

[113] ATLAS Collaboration, *Search for a supersymmetric partner to the top quark in final states with jets and missing transverse momentum at $\sqrt{s} = 7$ TeV with the ATLAS detector*, CERN-PH-EP-2012-201 (2012).

[114] ATLAS Collaboration, *Search for direct top squark pair production in final states with one isolated lepton, jets, and missing transverse momentum in $\sqrt{s} = 7$ TeV pp collisions using 4.7 fb^{-1} of ATLAS data*, Phys.Rev.Lett. **109** (2012) 211803.

[115] ATLAS Collaboration, *Search for Scalar Bottom Quark Pair Production with the ATLAS Detector in pp Collisions at $\sqrt{s} = 7$ TeV*, Phys. Rev. Lett. **108** (2012) 181802.

[116] ATLAS Collaboration, *Search for direct sbottom production in event with two b-jets using 12.8 fb^{-1} of pp collisions at $\sqrt{s} = 8$ TeV with the ATLAS Detector.*, ATLAS-CONF-2012-165 (2012).

[117] ATLAS Collaboration, *Search for scalar top quark pair production in natural gauge mediated supersymmetry models with the ATLAS detector in pp collisions at $\sqrt{s} = 7$ TeV*, Phys.Lett. **B715** (2012) 44–60.

[118] ATLAS Collaboration, *Pile-up subtraction and suppression for jets in ATLAS.*, ATLAS-CONF-2013-083 (2013).

[119] G. Polesello and D. R. Tovey, *Supersymmetric particle mass measurement with the boost-corrected contransverse mass*, JHEP **1003** (2010) 030.

[120] ATLAS Collaboration, *Luminosity Determination in pp Collisions at sqrt(s) = 7 TeV using the ATLAS Detector in 2011*, ATLAS-CONF-2011-116 (2011).